AN INVESTIGATION OF THE INFLUENCE OF SILVER DOPING ON THE INTERGRANULAR 'WEAK-LINK' PROPERTIES OF THE SUPERCONDUCTING SYSTEM, $Y_1Ba_2Cu_3O_{7-x}$

by

Alan Lawrence Leigh Jarvis

University of KwaZulu-Natal

December 2006

Submitted in fulfilment of the academic requirements for the degree of Doctor of Philosophy in the School of Electrical, Electronic and Computer Engineering, University of KwaZulu-Natal, 2006.

Abstract

High-temperature superconducting materials have found considerable technological application and still have a largely unrealised potential. The key to unlocking this potential depends on a better understanding of their properties; in particular, the maximum 'critical current density' which these materials, in the form of wires, tapes, thin-films and bulk monolithic forms, are able to support for high-current applications.

The 'critical current density' in a polycrystalline high-temperature oxide superconductor system is determined by a percolation process of the supercurrent through a three dimensional grain-boundary network. Grain-boundaries in these systems behave as Josephson junction 'weak-links' and they severely limit the critical current density in the presence of even moderate self or applied magnetic fields.

In the present work, isothermal quasi-static magnetisation measurements on the polycrystalline $Y_1Ba_2Cu_3O_{7-x}$ system are presented and analysed. An effective granular penetration depth in conjunction with a critical state model, which includes an approximate treatment for the percolation process, is used to obtain many of the salient physical parameters of the grain-boundary Josephson junctions and of the three-dimensional grain boundary junction network. Determination of the temperature and magnetic field dependence of several of these parameters, in particular a magnetic field-independent critical current which depends on the microstructure of the grain-boundary junction network, allows for testing and verification of models of the weak-link and network behaviour.

This treatment has been carried out specifically on various silver doped polycrystalline $Y_1Ba_2Cu_3O_{7-x}$ specimens in order to determine and quantify the effects of silver doping. An improvement in the critical current density with silver doping is explained in terms of silver scavenging and ridding grain-boundaries of impurities, and a proximity effect where trace amounts of silver residing in the grain-boundaries decreases the normal resistance of the grain-boundary Josephson junction. The insight gained from silver doping experimentation led to a macroscopic investigation into the joining of large single-domain $Y_1Ba_2Cu_3O_{7-x}$ specimens for large-scale applications.

Preface

The research presented in this thesis was performed by Mr. Alan Lawrence Leigh Jarvis. A substantial amount of the work was conducted in the Solid State Laboratory at the University of Natal's School of Pure and Applied Physics under the guidance of Professor Terence Doyle. Professor Doyle secured funding for the research from the 'Foundation for Research Development', which has been replaced by the 'National Research Foundation'. The high-temperature superconducting joining experiments were based in the School of Electrical, Electronic and Computer Engineering at the University of KwaZulu-Natal; where funding was sourced from the University Research Foundation.

Parts of this thesis have been presented by the author at the European Conference on Applied Superconductivity 1997 (a peer reviewed conference) in Enschede, The Netherlands; the South African Institute of Physics Conference 1998 in Cape Town, South Africa and the European Conference on Applied Superconductivity 2005 in Vienna, Austria (this paper was rated in the top 25% of papers submitted and published in the Journal of Physics: Conference Series 2006, Institute of Physics).

The whole thesis, unless specifically indicated to the contrary in the text, is the author's work, and has not been submitted in part, or in whole, to any other University.

As the candidate's co-supervisor, I have approved this thesis for submission.

Name: .....

Date: .....

Signature: .....

Acknowledgements

Even though Professor Terence Doyle (Terry) was on paper a co-supervisor, he was vital to guiding of the research documented in this thesis. Working with Terry was a privilege and an honour, and inspirational on many levels – one being the fact that I opted for the life of an academic. Through the years Terry became a very good friend and he has always given me advice with my best interests at heart. Not a dull moment was had when Terry came around for dinner, or to watch a BSG episode. Limericks and wit (and 'matchsticks on Sandy Bay') were the order of the evening. I am sure one of Terry's favourite words is 'serendipity', and it was 'serendipity' that led me to my Ag-doping experiments - yes, that stroll down to the Physics Department (University of Natal) changed my life for good.

The tea-room in the Physics Department was a place of enlightenment, with discussions about Quantum Mechanics (Don), Optics (Max) and Materials (Terry), and lively debates (Peter) a daily occurrence. I always felt that I gained a quasi-Physics degree just by doing, or being persuaded to do, tea (Ricardo)!

I would also like to thank my supervisor-on-paper, Professor Tony Broadhurst. I know superconductivity was not his area of expertise, but his enthusiasm, suggestions and support, especially at Faculty level (the wolves), helped tremendously in the closing stages of this work.

To my good friends and family who have encouraged me to finish 'that damn thesis', Mom, Dad, David, Kesh and Christine, and to Ron, the fruit is ripe and ready to be picked versus 'just hit the print button'. Thanks to my squash buddy and friend Dayle, whose offer to proofread this thesis was an indication of true friendship.

Finally, to my loving wife Louella – it is impossible for me to express how much I have appreciated your support and love during this Ph.D. chapter of our lives; and to my precious children James and Kate who gave me the final mental push to put the thesis to bed.

Selected List of Symbols and Their Units

Roman Letters

A

a_0	Length of cubic grain/size of junction (m)
A	Area of the junction or structural non-uniformities (m^2)
A_p	Magnetic vector potential (Tm)

B

b	Reduced flux in junction or length (m)
B	Magnetic flux density (SI - T , Gaussian - Oe)

D

d	Thickness of HTS specimen (m)
$\bar{d}, d$	Average or effective junction-barrier thickness (m)
D_m	Demagnetisation factor

E

e	Electron charge (1.6×10^{-19} C)
e^*	$2e$
E	Electric field (Vm^{-1})
E_{kin}	Kinetic energy (J)
E_{mag}	Magnetic energy (J)

F

f	Measure of average modulation depth of j_c in junction
f_n	Normal volume fraction
f_s	Superconducting volume fractions
$f(i_{c0})$	Critical current (intergranular) distribution function
$f_j(i_{cj})$	Modified critical current distribution function
F	Force (N)

G

g	Gibbs free energy of system, function of position (J)
g_n, g_s	Normal, superconductor state free energy, function of position (J)
$g(\zeta)$	correction factor

G	Gibbs free energy (J), Field dependent component of J_{cj}
G_n	Gibbs normal free energy (J)
G_s	Gibbs superconducting free energy (J)
H	
h	Planck's constant ($= 6.6 \times 10^{-34}$ Js)
h	H-bar ($= h/2\pi = 1.1 \times 10^{-34}$Js)
$\mathbf{h}, \mathbf{H}$	local field, mean internal field (SI - A/m , Gaussian - Oe)
H	Magnetic field (SI - A/m , Gaussian - Oe)
H_a	Applied magnetic field (SI - A/m , Gaussian - Oe)
H_{c0}	Critical magnetic field at $T = 0$ K (SI - A/m , Gaussian - Oe)
H_{c1}	Lower critical magnetic field (SI - A/m , Gaussian - Oe)
H_{c1g}	Intragranular critical lower field for grains (Oe)
H_{c1j}	Intergranular/Josephson critical field for GBJs (Oe)
H_{c2}	Upper critical magnetic field (SI - A/m , Gaussian - Oe)
H_i	Mean internal field (Oe)
H_{irr}	Irreversible field (Oe)
H_p	Magnetic field for complete penetration into specimen (Oe)
H_0	Characteristic field of average weak-link network junction (Oe)
I	
i_{cj}	Intergranular/Josephson critical current (A)
i^*	Local smallest critical current in network (A)
I_0, I_1	Modified Bessel functions
I_c	Critical transport current (A)
I_{cj}	Josephson tunnelling critical current (A/cm^2)
$I_{cj}(T)$	Expression for temperature-dependent component of I_{cj} (A/cm^2)
I_{c0j}	Josephson tunnelling critical current at $T = 0$ K (A/cm^2)
J	
j_c	Local junction critical current densities (A/cm^2)
$\overline{j_c}$	Mean junction critical current densities (A/cm^2)
J_c	Transport critical supercurrent density (A/cm^2)

J_{c0} Zero-field critical current density (A/cm^2)

J_{c1} Field independent critical current density (A/cm^2)

J_{cj} Effective local shielding current density $\equiv$ transport current density (A/cm^2)

K

k_B Boltzmann constant ($= 1.4 \times 10^{-23}$ J/K)

L

l_e Electron mean free path (m)

L Helmholtz free energy (J), Average intervortex spacing (m)

M

m effective mass (kg)

m_e Mass of an electron (9.11×10^{-31}kg)

m^* $2m_e$

M Magnetisation (SI - A/m , Gaussian - Oe)

M^- Magnetisation measured in decreasing field (SI - A/m , Gaussian - Oe)

M^+ Magnetisation measured in increasing field (SI - A/m , Gaussian - Oe)

M_{eq} Equilibrium magnetisation (Oe)

M_i Mass of isotope (kg)

M_{irr} Irreversible magnetisation (Oe)

N

n Total electron density (#/cm^3), Limit type: $n = -1/2$ (dirty), $n = -1/3$ (clean)

n_n Normal electron density (#/cm^3)

n_s Superconducting electron density (#/cm^3)

P

p Momentum (kgms^{-1})

P_c Percolation limit

R

r distance (m)

r_0 Correlation radius of the junction irregularities (m), flux penetration radius (m)

r_{eff}	Effective radius (m)
R	Resistance (Ω), Radius of long cylindrical HTS specimen
R_g	Radius of cylindrical grain $\simeq \frac{1}{2}a_0$ (m)
R_n	Normal state junction resistance (Ω)
S	
S	Entropy (J/K), Average junction area (m^2)
T	
t	Time (s)
$t = \frac{T}{T_c}$	Reduced temperature
t_i	Critical conductivity index
T	Temperature (K)
T_c	Critical Temperature (K)
T_{cu}	Curie temperature (K)
$T_{c,m}$	Critical temperature determined from magnetic measurements (K)
V	
v_F	Fermi velocity (m/s)
$\mathbf{v}_n$	Normal electron drift velocity (m/s)
$\mathbf{v}_s$	Superconducting electron drift velocity (m/s)
V	Volume (m^3)
V_d	Voltage across the Josephson junction (V)
X	
x	Distance (m)
x, y, z	Cartesian coordinates
x_n	Position in the plane of the junction (m)
x_0	Reduced flux penetration distance into the specimen (m)

Greek Letters

α	Ginzburg-Landau phenomenological parameter
β	Ginzburg-Landau phenomenological parameter
β_c	Proportional energy gap constant
γ	Josephson junction field-independent current in junction (A)
γ_φ	Phase difference (dimensionless)
Δ	Superconducting order parameter or energy gap (eV)
Δ_0	Superconducting order parameter at $T = 0$ K (eV)
Δ_i	Suppressed gap parameter at the junction boundaries (eV)
Δ_∞	Gap parameter far from the junction boundaries (eV)
ΔM	Magnetisation width (Oe)
δ	Reduced field-independent critical current density
ζ	Superconductor anisotropy factor (dimensionless)
η	Geometrical/morphological constant
θ	Misorientation angle between grains
κ	GL parameter (dimensionless)
Λ	Fractional deviation of a cylindrical grain from Meissner state
λ	Penetration depth (m)
$\overline{\lambda}$	Average penetration depth (m)
λ_{ab}	Penetration depth in the ab-plane (m)
$\lambda_{a,b,c}$	Average penetration depth in a, b or c direction (m)
λ_{ep}	Electron-phonon parameter (dimensionless)
$\overline{\lambda_g}$	Average granular penetration depth (m)
λ_J	Josephson penetration depth (m)
λ_L	London penetration depth (m)
μ_0	Permeability of free space
μ_{eff}	Effective permeability
ξ	Coherence length (m)
ξ_0	BCS coherence length (m)
ξ_{GL}	GL coherence length (m)

ξ_p	Pippard coherence length (m)
ξ_S	Effective coherence length (m)
σ	Conductivity ($\Omega^{-1}\mathrm{m}^{-1}$)
σ_{ns}	Surface energy of a superconducting-normal boundary (J)
Φ	Magnetic flux (SI - Wb, Gaussian - G.cm^2)
Φ_0	Magnetic flux quantum (SI - $h/2e$, Gaussian - $hc/2e$)
φ	Angle between the junction plane and direction of the magnetic field
φ_p	Phase difference (dimensionless)
χ	Magnetic susceptibility $\equiv \frac{dM}{dH}$ (dimensionless)
Ψ_i	Superconductor wavefunction ($\mathrm{m}^{-3/2}$)
ψ	Wavefunction ($\mathrm{m}^{-3/2}$)
ψ_r	Root-mean-squared relative fluctuation of j_c in the average GBJ
ω_D	Debye frequency (rad/s)

Acronyms

Ag	Silver
BCS	Bardeen, Cooper and Schrieffer
BSCOO	Ba-Sr-Ca-Cu-O (HTS)
CSM	Critical state model
EDX	Energy Dispersive X-Ray Analysis
GB	Grain-boundary
GBJ	Grain-boundary Josephson junction
GL	Ginzburg and Landau
HTS	High temperature cuprate oxide superconductor
JJN	Josephson junction network
MgB_2	Magnesium diboride, conventional superconductor
PIT	Powder in tube
PID	Proportional integral differential
RF	Radio frequency
SEM	Scanning electron microscope
SIS	Superconductor insulator superconductor junction
SNS	Superconductor normal superconductor junction
SQUID	Superconducting quantum interference device
VSM	Vibrating sample magnetometer
Y211	$Y_2Ba_1Cu_1O$
Y123	$YBa_2Cu_3O_{7-x}$ (HTS)
YBCO	$YBa_2Cu_3O_{7-x}$ (HTS)
Yb123	$YbBa_2Cu_3O_{7-x}$ (HTS)
Yb211	$Yb_2Ba_1Cu_1O$

Contents

List of Tables

List of Figures

Chapter 1

Superconductivity

1.1 Introduction

In 1911, a complete loss of electrical resistance to the flow of direct current was observed by Heike Kamerlingh Onnes [1] in the metal mercury when cooled below a critical temperature $T_c \approx 4.2$ K . This marked the discovery of the superconducting state[1]. Presently there are tens of elements and hundreds of compounds that exhibit the superconducting state. Superconductivity, however, is not only the property of zero resistance to electrical current - it is also the complete exclusion of magnetic flux (perfect diamagnetism); referred to as the Meissner effect, which is named after (and discovered by) Meissner and Ochsenfeld[2].

In 1957, in a theoretical study of the effects of an applied magnetic field on superconductors, Alexi Abrikosov[3] discovered that there are two types of superconductors: type-I, where magnetic flux is completely expelled from the interior for values less than some critical value; and type-II, where the magnetic flux is only expelled for small fields (below H_{c1}) and partially in higher external fields (up to H_{c2}). It is this latter state of type-II superconductors, the so-called 'mixed state', that enables superconductors to sustain fields higher than 10 Tesla, making them viable in practical applications.

Application of superconducting material in high current (thousands of amperes) and high magnetic field environments requires specific technological and economic criteria to be achieved.

[1] The name 'superconductor' was proposed by Onnes.

A significant milestone in this regard was the remarkable discovery of high-temperature copper oxide superconductors (HTSs) by Bednorz and Müller [4] in 1986. This new class of superconducting material unlocked the enormous potential for applications at temperatures above 77 K, the boiling point of liquid nitrogen. The significance here is the reduction of the expensive operational complexities associated with the cryogen, which typically has been expensive liquid helium. Currently the HTS, $HgBa_2Ca_2Cu_3O_8$, holds the record for the highest $T_c \approx 130$ K and up to 160 K under pressure [**5**]. Table 1-1 on the following page highlights important events in the history of superconductors.

From a theoretical and technological point of view, HTS materials offer the scientific and engineering communities a number of challenges. Theses challenges range from the fact that HTS materials are brittle (being ceramic and micaceous in nature, which is clearly a problem when superconducting cables are to be fabricated) to a lack of complete understanding of the mechanism of superconductivity in HTS [6]. A significant challenge is the fact that HTS material is highly anisotropic, both structurally and electrically. This implies that applied transport current or magnetic field varies depending on crystallographic orientation, hence processing techniques involving HTS material in the form of wires/tapes and bulk monolithic forms, must take this structural anisotropy into account and textured material must be produced to maximise superconducting properties.

Table 1.1: A historical perspective of superconductivity

Date	Event
1911	Superconductivity discovered by H. K. Onnes§[1], in Mercury ($T_c \approx 4.2$ K).
1912	Onnes discovers that a critical magnetic field will destroy superconductivity.
1933	†Meissner and Ochsenfeld[2] discover that superconductors are perfectly diamagnetic; a property that cannot be derived from its infinite conductivity.
1935	†The London brothers[7] use the idea of a two fluid model to describe current and field distributions within a superconductor and propose the idea of a magnetic penetration depth.
1950	†§Ginzburg and Landau[8] publish a phenomenological theory of superconductivity (GL theory) using Landau's 2nd order theory with an order parameter for the superconductivity state.
1955	‡Bardeen, Cooper and Schrieffer§(BCS)[9] develop a microscopic theory of conventional superconductivity based on a condensation of electrons into Cooper pairs - a pair of coupled electrons.
1957	†Based on GL theory, §Abrikosov[3] distinguishes between type-I and type-II superconductivity; he proposes that flux enters a type-II superconductor in the form of quantised flux lines, which are arranged in a regular lattice.
1962	Giaever§[10] considers the possibility of quantum tunnelling of Cooper pairs through an insulator barrier to be unlikely; while Josephson§[11] predicts the opposite. Josephson's prediction is later experimentally verified by Anderson and Rowell[12]
1986	§Bednorz and Müller[4] discover superconductivity in a ceramic (La-Ba-Cu-O) with $T_c \approx 35$ K. BCS theory apparently does not apply to the new **oxide superconductors**.
1987	†Wu *et al*[13] discover Y-Ba-Cu-O, a superconductor with $T_c = 92$ K, greater than the boiling point of liquid nitrogen (77 K), an inexpensive cryogen.
2001	Akimitsu *et al* [14-15] discover superconductivity in MgB_2 with $T_c = 39$ K, the highest critical temperature for a conventional BCS superconductor.
	§Received Nobel prizes for their discovery. †Reviewed later in this chapter.

In bulk polycrystalline HTS, consisting of a mosaic of crystalline grains, the critical supercurrent density, J_c, is generally determined by the properties of grain boundaries[2] (GBs) in the material. GBs can form areas of resistance or 'weak-links' to current flow, which follows percolation paths determined by low-energy GBs. This ultimately suppresses J_c. The J_c of each individual GB varies by several orders of magnitude (in the range zero to thousands A/cm^2) depending on the structural parameters of GBs [16-21] and other factors. The misorientation angle (the angle between equivalent atomic planes in adjacent grains), misorientation axis (the

[2] A grain-boundary is an interface-type structure consisting of two joined crystals.

axis around which one grain has to be rotated to coincide with the other adjacent grain) and GB planes (the atomic planes parallel to the interface and forming that interface), are considered the most important 'macroscopic' structural parameters. A misorientation angle of 10^0 typically leads to an order of magnitude decrease in J_c (intergranular)[16]. Other than the misorientation angle, GBs can be classified according to several different appropriate parameters, such as segregation of impurities, charge carrier concentration, oxygen stoichiometry and dislocation density. The electrical and mechanical properties of a material can be altered via the process of doping. It is the doping of polycrystalline HTSs, in particular GBs, that forms the main focus of this study, where the HTS material of choice is $YBa_2Cu_3O_{7-x}$ (abbreviated YBCO), which has a $T_c \approx 92$ K.

This thesis is presented in cgs units, which are the preferred units in publications in this field.

1.2 Organisation of Thesis

Chapter 1 begins with an introduction to phenomenological theories of superconductivity, which includes the London model, the Ginzburg-Landau (GL) theory, and a brief summary of key elements of the microscopic Bardeen, Cooper and Schrieffer (BCS) theory that are relevant to this study. The chapter ends with a discussion of various characteristic properties of superconductors.

Chapter 2 is dedicated to a discussion of high-temperature superconductivity, the system of choice for this study. The structural uniqueness of this system's superconducting two-dimensional copper oxide planes is explained as a source of its anisotropic nature. The chapter includes discussions of the so-called 'weak-link' effect, which originates from grain-boundaries acting as Josephson junctions[3] - the grain boundary Josephson junction (GBJ). It is the GBJ's sensitivity to magnetic fields that limits the transport current of HTS's.

The chapter ends with a discussion of the global HTS market, with brief discussions on the potential applications in bulk/large current, and microelectronic/small current devices.

Chapter 3 introduces the granularity properties of HTS's, beginning with experimental

[3]To be defined later.

evidence for the percolation nature of the supercurrent. Distinctions between intergranular and intragranular current are made, with an emphasis on the role of intergranular structural irregularities and their effect on the intergranular critical current density. A hypothesis that grain-boundaries, acting as Josephson junctions, have a nonuniform random Josephson current profile is used in the development of an intergranular critical state model (CSM), which is used in the analysis of isothermal magnetisation measurements. It is through the model's various fitting parameters that insight is gained into the nature of GBJs. The chapter ends with a discussion of the derivation of an average granular magnetic penetration depth determined from high-field isothermal magnetisation measurements.

Chapter 4 presents the experimental techniques and specimen preparation methods used in the present research. Results of magnetisation low-field, high-field and resistance measurements are presented.

Chapter 5 concentrates on numerical analyses of the low-field and high-field magnetisation data presented in Chapter 4. The various CSM fitting parameters, along with an average granular penetration depth derived from high-field measurements, are compared with theory and appropriate models. The latter fits yield, inter alia, values for various characteristic lengths of the average GBJ and they offer insight into the effect of silver doping on the YBCO system.

Using conclusions from the analysis in Chapter 5 (in particular, that optimum Ag doping can achieve better GBJ connectivity), Chapter 6 introduces experimentation in the development of various HTS solders for the joining of large single-domain YBCO specimens.

Chapter 7 presents conclusions and discusses current doping experiments. It is suggested that the methodology presented in this thesis may help in further improvements of GBJs in HTS systems.

1.3 Original Contributions in the Thesis

The original contributions in this thesis include:

1. The use and adaptation of a number of models, in particular a critical state model, as a diagnostic tool to understand why Ag doping improves the intergranular critical current of the polycrystalline YBCO HTS system. The behaviour of various fitting parameters, in particular

a magnetic field-independent critical current, which is sensitive to grain boundary junction microstructure, gives unique insight into why Ag doping improves the intergranular critical current density of YBCO.

2. The success of the Ag doping experiments implies the establishment of a new methodology in understanding the effects of other intergranular doping experiments.

3. The establishment of a unique method to estimate the size of strongly coupled grains (cluster) from high-field magnetic measurements. The cluster size, along with derived values for the penetration depth, helped constrain the critical state model.

4. The explanation of why Ag doping improves the critical current in polycrystalline YBCO supports experiments done by other researchers; that is, Ag is a useful 'additive' in the joining of large single domain YBCO.

5. The author suspects that there is a fundamental relationship between the field-independent (plateau) component of the transport critical current and the *d*-wave nature of HTS (see Section 3.2.1). [This is more of a comment than a contribution claim.]

1.4 Summary of Theories of Superconductivity

Superconductors contain superfluid, consisting of coupled pairs of electrons (or holes in HTSs), called Cooper pairs. Cooper pairs are named after one of the Physics Nobel laureates in the Bardeen, Cooper and Schrieffer (BCS) theory. The BCS theory describes on a microscopic level the mechanism of superconductivity in conventional superconductors [9]. In 1935 Fritz London conjectured, correctly, that a superconductor can be understood as a giant macroscopic atom (quantum state), where the superconducting ground state and normal non-superconducting state are separated by an energy gap [7]. A key prediction of the BCS theory was that of a minimum energy required to break a Cooper pair, $2\Delta(T)$, where Δ is known as the gap parameter. The gap parameter is dependent on temperature ranging from a minimum of zero at T_c to a maximum at $T = 0$ K; $2\Delta(0) = 3.528 k_B T_c$ where k_B is Boltzmann constant. At absolute zero, all electrons are paired, but as temperature increases electron pairs begin to unpair, resulting in the superconducting state comprising of single electrons ('excitations') and

paired electrons[4] - a supercurrent effectively 'shorts' the effect of single unpaired electrons.

When cooled below T_c, the conductive gas of electrons (fermions) in a superconductor is condensed into a Bose-Einstein condensate consisting of a quantum fluid of highly correlated Cooper pairs (bosons). A Cooper pair consists of weakly coupled electrons with opposite momentum and spin. Based on the BCS theory, lattice vibrations (phonons) play an 'intermediate' role, providing a mechanism of attraction for the negatively charged electrons.

Perfect conductivity is a direct consequence of the quantum nature of superconductivity on a macroscopic level. Cooper pairs, unlike single electrons, obey Bose-Einstein statistics which allow all paired electrons to be in the same state. Instead of each single electron in a metal having its own wavefunction (and wavelength), a superconductor has all its charge carriers (Cooper pairs) described by a single macroscopic wavefunction. The Cooper pairs have a net momentum of zero as they are comprised of electrons with equal and opposite momentum (and spin). Hence, the associated de Broglie wavelength of the entire coherent ensemble of Cooper pairs is infinite compared to the scale of the superconductor, and cannot be scattered by the normal scatters of single electrons.

An alternative explanation of perfect conductivity, is that once electrons condense into Cooper pairs, thus becoming bosons, they 'gather' in the ground state (lowest energy level) - Bose Einsein condensate. The nature of this condensate is such that the larger the number of bosons collecting in the ground state the more difficult it is for a boson to leave or overcome the 'resistance' of the condensate in order to interact and be scattered by a defect.

1.4.1 Superconductivity - second order transition

In the absence of a magnetic field the transition from normal to superconducting state at T_c is a second-order transition[5], due to the fact that entropy at the transition temperature is continuous. A general theory related to second order phase transitions was formulated by Lev Landau [22].

The fact that the superconducting state is preferred over the normal state below a certain critical temperature T_c, means that it is a lower energy state. The state of a superconductor

[4] Cooper pairs can also be 'ionised' (unpair) into the normal state via photo-ionisation with electromagnetic radiation energies $hf > 2\Delta$, where h is Planck's constant and f the frequency of the radiation.

[5] A first order transition occurs in the presence of a magnetic field.

is not only sensitive to temperature but also to magnetic field; above a critical value H_c the superconductor changes state to the normal state. Strictly, this is for type -I superconductor, and it implies that when a superconductor experiences an applied field equal to the critical field H_c, the Gibbs free energy $G(H,T)$ of the normal and superconducting states must be equal:

$$G_n(H_c,T) = G_s(H_c,T). \tag{1.1}$$

The change in the superconducting Gibbs free energy from zero applied field to H_c is given by

$$G_s(H_c,T) = G_s(0,T) - \int_0^{H_c} \mu_0 M dH, \tag{1.2}$$

where $\int_0^{H_c} \mu_0 M dH$ is the magnetic energy of the superconducting state, M is the magnetisation and μ_0 is the permeability of free space. For the superconducting Meissner state $M = -H$, and we obtain from Equation 1.2, assuming negligible demagnetisation factor and integrating,

$$G_s(H_c,T) = G_s(0,T) + \frac{\mu_0 H_c^2}{2}. \tag{1.3}$$

If we neglect the magnetic susceptibility χ of the normal state

$$G_n(H_c,T) = G_n(0,T),$$

and hence Equation 1.1 becomes

$$G_n(0,T) - G_s(0,T) = \frac{1}{2}\mu_0 H_c^2. \tag{1.4}$$

The right-hand-side of Equation 1.4 gives a thermodynamic description of the Meissner effect, it is the energy of exclusion of the magnetic field from a superconductor. A similar relation may be derived for type-II superconductors. Instead of the assumption of $M = -H$, as in the case of type-I, a substitution of $M = -f(H)$ is made where $f(H)$ is the function describing the type-II reversible magnetisation curve; this is discussed further in Section 1.4.

For type-I superconductors, the temperature dependence of the critical field $H_c(T)$ is found

experimentally to be given approximately by

$$H_c(T) = H_{c0}\left[1 - \left(\frac{T}{T_c}\right)^2\right], \text{ with } T \leq T_c, \tag{1.5}$$

where H_{c0} is the critical field at $T = 0$ K.

Applying the relation for entropy, $S = -\left(\frac{\partial G}{\partial T}\right)_H$, to Equation 1.4, we obtain

$$S_n(0,T) - S_s(0,T) = \mu_0 H_c \frac{dH_c}{dT}.$$

If T approaches T_c, H_c approaches 0 and $S_n(T_c) = S_s(T_c)$. This shows the entropy is continuous at T_c, hence Landau's second-order transition theory can be applied to superconductivity.

In 1950, Ginzburg and Landau[8] applied an adapted form of Landau's general theory of phase transition to superconductivity: this is know as the Ginzburg-Landau (GL) theory [23]. The GL theory is a phenomenological theory which successfully explains the electrodynamics, quantum mechanics and thermodynamic properties of superconductors; it will be more closely reviewed in the section on the Ginzburg-Landau theory of this chapter.

1.4.2 The London equations

The first useful theory of superconductivity was the phenomenological London theory. This theory introduces two equations in addition to Maxwell's equations to describe the electrodynamics of superconductors.

In 1935 the brothers F. and H. London suggested two equations to describe the magnetic and electric fields in a superconductor [7]. To describe the superconducting property of flux expulsion they could modify either Maxwell's equations or Ohm's law. For example, analysing the combination of Ohm's law and the experimentally observed infinite conductivity implied a flux preserving material, i.e. magnetic flux would be frozen into a superconductor, and not a flux expelling material (which was experimentally observed). The brothers chose to modify Ohm's law appropriately to describe superconductivity. An interesting result from the Londons' model is that of a magnetic penetration depth parameter, λ_L, which is a function of intrinsic properties of the superconductor. The parameter implies that in order for the Meissner effect to occur, a sheet of supercurrent must flow within a depth λ_L from the surface of a superconductor;

essentially the current generates a magnetic field which is equal and opposite to the applied field, hence screening out the applied field from the rest of the material.

The London model uses a two-fluid approach, where the total density n of electrons is made up of a 'fluid' of normal electrons, n_n, and of superconducting electrons, n_s, with associated particle average or 'drift' velocities $\mathbf{v}_n$ and $\mathbf{v}_s$. The assumptions made about the superfluid electrons are that they were not scattered and are freely accelerated by an electric field, thus shorting out the effect of the normal resistive electrons.

The acceleration of a superelectron in an electric field $\mathbf{E}$ can be described by the equation of motion:

$$\mathbf{F} = m_e\mathbf{a} = m\frac{d\mathbf{v}_s}{dt} = e\mathbf{E}, \tag{1.6}$$

where e is the charge and m_e the mass of an electron. The supercurrent density is defined by,

$$\mathbf{J} = n_s e\mathbf{v}_s. \tag{1.7}$$

Differentiating Equation 1.7 with respect to time and combining the result with Equation 1.6 results in the first London equation:

$$\frac{d\mathbf{J}}{dt} = \frac{n_s e^2}{m_e}\mathbf{E}. \tag{1.8}$$

The above London equation describes the infinite conductivity of a superconductor, where the supercurrent has an inductive relationship with electric field, $\mathbf{E}$, and directly contradicts Ohm's law where $\mathbf{J} \propto \mathbf{E}$.

Combining the first London equation with the Maxwell equation $\nabla \times \mathbf{E} = -\frac{d\mathbf{B}}{dt}$, we obtain:

$$\frac{d}{dt}\left(\nabla \times \mathbf{J} + \frac{n_s e^2}{m_e}\mathbf{B}\right) = 0 \tag{1.9}$$

The London brothers noticed that when Equation 1.9 is combined with Ohm's law and infinite conductivity is assumed the magnetic flux is 'frozen' into the material that is $\frac{d\mathbf{B}}{dt} = 0$. This is not the Meissner effect and therefore does not describe superconductors. To overcome this

dilemma they integrated Equation 1.9 giving:

$$\nabla \times \mathbf{J} + \frac{n_s e^2}{m_e} \mathbf{B} = 0, \tag{1.10}$$

the second London equation.

The second London equation describes the condition that $\mathbf{B} = 0$ at all times in a type-I superconductor and leads to a parameter, λ_L, known as a London penetration depth. Insight into the mechanism of how the Meissner effect is established is derived from the combination of Equation 1.10 and applying the curl operator on both sides of the Maxwell equation, $\mathbf{J} = \nabla \times \mathbf{B}/\mu_0$ (Ampere's Law)[6]:

$$\mathbf{B} + \lambda_L^2 \left[\nabla \times \nabla \times \mathbf{B}\right] = 0, \tag{1.11}$$

where λ_L is identified as the London penetration depth and equals,

$$\lambda_L = \left(\frac{m_e}{\mu_0 n_s e^2} \right)^{1/2}. \tag{1.12}$$

Considering the one-dimensional case in Equation 1.11 with x-axis perpendicular to the superconductor, an expression for the magnetic field distribution in the x direction for a superconducting half-slab can be derived:

$$\mathbf{B}_z(x) = -\lambda_L^2 \frac{d^2 \mathbf{B}_z(x)}{dx^2}, \tag{1.13}$$

the physical solution for which is:

$$\mathbf{B}_z(x) = \frac{\mathbf{B}_z(0)}{\cosh\left(\frac{x}{\lambda_L}\right)}. \tag{1.14}$$

This demonstrates the fact that the magnetic field in the bulk of the superconductor decreases to zero, thus describing the Meissner effect.

[6]Static field $\mathbf{B}$ is assumed here.

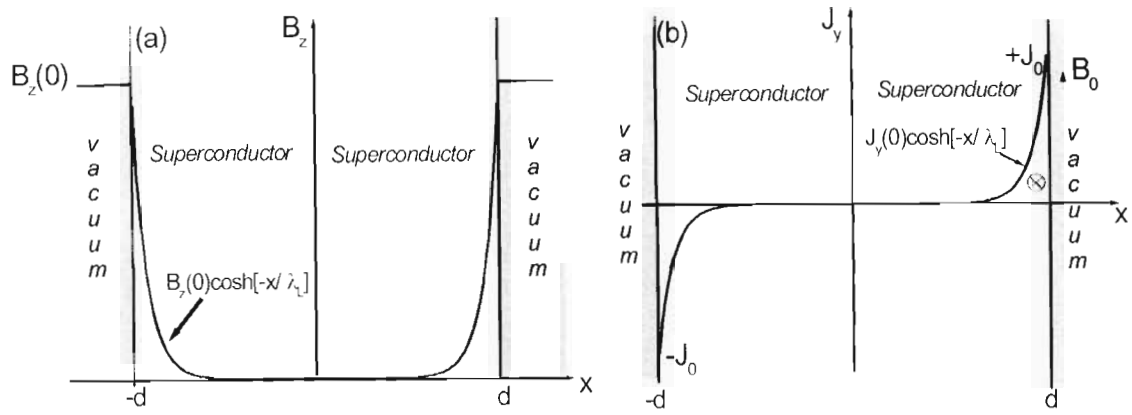

Figure 1-1: (a) London equations predict an exponentially decaying field penetration into a superconductor. (b) The screening supercurrent distribution calculated from the field distribution.

The supercurrent distribution can be shown to vary as:

$$\mathbf{J}_y = \mathbf{J}_y(0) \cosh\left(\frac{-x}{\lambda_L}\right), \tag{1.15}$$

and this demonstrates that magnetic field is screened out of a superconductor by an opposite field induced by surface supercurrents, which are confined within a depth of order λ_L. The field and current in the above one-dimensional case are plotted as a function of distance in Figure 1-1.

The approximate temperature dependence of λ_L is found empirically when combined with the Gorter and Casimir temperature dependence of the density of superconducting electrons [24], giving

$$\lambda_L(T) \approx \frac{\lambda_L(0)}{\left[1 - \left(\frac{T}{T_c}\right)^4\right]^{1/2}}. \tag{1.16}$$

Hence the penetration depth approaches infinity as the temperature tends towards T_c.

Coherence length

As an aside to the London theory, another important characteristic length, in addition to the penetration depth, is the coherence length, ξ. It is interesting to note that the London approach neglects this length. Due to the use of the single electron equation of motion, Equation 1.6, the London model is based on a local approach, and hence on the local carrier density of supercurrent. However, this local approach is not generally valid, especially when considering type-I superconductors, although it is a good approximation for extreme type-II superconductors.

Before the discovery of the electron pairing mechanism, the Londons' incorrect local approach to the study of type-I superconductors was recognised by Pippard [25]. He introduced a measure, the coherence length ξ, based on the quantum uncertainty principle - $\Delta x \Delta p \gtrsim h$, where large spatial variations of the wavefunction can occur within an interval Δx and large variations of electron momentum within an interval Δp ($\hbar = \frac{h}{2\pi}$ where h is Planck's constant). The momentum range of the electrons that condense into the superconducting state at T_c with a Fermi velocity v_F, that is within approximately $k_B T_c$ of the Fermi energy, is $\Delta p \approx k_B T_c / v_F$. Substituting for Δp into the uncertainty principle we get

$$\Delta x \gtrsim \hbar / \Delta p \approx \hbar v_F / k_B T_c.$$

In fact, the correct result established in the BCS theory [9] leads to the expression for the coherence length,

$$\xi_0 = \frac{\hbar v_F}{\pi \Delta_0}, \tag{1.17}$$

where $\Delta_0 \approx k_B T_c$ is the BCS energy gap at $T = 0$ K, which will be discussed further in Section 1.3.5. From tunneling or optical measurements the energy gap is determined and hence so is the coherence length.

Pippard found that this non-local length scale, the so-called Pippard coherence length, had a magnitude of approximately $\xi_p \approx 10^{-6}$ m. The Pippard coherence length can be expressed in terms of the BCS coherence length, ξ_0, and the electron mean free path, l_e, as:

$$\frac{1}{\xi_p} = \frac{1}{\xi_0} + \frac{1}{\alpha l_e}, \tag{1.18}$$

where α is a constant of order unity.

Pippard, through his non-local generalisation, modified the London equations and determined the field and current distribution within a type-I superconductor more accurately. Experimentally, Equation 1.18 can be verified by the inclusion of impurities in a superconductor, thus decreasing l_e and thereby decreasing ξ_p. An interesting result from the these experiments was that the penetration depth increases appreciably as l_e becomes less than ξ_0 and hence a type-II like behaviour may be achieved by suitable microstructural modification of an otherwise type-I superconductor.

The non-local modifications to the London model only apply where the magnetic screening takes place in a region where the carrier density may vary locally within the coherence volume, that is, $\xi_0 \gg \lambda$ (this relationship holds for type-I superconductors). If $\lambda \gg \xi_0$(type-II superconductors), then a non-local approach is not necessary and the original London equations more sufficiently describe the magnetic field penetration at a superconductor boundary.

1.4.3 Free energy in the London model

Using a thermodynamic approach similar to that used to describe superconductivity in Section 1.3.1., the London equations can be derived by minimising the free energy contributions of the superconducting state. This derivation will serve as an introduction to the free energy concepts of the Ginzburg-Landau (GL) [8] theory.

The free energy of a superconductor, with screening currents $\mathbf{J}(\mathbf{r})$ and local field $\mathbf{h}(\mathbf{r})$, can be written as,

$$G = \int_V G_s(\mathbf{r}) d^3\mathbf{r} + E_{kin} + E_{mag}. \tag{1.19}$$

The terms on the right-hand-side of this equation represent, respectively, the condensation energy, kinetic energy of the screening current and the magnetic energy.

Using the London penetration depth, $\lambda_L = \left(\frac{m_e}{\mu_0 n_s e^2}\right)^{1/2}$, and the definition of the supercurrent, the kinetic energy term can be written as,

$$E_{kin} = \int_V \frac{1}{2} m_e n_s \mathbf{v}_s(\mathbf{r}) d^3\mathbf{r} = \frac{\mu_0}{2} \int \lambda_L^2 \mathbf{J}^2(\mathbf{r}) d^3\mathbf{r}, \tag{1.20}$$

where $\mathbf{v}_s(\mathbf{r})$ is the velocity of the superconducting electrons at a point $\mathbf{r}$. The magnetic energy

term is given by

$$E_{mag} = \frac{\mu_0}{2} \int_V \mathbf{h}^2(\mathbf{r}) d^3\mathbf{r}, \tag{1.21}$$

where $\mathbf{h}(\mathbf{r})$ is the local field at $\mathbf{r}$.

Substituting Equation 1.20 and Equation 1.21 into Equation 1.19 we get:

$$G = \int_V d^3\mathbf{r} \left[G_s(\mathbf{r}) + \frac{\mu_0}{2} \lambda_L^2 \mathbf{J}^2(\mathbf{r}) + \frac{\mu_0}{2} \mathbf{h}^2(\mathbf{r}) \right]. \tag{1.22}$$

Using Maxwell's equation, $\mathbf{J}(\mathbf{r}) = \nabla \times \mathbf{h}(\mathbf{r})$, yields the following expression:

$$G = G_0 + \frac{\mu_0}{2} \int_V d^3\mathbf{r} \left[\lambda_L^2 \left(\nabla \times \mathbf{h}(\mathbf{r}) \right)^2 + \mathbf{h}^2(\mathbf{r}) \right],$$

where G_0 is the total condensation energy and the first term of the integral expression represents the kinetic energy of the electrons and the second term the magnetic energy. Minimising the terms in the square brackets in the energy equation with respect to $\mathbf{h}(\mathbf{r})$ gives,

$$\mathbf{h}(\mathbf{r}) + \lambda_L^2 \left[\nabla \times \nabla \times \mathbf{h}(\mathbf{r}) \right] = 0, \tag{1.23}$$

which is the London equation, Equation 1.11, that was derived using an electrodynamic approach. Thus, if the number of superconducting electrons remains constant, the London equation represents the field distribution which minimises the sum of the kinetic energy of the supercurrent and the magnetic energy.

1.4.4 The Ginzburg-Landau (GL) theory

The BCS microscopic theory has its limits when considering spatial inhomogeneities in superconductors, while the London theory does not consider quantum effects. The first quantum theory of superconductivity is the Ginzburg-Landau (GL) theory (phenomenologically based) [8]. Based on electrodynamics, quantum mechanics and a thermodynamic description (similar to that used in the London theory), the GL theory is better equipped to deal with spatial inhomogeneities. For example, the observation of magnetic flux penetrating the interior of a type-II superconductor implies that the superconducting carrier density must vary and hence it is not constant throughout the material. GL theory predicts type-II superconducting behaviour and

quantisation of magnetic vortices [3], making it a very successful theory. Developed in 1950 by Vitaly Ginzburg and Lev Landau, the GL theory remained popular only in the Soviet Union for close on a decade until L.P. Gorkov showed that it could be derived from the BCS theory [26].

The GL theory is based on a two-fluid approach: the total density of electrons, n, in a superconductor consists of superconducting electrons, n_s, and non-superconducting electrons, $n-n_s$. The theory uses a phenomenological approach based on Landau's theory of second order phase transitions, and uses a macroscopic wave function, $\psi(r) = |\psi(\mathbf{r})|\, e^{i\varphi_p(\mathbf{r})}$, instead of the magnetisation M found in the Landau approach [22]. Prior to the BCS theory, the wave function was used as an order parameter to describe the centre of mass of the superconducting electrons. It is now interpreted as the centre of mass function of the Cooper pairs. The magnitude of the wavefunction $\psi(\mathbf{r})$ is normalised such that $|\psi|^2 \propto n_s$ and the phase $\varphi_p(\mathbf{r})$ is related to the supercurrent.

The basic postulate of GL theory is that ψ is small[7] and varies slowly in space, and that the free energy of the system can be expanded as a power series in terms of $|\psi|^2$,

$$G_s(\mathbf{r},T) = G_n(\mathbf{r},T) + \alpha\,|\psi|^2 + \frac{\beta}{2}\,|\psi|^4 + \frac{1}{2m_e^*}\,|(-i\hbar\nabla - e^*\mathbf{A}_p)\,\psi|^2 + \frac{\mu_0\mathbf{h}^2}{2}, \tag{1.24}$$

$$G_s(T) = \int_V G_s(\mathbf{r},T)d^3r, \tag{1.25}$$

where subscripts n and s represent the normal and superconducting state respectively, $\hbar = \frac{h}{2\pi}$, where h is Planck's constant, A_p is the vector potential of the magnetic field (thus $\mu_0\mathbf{h} = \nabla\times\mathbf{A}_p$) and V is the volume of the specimen. Cooper pairs had not been identified as charge carriers of superconductors when the GL theory was formulated; this summary assumes their existence and therefore takes $e^* = 2e$ and $m_e^* = 2m_e$. The first term on the right hand-side of Equation 1.24 describes the normal-state free energy, the second and third terms contain the power-law expansion of the superfluid condensation energy in terms of $|\psi|^2$, the fourth term represents the kinetic energy of the superelectrons, and the final term represents the magnetic screening contribution to the free energy, all per unit volume. The parameters α and β will be discussed

[7] For example, near T_c.

further in the following sections.

Substituting the modulus and phase of the order parameter into Equations 1.24 and 1.25 yields,

$$G_s(\mathbf{r},T) = G_n(\mathbf{r},T) + \alpha|\psi|^2 + \frac{\beta}{2}|\psi|^4 + \frac{\hbar}{2m_e^*}(\nabla|\psi|)^2 + \frac{1}{2}|\psi|^2 m_e^* \mathbf{v}_s^2 + \frac{\mu_0 \mathbf{h}^2(\mathbf{r})}{2}, \tag{1.26}$$

where $\mathbf{v}_s$ is defined as

$$\mathbf{v}_s = \frac{1}{2m_e^*}\left(\hbar\nabla\varphi_p - e^*\mathbf{A}_p\right). \tag{1.27}$$

In order to determine $\psi(\mathbf{r})$ and $\mathbf{A}_p$, Equation 1.24 is minimised with respect to both $\psi(\mathbf{r})$ and $\mathbf{A}_p$. This results in the Ginzburg-Landau equations:

$$\alpha\psi + \beta|\psi|^2\psi + \frac{1}{2m_e^*}(-i\hbar\nabla - e^*\mathbf{A}_p)^2\psi = 0, \tag{1.28}$$

$$\mathbf{J} = \nabla \times \mathbf{h} = \frac{e^*}{m_e^*}\left[\psi^*(-i\hbar\nabla - e^*\mathbf{A}_p)\psi\right]. \tag{1.29}$$

The first GL equation, Equation 1.28, describes the order parameter while the second GL equation, Equation 1.29, the supercurrent. Given specific conditions the GL equations can provide a good understanding of superconductivity in terms of a few parameters. This will be outlined in the following subsections.

Thermodynamic critical field, H_c

The GL free energy function, Equation 1.24, introduces two phenomenological parameters: α and β. Just as in the Landau theory [22], α is approximated by a first order Taylor expansion, that is, $\alpha = a(T - T_c)$ and is positive in the normal state and negative in the superconducting state, while β is a positive constant independent of temperature. The London theory results from the minimisation of Equation 1.24, if the first, second and third terms of Equation 1.24 can be assumed to be constant, that is, if the order parameter does not vary in space. In the absence of a magnetic field and if the phase of the order parameter is constant[8], then the fourth and fifth terms of Equation 1.24 are zero, and the energy difference between the n and s-state

[8]Constant phase implies no current. This association will be discussed further later.

becomes:

$$G_s(\psi,T) - G_n(\psi,T) = G(\psi,T) = \alpha(T)\,|\psi|^2 + \frac{1}{2}\beta\,|\psi|^4\,. \tag{1.30}$$

Minimising with respect to $|\psi|^2$ gives:

$$\frac{dG(\psi,T)}{d\,|\psi|^2} = \alpha(T) + \beta\,|\psi|^2 = 0, \tag{1.31}$$

and hence

$$|\psi|^2 = -\frac{\alpha(T)}{\beta}. \tag{1.32}$$

Substituting back into Equation 1.24 results in the following expression for the free energy difference per unit volume of superconductor, in the absence of fields and currents:

$$G_s - G_n = -\frac{\alpha^2(T)}{2\beta} = \frac{\mu_0 H_c^2}{2}. \tag{1.33}$$

Penetration depth, λ

Assuming a small magnetic field and neglecting variations of the order parameter ψ, the second GL equation, Equation 1.29 reduces to:

$$\nabla \times \mathbf{h} = -\frac{e^{*2}\,|\psi|^2}{m_e^*}\mathbf{A}_p. \tag{1.34}$$

This equation reduces to the London equations (Equations 1.11 and 1.23) when taking the curl of it and using $\mathbf{h}(\mathbf{r}) = \nabla \times \mathbf{A}_p$. The penetration depth can be identified as,

$$\lambda^2 = \frac{m_e^*}{\mu_0 e^{*2}}\frac{1}{|\psi|^2}. \tag{1.35}$$

This expression for the penetration depth, in contrast to the London expression (Equation 1.12) contains a temperature-dependent quantity $|\psi|^2$, which can be in terms of $\alpha(T)$ from Equation 1.32[9]. The resulting temperature dependence of the penetration depth is:

$$\lambda^2 \propto \frac{1}{T_c - T}. \tag{1.36}$$

[9]Only for temperatures approaching T_c where GL theory is valid.

Coherence length, ξ

Within the GL theory, the coherence length ξ_{GL} is defined as a measure of the distance over which the order parameter varies, that is, ψ increasing from zero to its maximum over a distance ξ_{GL}.

The definition of the coherence length originates from the first GL equation; consider the one-dimensional case in the absence of a magnetic field, Equation 1.28 becomes:

$$-\frac{\hbar^2}{2m_e^*}\frac{d^2\psi}{dx^2} + \alpha\psi + \beta|\psi|^2\psi = 0 \tag{1.37}$$

The above equation has a physically acceptable solution

$$\psi = \psi_0\left[1 - \exp\left(-\frac{\sqrt{2}x}{\xi_{GL}(T)}\right)\right], \tag{1.38}$$

where the parameter $\xi_{GL}(T)$ is defined as

$$\xi_{GL}(T) = \frac{\hbar^2}{2m_e^*|\alpha|}. \tag{1.39}$$

Hence, the order parameter establishes itself exponentially over a characteristic length scale $\xi_{GL}(T)$, the GL coherence length.

Other important relations in the GL theory

The ratio of the penetration depth λ and the coherence length ξ_{GL} define the GL-parameter,

$$\kappa = \frac{\lambda}{\xi_{GL}} \tag{1.40}$$

The GL-parameter is independent of temperature due to the fact that both characteristic lengths diverge as $|\alpha|^{-1/2}$ as $T \to T_c$. The GL-parameter is an important parameter that categories superconducting material into either type-I ($\kappa < 1/\sqrt{2}$) or type-II superconductors ($\kappa > 1/\sqrt{2}$) near T_c.

The parameters α and β introduced in the GL theory can be expressed in terms of the experimentally measurable quantities H_c and λ; by suitable substitutions of Equation 1.32,

Equation 1.33 and Equation 1.35, that is:

$$\alpha = -\frac{e^{*2}}{m_e^*}\mu_0^2 H_c^2 \lambda^2 \tag{1.41}$$

$$\beta = -\left(\frac{e^{*2}}{m_e^*}\right)^2 \mu_0^3 H_c^2 \lambda^4. \tag{1.42}$$

Another important relationship between the characteristic quantities is found by combining Equation 1.33 with Equation 1.35 and Equation 1.39. This yields the result

$$H_c(T)\lambda(T)\xi(T) = \text{constant} = \frac{\hbar}{e^*\mu_0\sqrt{2}} = \frac{\Phi_0}{2\pi\mu_0\sqrt{2}},$$

where $\Phi_0 = hc/e^*$ is the flux quantum: it is the minimum amount of magnetic flux that threads a superconducting loop.

Finally, expressions for both the lower and upper critical fields, H_{c1} and H_{c2}, in terms of the thermodynamic critical field can be obtained:

$$H_{c1} = \frac{H_c}{\sqrt{2}\kappa}(\ln\kappa) \text{ and } H_{c2} = \sqrt{2}\kappa H_c, \text{ for } \kappa >> 1. \tag{1.43}$$

Surface energy, σ_{ns}, and the GL parameter, κ

The response of a type-I superconductor to an external magnetic field is different to that of a type-II superconductor, as later shown in Figure 1-5. This difference is due to surface energy effects at the interface of the superconductor and normal or vacuum regions. The surface energy is positive for a type-I superconductor and negative for a type-II superconductor.

The surface energy, σ_{ns}, of a superconducting normal boundary is defined as:

$$\sigma_{ns} = \int_{-\infty}^{\infty} (g(x) - g_n(x))\, dx, \tag{1.44}$$

where $g(x)$ is the Gibbs free energy of the system. Here we assume that $g(x)$ is equal to g_n for $x < 0$ and equal to g_s for $x > 0$. Using the relations for the free energy as detailed previously,

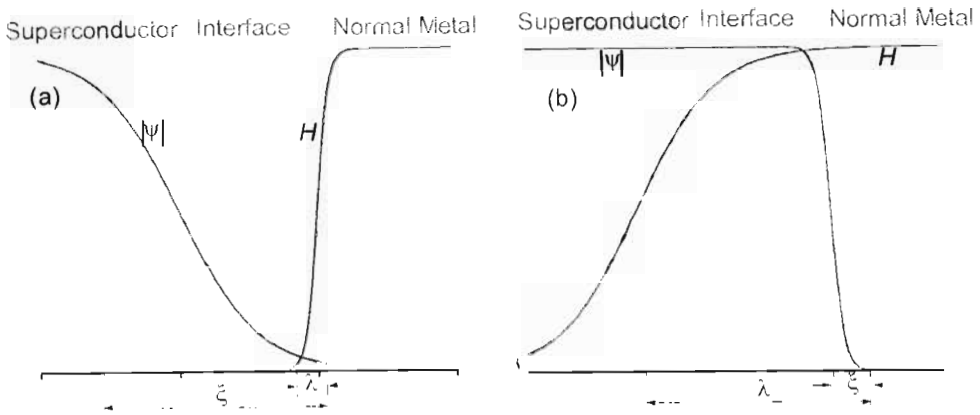

Figure 1-2: Spatial variations of the order parameter ψ(blue curves) and the magnetic field H (green curves) in the vicinity of normal-superconductor interface for (a) $\kappa << 1$ (type-I) and (b) $\kappa >> 1$ (type-II).

the final result for the free energy difference at the boundary is found to be:

$$\sigma_{ns} = \frac{\mu_0 H_c^2}{2} \int_{-\infty}^{\infty} \left[\left(1 - \frac{h}{H(0)} \right) - \left(\frac{\psi}{\psi_0} \right)^4 \right] dx. \tag{1.45}$$

Analysing the two terms within the square brackets of Equation 1.45, we note the term on the right-hand-side represents the negative contribution to the surface energy associated with the condensation energy. The left-hand-side term represents the positive contribution to the surface energy associated with the diamagnetic screening energy. Hence, the balance of the positive magnetic expulsion energy and the negative condensation energy determines the sign of σ_{ns}. Numerical calculations show that $\sigma_{ns} > 0$ for superconductors with $\kappa < \frac{1}{\sqrt{2}}$ (type-I) and $\sigma_{ns} < 0$ for superconductors with $\kappa > \frac{1}{\sqrt{2}}$ (type-II).

The numerical calculations can be interpreted physically, for two cases (i) $\kappa << 1$, i.e. $\lambda << \xi$ and (ii) $\kappa >> 1$, i.e. $\lambda >> \xi$. Figure 1-2 shows how the magnetic field, which falls off over a distance λ, and the order parameter, which falls off over a distance ξ, varies at the interface for the two cases. A comparison of magnitudes of the order parameter $|\psi|$ and the magnetic field H at certain distances ultimately define the sign of the surface energy.

In Figure 1-2 (a) there is a region where $|\psi|$ is small, with the magnetic field screened out,

and hence 'enjoys' superconducting properties. This region is free of magnetic field – in order to expel the field out of this region work must be done on the magnetic field and shift its boundary by a distance ξ. In Figure 1-2 (b) the opposite holds in that there is a region where $|\psi| \sim 1$ in a relatively large magnetic field. This implies that the energy of the system as a whole has decreased by the value of work to shift the field by a distance λ.[Unlike the previous situation, electrons in this region are coupled and hence the energy is less by the condensation energy compared to the energy in the normal region.]

Ginzburg and Landau failed to see any other relevance of the distinction between positive and negative surface energies. Later Abrikosov using the GL-theory, managed to predict that superconductors with $\sigma_{ns} < 0$, when placed into a external magnetic field above H_{c1}, would find it energetically favourable to subdivide into alternating normal and superconducting domains [3]. He also predicted that magnetic field penetrates into the superconductor in a specific way; as singly quantized vortex filaments forming a regular array. Abrikosov calculated that the array of flux lines within the type-II material would arrange in a regular square array due to inter-vortex mutual repulsion. In 1964, the structure of the magnetic lattice was correctly predicted by Kleiner, Roth and Autler [27] to be a triangular lattice . The magnetic triangular lattice was first observed experimentally by Essmann and Träuble in 1967 [28] through the decoration of ferromagnetic particles onto the surface of the superconductor in the mixed state, often referred to as the Abrikosov phase.

Flux quantisation provides supports for the assumption of a macroscopic wave function used in the GL theory. This derives from the fact that the magnetic flux quantum, not derived in this thesis, can be pictured by circulating screening current about a flux line in terms of the wave function, ψ. Here, for a superconducting path of zero electrical resistance, ψ must make an integral number of wavelengths about the circular path of radius ξ. The lowest harmonic in such a case corresponds to one complete wavelength.

Finally, the GL theory can be applied to HTS material with general success, although several fundamental aspects of these material, which will be discussed in Chapter 2, must be considered.

1.4.5 The Bardeen, Cooper and Schrieffer (BCS) theory

Unlike the London theory, GL theory took into account the macroscopic quantum nature of superconductivity; for example, considering the fact that superconductivity is a more ordered state than the normal state. In this section a summary of key elements of the microscopic BCS theory relevant to this study are introduced. It is interesting to note that in 1959 Gor'kov showed that BCS theory reduces to GL theory close to T_c [26].

A clue to the microscopic mechanism of superconductivity was the existence of permanent currents. This suggested some collective state of the conduction electrons in superconductors. Forty-six years after the discovery of superconductivity, Bardeen, Cooper and Schrieffer developed their microscopic theory [29]. The BCS theory hinges on electrons, 'coupled' together by phonons, interacting over substantial atomics distances (thousands of atomic intervals apart) to produce a coherent superconducting state [30]. Essentially, and very simplistically, an electron passes through the lattice and attracts positive ions. The shortest response time of the ions is the highest possible lattice vibration frequency, the Debye frequency ω_D. This lattice deformation attracts a second electron because of the local accumulation of positive charge. The clue to this insight came about due to the observation that the transition temperature was directly related to the mass of different isotopes of a particular superconductor and obeyed the following relation,

$$T_c M_i^a = \text{ constant}, \tag{1.46}$$

where M_i is the mass of the isotope and $a \sim 0,5$ for most superconductors.

After the discovery of the isotope effect, L.N. Cooper showed that if electrons in a metal experience an attractive interactive force, no matter how small, then electrons would spontaneously pair up, resulting in a material with very different properties [31, 32]. The normal state of such a material is unstable at lower temperatures and a more stable superconducting state with coupled electrons (Cooper pairs) is preferred.

Two electrons with opposite spin and momentum form Cooper pairs. Since the electrons of a Cooper pair have a total spin equal to zero all pairs act as bosons, and occupying the same quantum state, the BCS ground state. Consequently, the condensation of electrons into Cooper pairs can be described by a single macroscopic quantum wavefunction. This implies

that superconducting is an inherently quantum mechanical phenomenon, which manifests itself on a macroscopic scale.

Critical temperature, T_c

A famous result of the BCS theory is the relationship between critical temperature and the lattice environment:

$$k_B T_c = 1.13\hbar\omega_D \exp\left(-\frac{1}{\lambda_{ep}}\right), \tag{1.47}$$

where ω_D is the Debye lattice frequency and λ_{ep} is a dimensionless electron-phonon parameter which typically has values close to 0.3 for conventional superconductors. With $\lambda_{ep} = 0.3$, and typical values for ω_D equal to 10^{12} Hz to 10^{13} Hz[10], an upper limit for the BCS value T_c of approximately 25 K is implied. This conclusion has to some extent been challenged by Nagamatsu *et al*'s [14][15] discovery that MgB_2 has a superconducting transition temperature $T_c = 39$ K.

The BCS limit obviously does not apply to HTSs, which typically have critical transition temperatures greater than 77 K. Nonetheless, the basic BCS model is the foundation of the understanding of all superconductors. Currently, there is no general consensus in the scientific community on the microscopic mechanism operating in HTSs, unlike MgB_2, which is classified as a conventional BCS superconductor. The main discourse focuses on the 'glue' of the coupled holes (the charge carrier in HTSs), which form the superconducting condensate.

Energy gap, 2Δ

The energy gap or order parameter Δ is a fundamental quantity within the BCS theory. It can be shown that the minimum energy required to break up a Cooper pair is 2Δ. The energy gap at $T = 0$ K is related to T_c by,

$$2\Delta_0 = \beta_c k_B T_c. \tag{1.48}$$

For so-called weak-coupled superconductors, experimental values for β_c vary from 3.0 to 4.5 - with most around the theoretical BCS value of $\beta_c = 3.5$. HTS experimental data suggests

[10]This vibration range is equivalent to the Debye temperatures, $\Theta_D = 100$ K - 500 K where $\hbar\omega_D = k_B\Theta_D$.

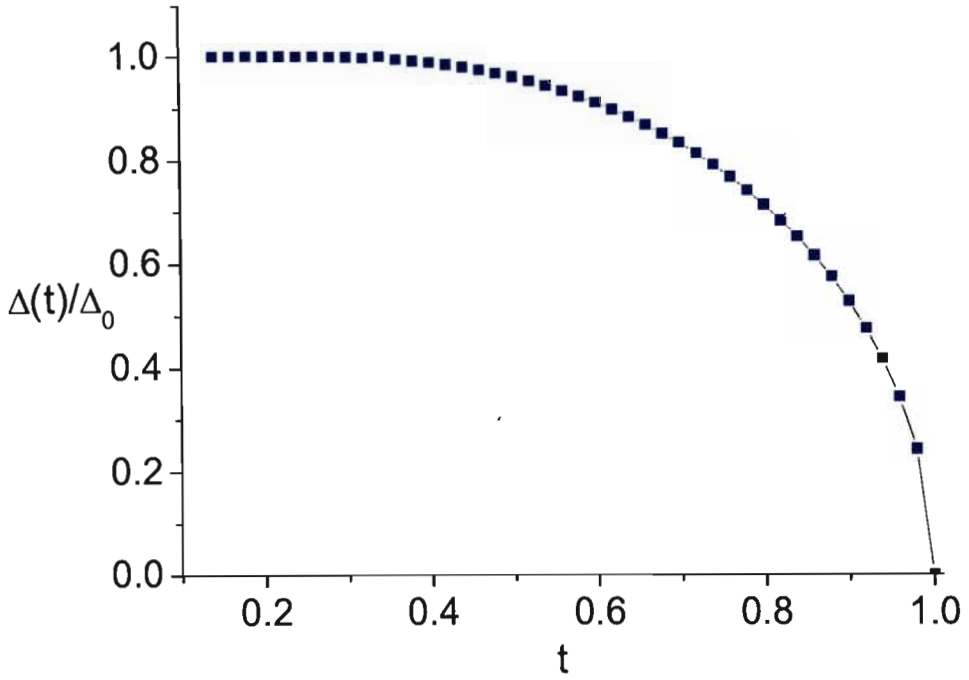

Figure 1-3: Temperature dependence of the BCS energy gap for the range $0.1 \leq t \leq 1.0$.

that the energy gap width lies between 4 and 7 [23, 33]; this suggests that HTS's are not weak-coupled BCS superconductors.

The temperature dependence of the gap is somewhat flat until it nears T_c. Close to T_c, Δ decreases rapidly according to:

$$\frac{\Delta(T)}{\Delta_0} = 1.74\left(1 - \frac{T}{T_c}\right)^{1/2} \qquad T \approx T_c. \tag{1.49}$$

Numerically calculated values of the reduced gap parameter $\frac{\Delta(T)}{\Delta_0}$ versus reduced temperture $t = \frac{T}{T_c}$, are plotted in Figure 1-3 [34].

Coherence length, ξ

Coherence in superconductivity is the mutual interaction and correlation of the behaviour of electrons extending over some distance, where the maximum distance is called the intrinsic BCS

coherence length, ξ_0. According to the BCS theory $\xi_0$is related to the energy gap by,

$$\xi_0 = \frac{\hbar v_F}{\pi \Delta_0}, \tag{1.50}$$

where v_F is the Fermi velocity [35].

Unlike conventional superconductors, which have coherence lengths ranging from 0.1 - 1μm, HTSs have very short coherence lengths of the order of atomic distances, resulting from large Δ_0 and small v_F.

Pippard concluded from microwave surface-impedance measurements that a small amount of impurities does not have a significant effect on T_c but strongly effects ξ [25]. He suggested that the electron mean free path l_e limits the intrinsic range of the Cooper pair, see Equation 1.18.

It is useful to classify superconductors as 'clean' if $l_e \gg \xi_0$ and 'dirty' if $l_e \ll \xi_0$,

$$\begin{aligned} \xi(T) &= 0.74\xi_0 \left(\frac{T_c}{T_c - T}\right)^{1/2}, \quad l_e \gg \xi_0, \quad \text{Clean Limit,} \\ \xi(T) &= 0.85\sqrt{\xi_0 l_e} \left(\frac{T_c}{T_c - T}\right)^{1/2}, \quad l_e \ll \xi_0, \quad \text{Dirty Limit.} \end{aligned} \tag{1.51}$$

Penetration depth, λ

In contrast to ξ, the penetration depth λ increases with increasing concentrations of impurities via the decreasing of the mean free path of electrons [25]. This approach has been confirmed by the BCS theory. The BCS dependence of $\lambda(t)$ on reduced temperature for both the 'dirty' ($n = -\frac{1}{2}$) and 'clean' ($n = -\frac{1}{3}$) limits is the following:

$$\lambda(t) = \lambda_0 \left[\frac{\Delta(t)}{\Delta_0} \tanh\left(\frac{\beta_c}{4t}\frac{\Delta(t)}{\Delta_0}\right)\right]^n, \tag{1.52}$$

where Equation 1.52 is used in fitting magnetisation data in Chapter 5.

1.5 Characteristic Properties of Superconductors

1.5.1 Type-I and type-II superconductors

Other than niobium, vanadium and technetium all elemental superconductors are so-called 'type-I', with HTS and intermetallic superconductors being of 'type-II'. The distinctions between type-I and type-II superconductors initially arose from a study of the behaviour of a superconductor in an applied magnetic field. A quantitative description of the magnetic behaviour, including the classification of type-I and type-II superconductors, was first formulated by Abrikosov [3] in his analysis of the Ginzburg-Landau theory, as discussed in Section 1.3.4.

An important aspect of superconductivity is the Meissner effect, which is a direct consequence of the macroscopic quantum nature of a superconductor. This effect demonstrates the property of a superconductor to be a perfect diamagnetic material and it cannot be explained by infinite conductivity. A fundamental difference between a theoretical perfect conductor and a superconductor is the fact that the former can be considered a magnetic field 'conserver' ($\frac{d\mathbf{B}}{dt} = 0$); while a superconductor is a magnetic field 'expeller' ($\mathbf{B} = 0$), screening out magnetic field from its interior.

For a type-I superconductor with zero demagnetisation factor (a long thin cylinder in a parallel field) the magnetic field is expelled up to a maximum field value, H_c, above which the superconducting state ceases, as shown in Figure 1-4. In the case of a type-II superconductor there are two critical fields. The same perfect diamagnetic response is observed up to a lower critical field $H < H_{c1}$. Above H_{c1}, superconductivity is not destroyed; instead magnetic field penetrates into the bulk of the superconductor, forming normal regions in the form of magnetic vortex filaments. This 'mixed state' may or may not be able to exhibit perfect conductivity, depending on whether the vortices are locked (or pinned) by pinning sites. Each vortex contains exactly one magnetic flux quantum of magnitude:

$$\Phi_0 = \frac{hc}{2e} \tag{1.53}$$

where, h is Planck's constant, c the speed of light in a vacuum and e is the charge of an electron. The denominator $2e$ in Equation 1.53 is a consequence of the fact that the charge carriers of a superconductor are Cooper pairs. A rough picture of a vortex consists of a normal core and

a circulating supercurrent. The core, with radius $\sim \xi$, consists of the magnetic field which has 'punctured' though the superconducting material and the vortex supercurrent circulates within a region of radius $\sim \lambda$ around the core.

When flux first enters a type-II superconductor the interaction of the vortices is small because they are far apart. With increasing magnetic field the separation between vortices is comparable to the penetration length, vortices repel each other and form a regular triangular vortex lattice. Pinning of the vortices due to inhomogeneities in the superconducting material leads to a semi-glass magnetic structure in some regions. As discussed in Section 1.3.4, the formation of the normal regions in a type-II superconductor is an energy consequence, which 'allows' the superconducting state to persist above H_{c1}, up to an upper critical field H_{c2}, above which the normal state is preferred, as shown in Figure 1-4 (b) and (c) respectively[11].

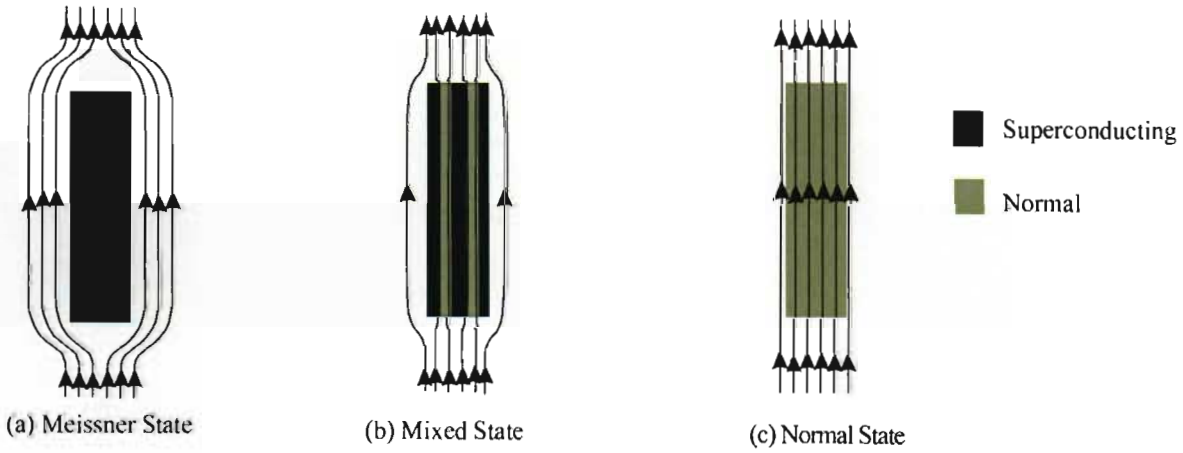

Figure 1-4: Field profiles for a superconductor in (a) Meissner state type-I ($H<H_c$) or type-II ($H<H_{c1}$), (b) mixed state type-II ($H_{c1}<H<H_{c2}$), (c) normal state for either type-I ($H>H_c$) or type-II ($H>H_{c2}$) or $T>T_c$.

The magnetic flux density B and the applied magnetic field H_a are related to each other by the following expression,

$$B = H_a + 4\pi M, \tag{1.54}$$

[11]The existence of a third critical field, H_{c3}, refers to the end of superconductivity at the surface of a superconductor. 'Surface superconductivity' can exist at fields greater than H_{c2} when the surface is parallel to the external field.

where M is the magnetic moment per unit volume. The magnetisation curve is often plotted as -$4\pi M$ versus H_a. Magnetisation curves for reversible (zero flux pinning) type-I and type-II superconductors are shown in Figure 1-5. The area under a magnetisation curve is a direct measure of the condensation energy associated with the superconducting state.

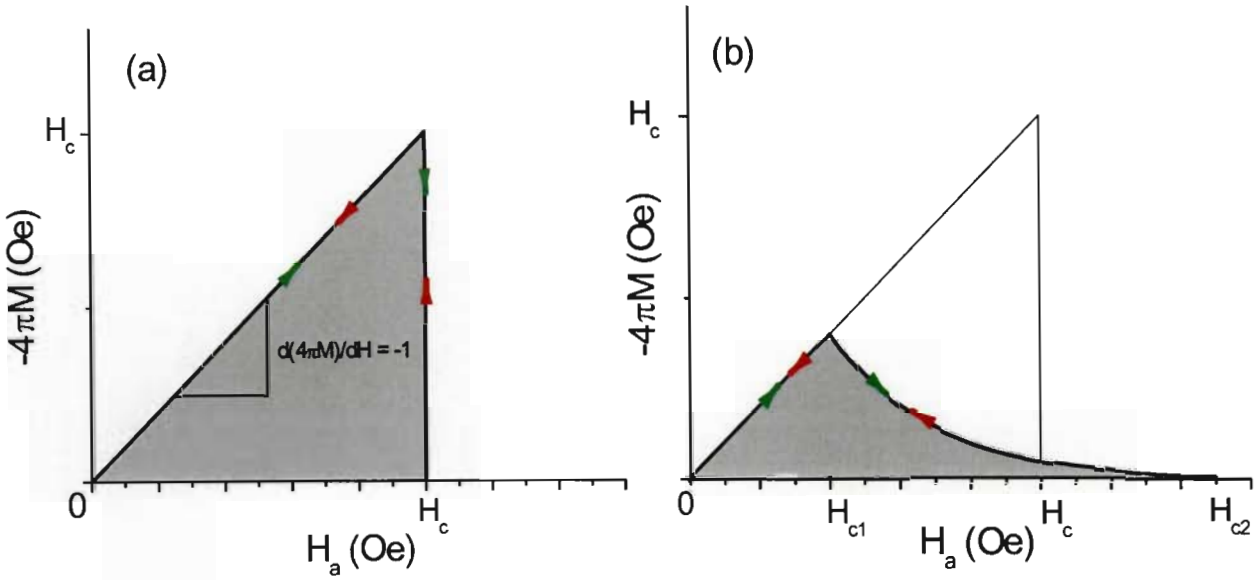

Figure 1-5: Ideal reversible magnetisation curves for (a) type-I and (b) type-II superconductors.

The reversible response of a type-II superconductor to an applied magnetic field, shown in Figure 1-5 (b), is an ideal case. In practise, with the applied field increasing or decreasing in the mixed state, vortex motion is inhibited by pinning centres, such as material defects. This results in a non-reversible $M(H)$ relationship such as that illustrated by the black curve in Figure 1-6, the red curve is a theoretical reversible plot.

Perfect conductivity in the mixed state cannot be assumed - the interaction of current and vortices (self-field or external field) results in a Lorentz-like force on the vortices, which tends to move them against pinning forces, resulting in power dissipation. Pinning of vortices enables type-II superconductors to carry currents with zero resistance. Table 1.2 provides upper critical field parameters for selected compounds and alloys at practical operating temperatures of liquid nitrogen (77 K) or helium (4.2 K).

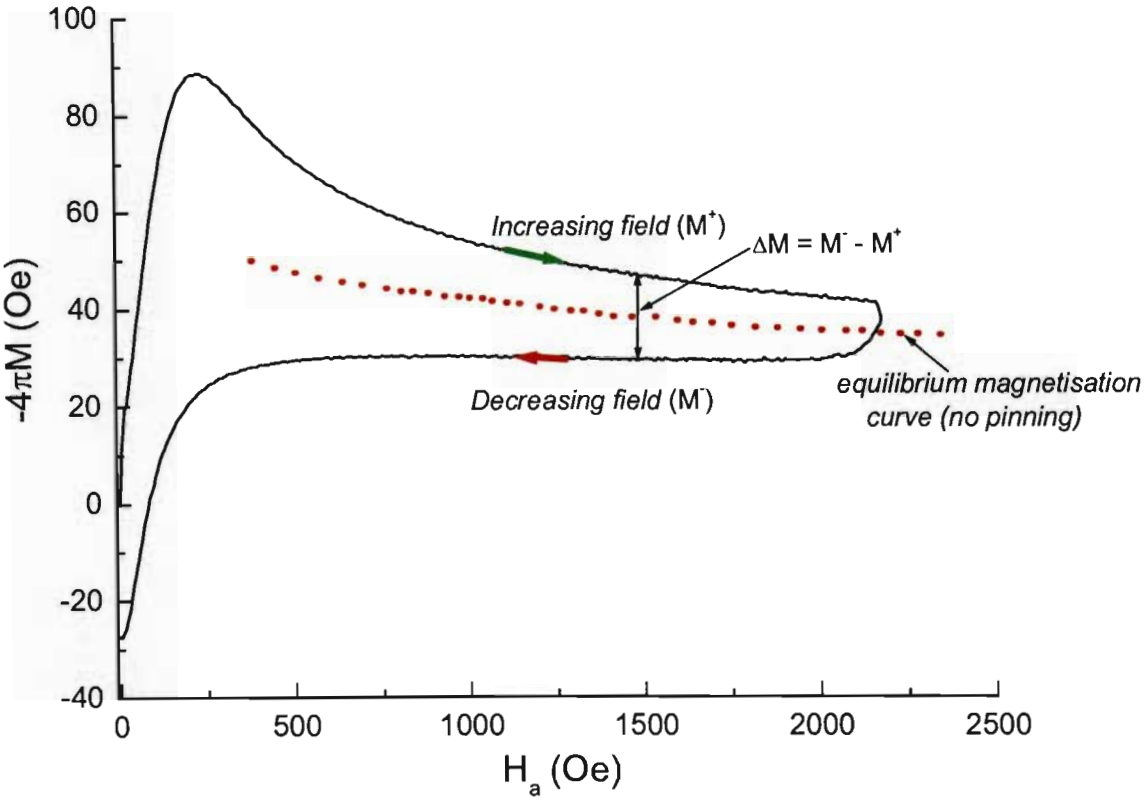

Figure 1-6: Hysteresis magnetisation curve due to pinning of vortices.

Table 1.2: Upper critical magnetic field values given in SI units of Tesla for selected superconductors.

Material	B_{c2} (T)
Nb_3Sn	22 (4.2 K)
$Nb_3(Al_{75}Ge_{25})$	40 (4.2 K)
$(Bi,Pb)_2Sr_2Ca_2Cu_3O_x$	3 (30 K) 1 (77 K)
YBa_2CuO_{7-x}	10 (77 K)

For the scope of this thesis it is necessary to assume that the magnetisation response to applied field, $M(H)$, is comprised of two components, equilibrium M_{eq} and irreversible M_{irr}:

$$M = M_{eq} + M_{irr}. \tag{1.55}$$

M_{eq}, which is negative in sign, is the equilibrium magnetisation that is generated by the supercurrents associated with individual vortices. M_{irr} is the magnetic response due to macroscopic supercurrent J_c whose existence, as discussed above, depends on the pinning of vortices; that is, $J_c = 0$ when $M_{irr} = 0$ (zero pinning force). If pinning forces are 'small' then $M(H)$ curves are almost reversible. Under this condition of reversibility, the London penetration depth can be related to M_{eq}. This will be discussed further in Section 3.5.

Finally, unlike the above case of no pinning (reversible $M(H)$ relationship), C.P. Bean developed a critical state model (CSM) to describe the $M(H)$ properties in a type-II superconductor when there is significant pinning [36]. The CSM is used in the estimation of the critical current by analysing the $M(H)$ relationship. The model predicts that $J_c(H,T)$ is proportional to $\Delta M = M^- - M^+$, where $M^-(M^+)$ is the magnetisation measured in decreasing (increasing) field respectively, as shown in Figure 1-6.

1.5.2 The Critical State Model

Bean's critical state model (CSM) [36], is based on the fact that the resistance of a superconductor is zero, which implies there are two states for current flow, either the current density is equal to J_c or zero. Figure1-7 illustrates the model for an initially unmagnetised slab of type-II superconductor, in increasing magnetic field (a) $\rightarrow$ (b) and decreasing field (b) $\rightarrow$ (c). When the external applied field parallel to the conductor surface is raised by H_c, a bipolar current of $\pm J_c$ is induced. The external applied field penetrates to such a depth that the shielding field cancels the external applied field in the central region. While increasing the external field, both the current and the field penetrate deeper into the superconductor until the centre is reached by the penetrating external field H_p and is directly related to the current that the superconductor can sustain without vortex lattice motion. The interaction between the vortex lattice and pinning sites is important as it permits the superconductor to sustain a supercurrent without dissipation. If the vortex lattice moves, this implies a local change in flux has occurred and

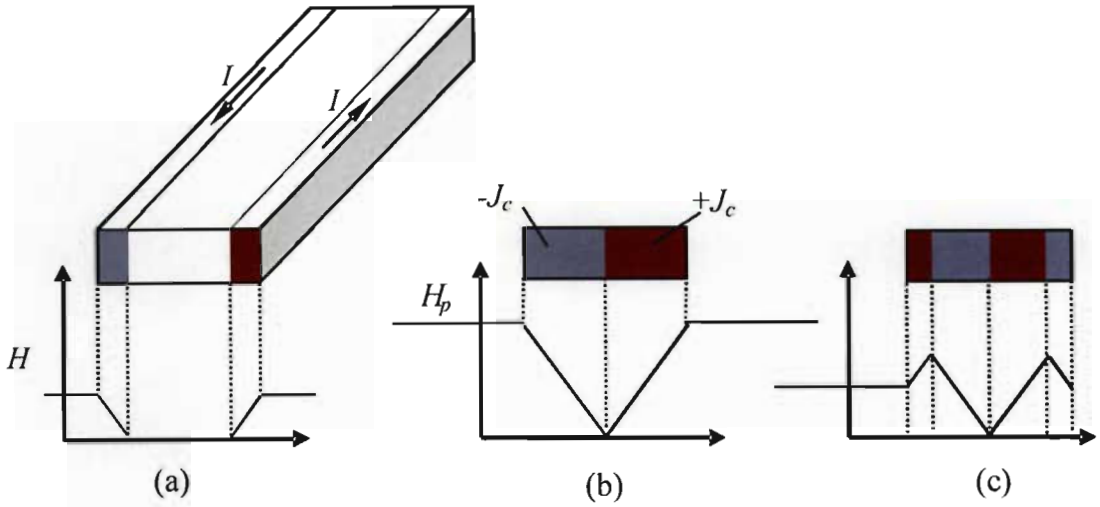

Figure 1-7: Internal field profile in a slab of type-II superconductor according to the Bean critical state model [36], with external field parallel to the surface (increasing magnetic field (a) → (b) and decreasing field (b) → (c)).

an electric field is induced. The interaction of the electric field and current results in energy dissipation.

The Bean CSM assumes that J_c is independent of B and the following general expression represents the CSM where the magnetic field gradient is equal to the critical current density and proportional to the vortex pinning force,

$$\nabla \times \boldsymbol{H} = \frac{4\pi}{c}\boldsymbol{J}. \tag{1.56}$$

Reducing the external field below H_p results in a new induced bipolar current of opposite polarity with a more complex magnetic profile sketched in Figure 1-7(c). In Chapter 3 a polycrystalline HTS intergranular CSM (based on the above general form) is developed, which has morphology-dependent parameters.

1.5.3 The DC Josephson effect

Giaever's [10] observation of single electron tunnelling led to the discovery of the Josephson effects, one of which is to be discussed in this section. In 1962 Brian Josephson [37-39] successfully predicted the tunnelling of Cooper pairs though an S_aIS_b (superconductor insulator

superconductor) junction, providing the insulator was thin enough ($\sim$ 10 Å), with no potential drop across the insulator. This tunnelling effect is known as the 'DC Josephson effect' and not only takes place in junctions but also in other 'weak-links' where the critical current is suppressed, for example in HTS intergranular material.

The DC Josephson effect is based on the quantum nature of superconductivity. In order to understand the effect consider two identical and separate superconductors where each superconductor will have its ensemble of Cooper pairs in one single state, described by a wavefunction, $\Psi_i = |\Psi_i| e^{\varphi_{pi}}$. At the same temperatures their respective amplitudes will be identical, but their phase will be arbitrary. If the two superconductors are brought together, in such a way as to establish a perturbation resulting in a weak link, the interference between their wavefunctions results in a new wavefunction for the whole. The amplitudes of the wavefunctions are equal before the joining but their phases are not, hence the phase coherence is directly related to the establishing of a weak-link contact.

In Josephson junctions the wavefunctions on either side of the barrier/insulator become locked together with a phase difference, $\gamma_{\varphi_p} = \varphi_a - \varphi_b$, and a supercurrent, I_{cj}, flows between the two superconductors with zero voltage drop, according to the following expression,

$$I_{cj} = I_{c0j} \sin \gamma_{\varphi}. \tag{1.57}$$

The above equation implies that if a tunneling current I_{cj} is to flow across the junction, the phase difference γ_{φ} adjusts accordingly. If an injected current is higher than the maximum critical tunnel current, $I_{c0j} = I_{cj}(0)$, then a voltage difference V_d develops across the junction.

Derivation of the DC Josephson effect

The above Josephson relation, Equation 1.57, can be derived directly from GL equations, discussed in Section 1.3.4.

The insulator barrier of a SIS junction is perpendicular to the x-direction with a current in this direction given by the second GL-equation, Equation 1.29. If the barrier were infinitely

thick, the junction current would be zero and Equation 1.29 would be,

$$-i\hbar\frac{\partial\Psi}{\partial x} - e^*\mathbf{A}_x\Psi = 0.$$

If the barrier is 'thin' the current on the one side of the junction must be related to the order parameter on the other side of the junction. Phenomenologically, this boundary condition can be represented by the following expression,

$$\left(-i\hbar\frac{\partial}{\partial x} - e^*\mathbf{A}_x\right)\Psi[\text{side a}] = -i\hbar\frac{\Psi}{b}[\text{side b}], \tag{1.58}$$

were the parameter b has the dimensions of length. The current flowing in side 1 is

$$J_x = \frac{e}{m_e}\left[\Psi_{\rm a}^*\left(-i\hbar\frac{\partial}{\partial x} - e^*\mathbf{A}_x\right)\right]\Psi_{\rm a}.$$

Using Equation 1.58 we can write the above equation as

$$\begin{aligned} J_x &= -\frac{i\hbar e}{bm_e}\left[\Psi_{\rm a}^*\Psi_{\rm b} - \Psi_{\rm b}^*\Psi_{\rm a}\right] \\ &= \frac{2e\hbar}{m_e b}|\Psi_{\rm a}||\Psi_{\rm b}|\sin(\varphi_{\rm b} - \varphi_{\rm a}), \end{aligned} \tag{1.59}$$

which is the Josephson relation, Equation 1.57.

Temperature dependence

Ambegaokar and Baratoff [40] applied the BCS theory to an ideal planar SIS junction and calculated the temperature dependence of I_{c0j}, to be given by:

$$I_{c0j}(T) = I_{c0}F(T) = I_{c0}\left[\frac{\Delta(T)}{\Delta_0}\tanh\left(\frac{\Delta(T)}{2k_BT}\right)\right] \tag{1.60}$$

where $I_{c0} = I_{c0j}(T=0) = \dfrac{\pi\Delta_0}{2eR_n}$, R_n is the normal-state junction resistance, $\Delta(T)$ is the gap parameter, $\Delta_0 = \Delta(T=0)$, e is the charge of an electron and k_B is Boltzmann's constant.

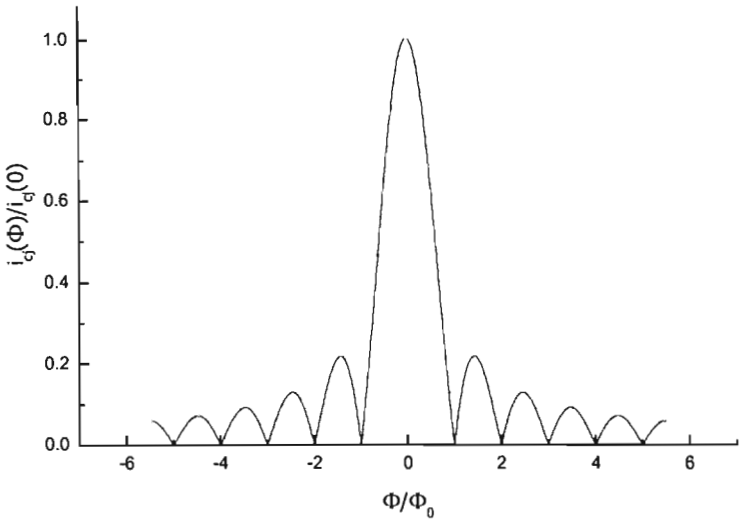

Figure 1-8: Magnetic field dependence of the Josephson current for a rectangular uniform junction.

Field dependence

One of the most remarkable aspects of Josephson junctions is the existence of an 'interference pattern' where the modulation is a direct consequence of the wavelike nature of Cooper pairs. If we assume a 'rectangular' Josephson junction a 'Fraunhofer diffraction' [41, 128] relationship exists between the maximum supercurrent and magnetic field (see Figure 1-8), which is described by the expression

$$I_{cj} \propto G(H,T) = \left| \frac{\sin(\pi\Phi/\Phi_0)}{\pi\Phi/\Phi_0} \right|, \tag{1.61}$$

where $\Phi = \Phi(H,T)$ is the total flux threading the junction.

Finally, the temperature and field dependent equation for the Josephson current in a single ideal SIS junction can be expressed as,

$$I_{cj}(H,T) = I_{c0j}(T)G(H,T). \tag{1.62}$$

This concludes a general discussion on theories and characteristic properties relating to superconductivity. It forms the foundation for the following two chapters, which relate specifically to high temperature superconductivity.

Chapter 2

High-Temperature Superconductivity

After a brief discussion on the discovery of high-temperature superconductors (HTSs), this chapter focuses on structural issues relating to HTS - starting from the general crystalline form, with its unique superconducting copper oxide planes and anisotropic complications, to structural intergranular problems that manifest as 'weak-links' between grains. [Weak-links are characterised by a short section of superconductor or barrier material, of the same order as the coherence length, where the order parameter (and critical current) is substantially suppressed.] Against this backdrop the future of HTS technology is discussed.

2.1 Discovery

In 1986, J. Bednorz and K. A. Müller [4] surprised the solid state physics and material science communities with their discovery of a polycrystalline ceramic superconducting system La-Ba-Cu-O, with a $T_c > 30$ K. The maximum critical transition temperature had been fixed at 23 K for over a decade and the BCS theory presented convincing arguments that T_c above 30 K was probably impossible (presently, there is no accepted theoretical explanation of high temperature superconductivity). The evolution of transitional critical temperatures in superconductors is shown in Figure 2-1.

Initially the research of Sleight *et al* [42] and K. H. Höck *et al* [43] caught the attention

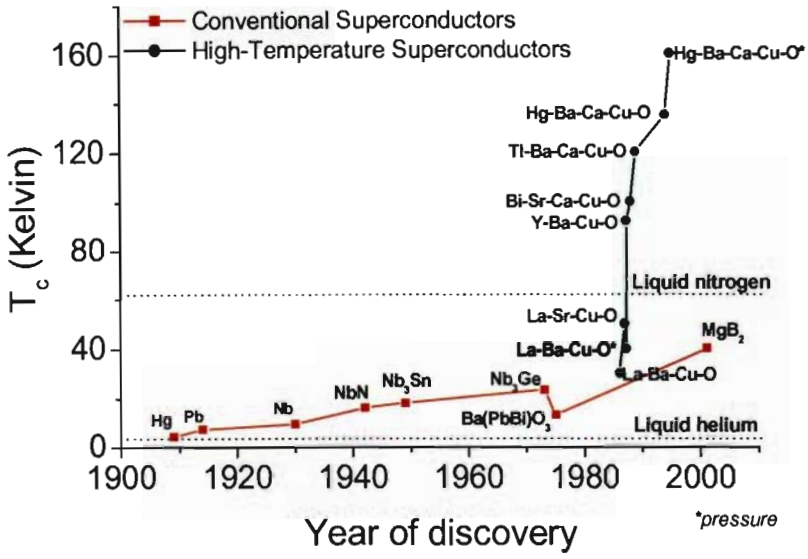

Figure 2-1: Critical temperature vs year of discovery for a few important superconductors.

of Bednorz and Müller[1]. Sleight *et al* had found that the perovskite Ba $(Pb_{1-x}Bi_x)O_3$ superconducts at 13 K and Höck *et al* had suggested that the Jahn-Teller effect[2] may lead to polaron-induced high-temperature superconductivity in transition-metal oxides [44]. This was the beginning of the discovery of HTSs. It is remarkable how HTSs differ from conventional metallic superconductors; none of the constituent atoms of HTSs are superconductors and no evidence from conventional superconductivity research had suggested focusing on oxides, which are predominantly classified as insulators at room temperature.

The sharp drop in resistance in the La-Ba-Cu-O system, suggesting the presence of a superconducting phase, was confirmed by many sources, one of which was C. W. Chu. Chu *et al* [45, 46] placed a specimen of La-Ba-Cu-O under hydrostatic pressure and recorded an increase in T_c to 50 K. Instead of applying an external pressure, controlled atomic substitution achieved the same effect with an increase in T_c. For example, Bednorz, Müller and Takashige [47] partially replaced La by Sr or Ca rather than Ba ; they found with La substituted by Sr, T_c was raised

[1] On 8^{th} December 1987 they were awarded the Nobel Prize in Physics for the discovery of high-temperature superconductivity.

[2] see C. Kittel and H. Kroemer, *Thermal Physics*, 2nd ed., Freeman, 409, (1980)

to 40 K at ambient pressure.

In 1987, following the same reasoning as Bednorz *et al* in substituting atoms to increase internal pressure in the crystal lattice, Wu *et al* [13, 48] discovered superconductivity in $YBa_2Cu_3O_{7-x}$ (YBCO)[3], which had a $T_c \approx 92$ K. A typical resistance versus temperature curve for YBCO is shown in Figure 2-2. YBCO's critical temperature is well above that of the boiling point of liquid nitrogen (77 K), a much cheaper cryogen than liquid helium.

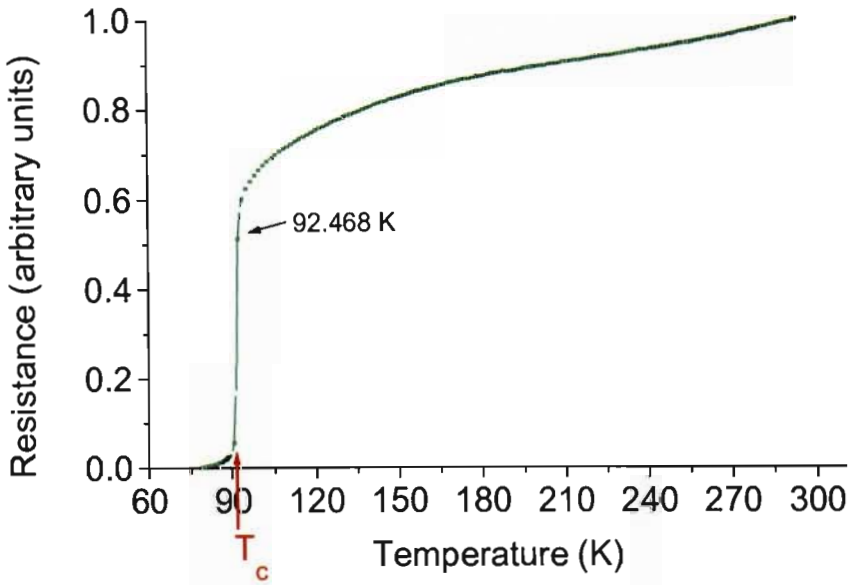

Figure 2-2: Temperature versus resistance of a HTS , showing the phase change of $YBa_2Cu_3O_{7-x}$ below 93 K (present work).

Since the discovery of YBCO, a large number of HTS compounds have been discovered; to date $HgBa_2Ca_2Cu_3O_8$ has the highest T_c, equal to 135 K (160 K under pressure) [5].

Presently, there is no theoretical explanation for the superconducting state in HTS material. Despite this, they exhibit superconducting properties that can be described by phenomenological theories such as the Ginzburg-Landau theory discussed in Chapter 1. One of the main

[3]This was the discovery of the '123' superconductors where Y can be replaced by many other rare earth elements resulting in slight changes in T_c.

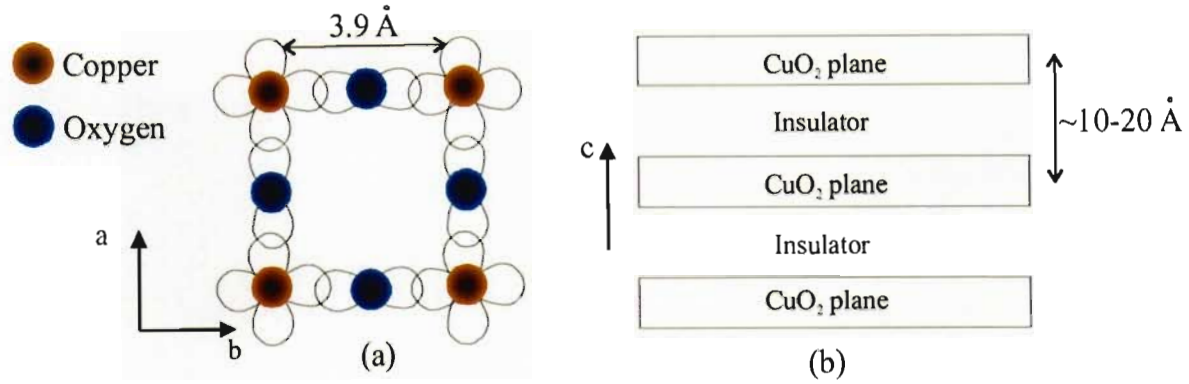

Figure 2-3: Copper oxide superconducting structure. (a) Unit cell of Cu_2O, ab-plane. (b) Layered superconducting planes, c-axis.

differences between conventional and HTSs is the short coherence length with respect to material defects associated with HTS; for example, twinning, dislocation, grain-boundaries, etc. The short coherence length is the source of the weak-link grain boundary problem, i.e. a grain boundary can decrease the intergranular critical current flowing from one grain to another by orders of magnitude. Another important property associated with HTSs is their anisotropic nature, which results from a layered crystal structure. [The short coherence length and anisotropic nature gives rise to difficult and complex fabrication techniques in the production of electronic superconducting components and superconducting cable [49, 50].]

2.2 Crystalline structure - the general form

Crystallographic investigation in order to identify superconducting phases and their crystalline structure has been central in HTS research [51]. From this research it has been established that all HTS crystalline structures are generically the same material, consisting of conducting CuO_2 planes, separated by insulating layers as shown in Figure 2-3 [52].

When optimally doped[4] with charge carriers (holes) the CuO_2 planes can conduct and superconduct along the alternating Cu and O within the planes[5]. Apart from the existence

[4] Normally in an oxygen atmosphere.
[5] Where the Cu $3d$ orbitals and the O $2p$ orbitals line up in energy.

of supercurrent in the superconducting planes, tunnelling supercurrents exist between multiple parallel conducting layers that are approximately 1 nm apart, thus resulting in the HTS being entirely superconducting but highly anisotropic. The insulating layers act as charge reservoirs, which maintain proper doping in the CuO_2 and serve as spacers that couple the parallel CuO_2 planes.

In this study the HTS of choice is YBCO, with a $T_c \approx 92$ K. An obvious reason for the preferential study of YBCO is that its T_c is above the boiling point of liquid nitrogen (77 K), which was the cryogen available for this research. Secondly, YBCO has superior magnetic and current properties when compared to most other HTSs at operational temperatures greater than 60 K; reversible $M(H)$ behaviour is only apparent at temperatures close to T_c. Thus, YBCO is the material of choice in many practical HTS applications, particular in second-generation wire (to be discussed in Section 2.5.1).

2.2.1 $YBa_2Cu_3O_{7-x}$

The YBCO crystal structure is similar to the cubic perovskite structure. This structure type is more commonly associated with piezoelectric and ferroelectric materials. In fact, the structure of YBCO comprises a stack of three perovskite-like cubes as shown in Figure 2-4.

The total number of oxygen (O) sites available per triple perovskite structure of YBCO is nine and not seven, which one may assume at a first glance at its chemical formula, $YBa_2Cu_3O_{7-x}$. The location and content of O atoms within the YBCO crystal structure is critical to the superconducting state [53].

The YBCO unit cell in Figure 2-4 shows that the O-atoms, above and below the yttrium (Y) atom (level), form part of complete CuO_2 planes, but are missing at the Y-level. Also, on the top and bottom of the unit cell, the O-atoms in the front and back are missing, leaving straight Cu-O chains, i.e. no complete planes. This results in a set of two closely coupled superconducting CuO_2 planes per YBCO unit cell.

The valences of the atoms in the unit cell of $YBa_2Cu_3O_6$ are most important and suggest a low hole density concentration: since Y is +3, Ba is +2, Cu is +2 and O is -2, this gives a total of 3+4+6-12=+1. [Assuming all the holes are mobile this results in 6 x 10^{27} holes/m^3, a lower charge carrier concentration than in conventional metals.] For a maximum T_c oxygen

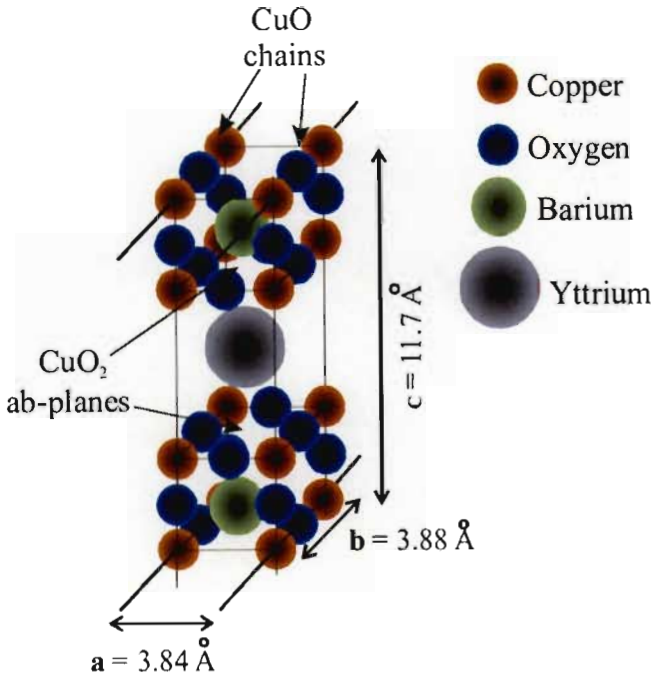

Figure 2-4: Unit cell of YBCO, with CuO_2[ab]-planes and CuO chains.

diffuses into the O sites of Cu-O chains, implying an even lower charge carrier concentration. $YBa_2Cu_3O_{6+x}$ is an insulator in the range $0.0 < x < 0.4$ and superconducts in the range $0.4 < x < 1.0$ as shown in Figure 2-5.This dependence of the state of YBCO on oxygen content is extremely important. Consequently, annealling in an oxygen atmosphere is an essential step in the production of superconducting YBCO.

2.2.2 Anisotropy

High temperature superconductors (HTSs) are described as anisotropic superconductors with superconductivity mainly confined to two-dimensional CuO_2 ab-planes. It is because of the CuO_2 ab-planes that anisotropy dominates the normal and superconducting properties of HTSs. A single YBCO crystal, for example, has larger critical currents in the ab-plane than along the c-axis, and the penetration depth and coherence length are also anisotropic in nature [23, 54]. The degree of anisotropy varies from HTS to HTS; for example, the normal resistance ratio of the 'BSCCO' (mixed oxides of bismuth, strontium, calcium and copper) system may be as high

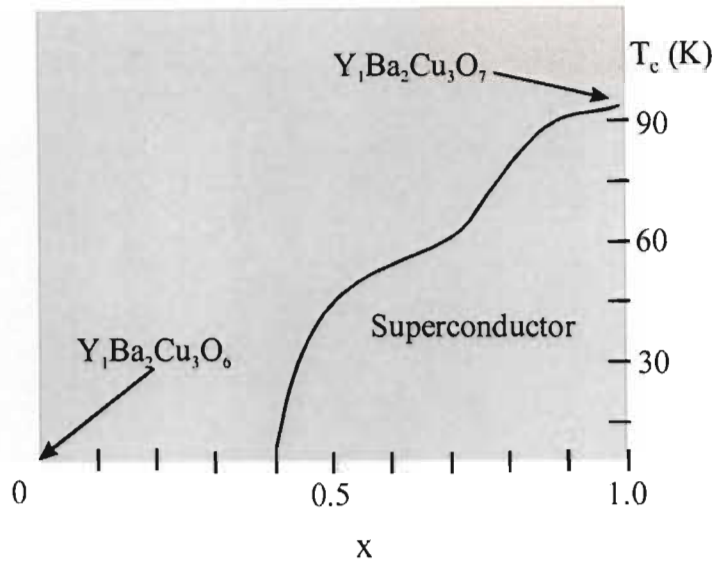

Figure 2-5: Variation of critical temperature as a function of oxygen doping in $YBa_2Cu_3O_{6+x}$.

10^5, while in YBCO it is 10^2. Another important form of anisotropy is that found in the energy gap in the ab-plane. The energy gap of a HTS has a predominant $d_{x^2-y^2}$ symmetry, with the possible exception of $Nd_{1-x}Ce_xCuO_4$ [55-60]. This implies that the gap is greatest along the a and b directions and zero between the two axes, and has direct implications for the critical current in grain-boundaries [61].

Anisotropy must be considered when analysing magnetic data, including that for polycrystalline granular material. This study introduces an average granular penetration depth, $\overline{\lambda_g}$, which is an average penetration depth in the ab-plane, λ_{ab} and the penetration depth in the c-direction, λ_c. A detailed study is presented in Chapter 3; where $\overline{\lambda_g}(T)$ data is derived from high-field magnetisation M versus applied field H isotherm curves.

2.3 Polycrystalline material

Bulk polycrystalline HTSs have transport current characteristics that differ significantly from those of conventional superconductors [62, 63]. This is due to weak superconducting coupling between grains, which behave as magnetically sensitive Josephson junctions - grain boundary Josephson junctions (GBJs) [64-66]. This is the so-called 'weak-link' effect [67], which is central

to this thesis. It is the 'weak-link' effect that determines the ultimate transport current in a HTS and this is a severe problem in large current applications, for example in HTS tape/wire the intergranular critical current may be orders of magnitude less than intragranular critical currents[6] [66].

No single physical parameter can be used to described a grain boundary as a GBJ. Parameters can be categorised as either intrinsic or extrinsic, for example the short coherence length of HTSs is considered intrinsic compared to trapped secondary phase in the GBs.

The grain boundary (GB) density in HTS material is a consequence of the preparation methods used. For example, a solid state prepared polycrystalline bulk HTS will have on average a smaller grain than that of a melt textured processed material, and hence a higher GB density. In this study, polycrystalline YBCO material was chosen in order to investigate GB weak-link effects. Figure 2-6 shows a micrograph of grains of a polycrystalline YBCO specimen.

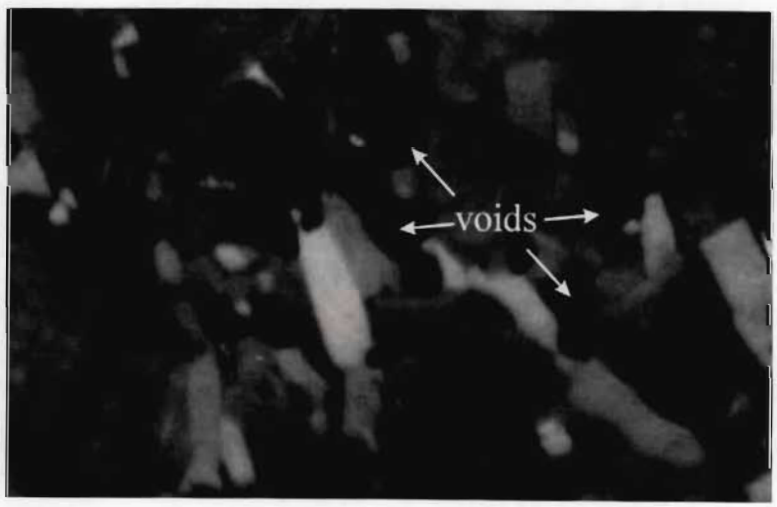

Figure 2-6: Polycrystalline YBCO showing typical granular structure and voids (dark regions).

A number of papers have correlated structural parameters of GBs with their ability to carry superconducting current [16, 63, 68, 70-74]; for example, grain misorientation angles and dislocation density. A GB is an interface of adjacent grains of different orientation, which have been rotated, i.e. tilted or twisted, with respect to one another, and is therefore a planar defect.

[6] In some electronic applications quite the opposite holds, where the 'weak-link' effect is considered useful.

Figure 2-7 (a) shows an idealised sketch of a contaminated low angle GB.

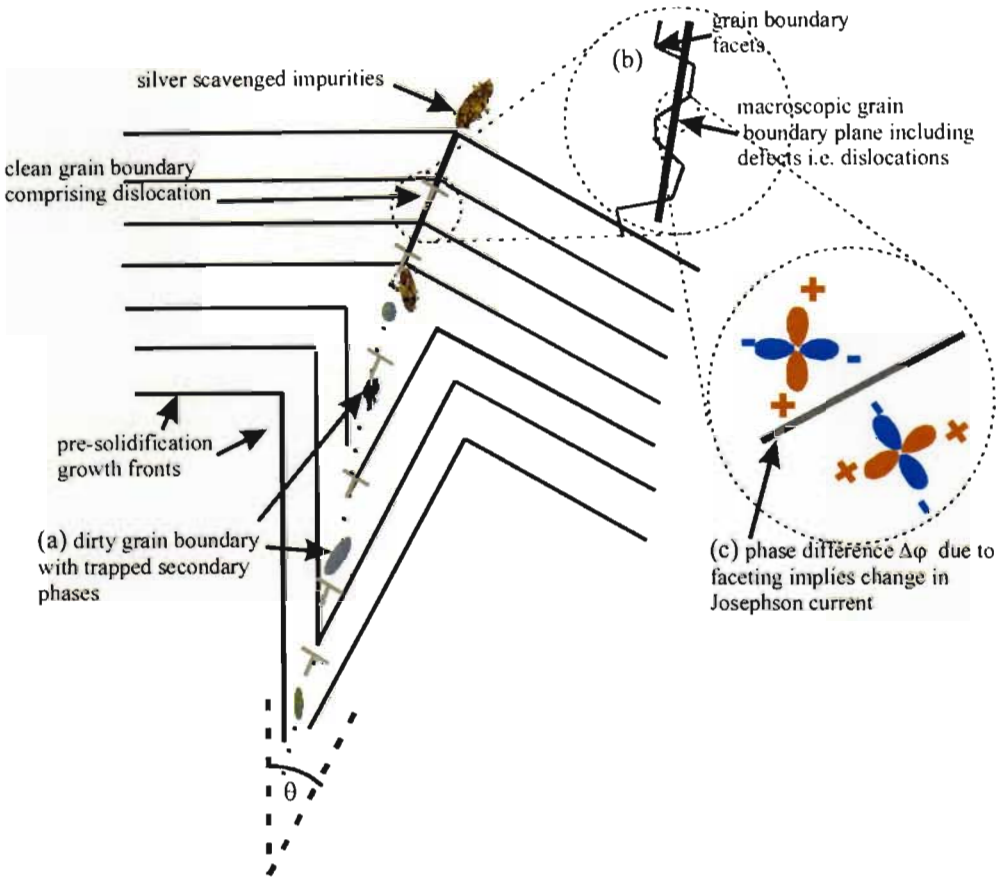

Figure 2-7: Schematic representation of a grain boundary microstructure including dislocations (a) contaminated low angle (θ) grain boundary (b) silver cleaned grain boundary (a result of this study) and (c) phase change of $d_{x^2-y^2}$ order parameter. Facets affect the phase difference which may equal π, resulting in Josephson current flowing backward across the junction.

It has been shown that the misorientation angle between two HTS grains determines the electronic behaviour of the GB [16, 63, 75]. In these studies, single GBs with varying misorientation angles (twist) were fabricated by epitaxially growing YBCO thin films on bicrystal substrates with predefined misorientation angles. A decrease in critical current density J_c of more than three orders of magnitude for increasing misorientation angle θ in the range from 0^0 to 45^0 has been observed [63]. For example, bulk polycrystalline YBCO typically has a critical current density $J_c(T = 77\ \text{K}) < 500\ \text{A/cm}^2$, whereas orientated YBCO thin film grown epitaxially on single crystal oxide substrates, such as $SrTiO_3$ (001) has $J_c(77\ \text{K}) > 1\ \text{x}10^6\ \text{A/cm}^2$

[76]. A sharp decrease of intergranular critical current density is typically observed at angles, $\theta > 10^0$ [16, 17, 75-79].

It has been proposed that the increase in stress fields due to dislocations in GBs suppresses the order parameter and hence contributes to the weak-link behaviour [63, 70]. Meilikhov [81] has published calculations that support the angular dependence of intergranular critical current on dislocations.

Local oxygen stoichiometry within GBs influences grain connectivity [70]. Experimental data suggests that oxygen content and misorientation of grains affects local critical temperature and current density within the GB; this oxygen versus T_c relationship was discussed in Section 2.2.1. From a broader stoichiometry perspective, impurities found in bulk YBCO, such as Y_2BaCuO_5, $BaCuO_2$, CuO, etc, prefer to segregate within GBs and result in the deterioration of grain coupling [82, 83]. One of the main aspects of this thesis is illustrated in Figure 2-7, that of the role of silver doping, where the addition of controlled amounts of silver rids GBs of impurities.

The intragranular critical current density can be up to orders of magnitude greater than the intergranular critical current density in polycrystalline HTSs. This is fundamentally associated with HTSs' intrinsically short coherence length, which results in an undesirable interaction with structural defects such as GBs and impurities, as discussed above.

It has been shown that the nature of the order parameter's symmetry, $d_{x^2-y^2}$, [84-89] coupled with faceting in GBs, as shown in Figure 2-7 (b) and (c), leads to an inhomogeneous current distribution (in the GBJs). Based on this work, a model was developed which successfully described the grain-to-grain angular dependence of the intergranular critical current [90], and indicates that the intergranular critical current is reduced by approximately one order of magnitude, leaving other effects responsible for the further decrease in the critical current.

It is quite clear from the preceding discussion that there is a hierarchy of structural heterogeneities that exists in HTS material, leading to weakly coupled grains. Grain boundaries made up of a dislocation network, as well as macroscopic cracks, voids and secondary inclusions [92, 93], and the consequences relating to the order parameter symmetry and GB facets, all affect the coupling of grains in HTSs on various spatial scales, from tens of micrometers to below nanometres, as illustrated in Figure 2-7.

Other identified problems relating to the intrinsic nature of HTS material are the existence of a space charge layer and significant electronic band bending at interfaces such as GBs, which is related to a combination of low carrier density and a large dielectric constant typical of HTSs [91].

Understanding why grain-boundaries act as Josephson junctions is important in order to improve grain-to-grain coupling in HTS wires/tape. Texturing is a method used to align grains and increase the critical current density, J_c [94, 95]. The material predominately used in the powder in tube (PIT) method is $(Bi,Pb)_2Sr_2Ca_2Cu_3O_x$ (Bi-2223). Bi-2223 is extremely anisotropic and micaceous, enabling it to mechanically texture easily (unlike YBCO). Ultimately, even in superior textured material, only some 10% of the cross section of the material is carrying current [96]. Current in wire/tape or polycrystalline material flows though a weak-link network (of GBs) by a percolation process and it is the percolation paths comprised of low-energy GBs that account for 10% of the cross-sectional area that carries the current. Hence, in order to increase J_c, more paths of low-energy GBs are needed. [The abovementioned are also of concern in the so-called second generation YBCO superconductor tapes, which will be discussed in the Section 2.5.]

In addition to texturing, there are other possible solutions to improving connectivity of grains. For example, (i) fluxing of GBs to obtain cleaner GBs or (ii) doping of GBs to relieve stress at dislocations and/or alter the band structure and charge carrier density at interfaces.

2.3.1 Intergranular structural fluctuations

The nature of the structure of GBJs is important to this study. GBJs are not the ideal planar Josephson junctions discussed in Section 1.4.3.

The relationship between the maximum supercurrent and applied magnetic field, such as the 'Fraunhofer diffraction' pattern shown in Figure 1-8, provides insight into the barrier's (I) structure [97, 98]. Yason [99] studied SIS junctions, in particular Sn-oxide-Sn junctions, with random non-uniformities of the oxide barrier (structural fluctuations). He established that thermal fluctuations destroyed superconductivity, whereas structural fluctuations led to the establishment of a unique levelling off (a plateau region) instead of the typical decaying relation of the 'Fraunhofer diffraction' pattern. This plateau region is a current component

which is field independent.

Josephson effects are not only observed in SIS/SNS junctions, but also intrinsically in 'weak-link' junctions in bulk HTSs. It is 'weak-links' with Josephson junction properties that influence the nature of the supercurrent in bulk HTSs. The existence of a field-independent component of the Josephson current offered a completely different interpretation of bulk HTSs' transport critical current in an increasing magnetic field [100] and will be further discussed in Chapter 3.

A result of this study is the effect of doping on the structure of GBJs. It is through the field-independent critical current component that a measure can be made of the influence doping has on the barrier's structure, i.e. uniform to irregular in nature.

2.4 Further Comments on High-Temperature Superconductors

As previously mentioned, while there is presently no specific theoretical explanation of the mechanism responsible for superconductivity in HTSs, Ginzburg-Landau theory still applies with a few fundamental considerations. For example, in the region where it is applicable, that is near T_c, the free energy difference between the normal and superconducting state becomes comparable to the average thermal energy. HTSs are more intrinsically sensitive to thermal fluctuations due to their large penetration depth, small coherence length and higher operating temperatures. Consequently, thermal fluctuations (k_BT) must be taken into account. Due to the small concentration of charge carriers the penetration depth for high temperature superconductors is much larger than that for conventional superconductors.

Another consideration is the anisotropic nature of high temperature superconductors. For materials such as BSSCO, the Ginzburg-Landau theory at times proves to be inadequate [101] and the Lawrence-Doniach theory is used instead to account for extreme degrees of anisotropy[7] [102]. For example, in theoretical studies an effective charge carrier mass tensor has been adopted to account for the different mobilities in the different crystallographic directions, where the degree of the anisotrophy is described by the dimensionless superconductor anisotropy factor, $\zeta \equiv \frac{\lambda_c}{\lambda_{ab}} = \frac{\xi_{ab}}{\xi_c} = \left(\frac{m_c}{m_{ab}}\right)^{1/2}$ where m is the effective mass.

[7] It is this high degree of anisotropy that is responsible for many effects related to the flux line lattice in high temperature superconductors.

The coherence lengths for YBCO are $\xi_{ab}(0) \sim 15$ Å and $\xi_c(0) \sim 4$ Å. This value for $\xi_c(0)$ is approximately equal to the distance between the conducting CuO_2 planes and supports YBCO as being a quasi-two-dimensional superconductor; even more so for the extreme anisotropic BSCCO with $\zeta \gtrsim 150$ [103].

2.5 Technology and Applications

The global superconductivity market is projected to be US$45 billion by 2010 [104] with potential applications in bulk/large current, and microelectronic/small current devices. The latter comprise devices such as rf and microwave passive components, medical instrumentation and digital electronics, while the former include applications such as motors, generators, transformers, power transmission cables and energy storage systems.

2.5.1 Large-current applications

Initial attempts to construct electromagnets based on the zero resistance property of superconductors, thereby generating a magnet without the problem of Joule heating, were unsuccessful as only magnetic fields of a few millitesla were possible. Early measurements and experimentation was mostly on elements which, with the exception of Nb, were later identified as type-I superconductors. Much progress was made in the 1960s with type-II superconductors, notably with niobium alloys NbTi and Nb_3Sn, which led to the production of compact solenoidal magnets generating fields up to several tesla [105], with a critical operating temperature below ~ 25K.

Unlike the abovementioned conventional low-temperature superconductors, the weak-link problem has impacted directly on the fabrication of HTS electrical conductors, in particular wires and tapes [96, 105-107] used in large current applications. The two HTS systems that have been actively researched in the production of HTS wire/tapes are Ba-Sr-Ca-Cu-O (BSCCO) and YBCO. Early efforts to fabricate a superconducting wire technology for applications at 77 K focused initially on polycrystalline material. This fabrication route was thwarted by the weak-link problem, achieving typical critical current densities less than 500 A/cm^2 [108 - 110].

An attempt to overcome the weak-link problem was to align grains, thus overcoming the GB

misorientation problem in the bulk material by employing a mechanical-texturing technology [111], commonly referred to as the powder-in-tube (PIT) route. This fabrication route uses BSCCO as the material of choice, producing what is referred to as 'first generation' tapes. Typical critical current density values of these tapes about 15 000 A/cm^2 at $T = 77$ K. The PIT route involves packing superconducting BSCCO powder into silver tubes which are drawn and swaged into silver filaments about 1 mm thick; bundles of filaments are then rolled together to make tape. The PIT method of fabricating tapes decreases the number of low-energy GBs but does not eliminate weak-link characteristics. This is evident in the observation that typically only a fraction of the cross section of the BSCCO material in the tape carries current [96]. Despite BSCCO's high $T_c \approx 110$ K, it was the preferred HTS of choice over YBCO due to the ease with which it textured, which is related directly to its extreme anisotropic and micaceous nature.

The material of choice in 'second generation' tape is YBCO rather than BSCCO. This is due to the fact that many high-current applications, such as generators, motors, transformers and transmission cables, are associated with high magnetic fields. The magnetic field penetrates superconductors in the form of discrete bundles of magnetic flux lines. If these flux lines remain stationary (pinned), superconductivity can withstand the presence of supercurrent. However, if 'strong' pinning sites do not exist, and current is flowing in the superconducting material, flux lines move or 'creep' due to $\mathbf{J} \times \mathbf{H}$ forces resulting in a dissipation of energy [112, 113] and the vanishing of the critical current at fields below H_{c2}. The onset of the dissipation defines a critical field where perfect conductivity reappears. This critical field, H_{irr} defines the 'irreversibility line' and is particular noticeable in HTS most likely due to their high T_c, small ξ and low dimensionality. The region below H_{c2} and above H_{irr} may be thought of as a vortex liquid. From a practical perspective this region defines a condition where supercurrent rapidly decreases and renders superconducting material useless for many applications.

Due to BSCCO's extreme anisotropy it does not intrinsically pin as well as YBCO [114]. Hence, YBCO is the preferred material (even though BSCCO has a higher T_c), providing that it can easily be textured. [BSCCO tapes operating at 77 K in a magnetic field are limited by thermally activated flux motion, which ultimately acts as a resistance to current. It is for this reason that most field tests of motors, transformers and generators using BSCCO conductors

have been conducted at much lower temperatures - less than 30 K.]

Presently, the widely pursued 'second generation' so-called coated conductor technology, promises a cost effective way (operational temperature equal to 77 K) to manufacture flexible, high current density wires made with YBCO. The essential element of this technology is the deposition of YBCO as a biaxially aligned thick film onto a prepared textured substrate, which acts as a 'template'. This results in a superconducting layer with grain-to-grain in plane alignment [115]. For large scale fabrication of the 'second generation' conductors, two epitaxial methods have been pursued: ion beam assisted deposition (IBAD) [116-118] and rolling assisted biaxially aligned substrate process (RABITS)[115, 119], with typical in-plane textures of 8°and 12° respectively. For operation at 77 K the second generation conductors are very promising, in both cases yielding high critical current densities $> 10^5$ Acm^{-2}.

In order to improve J_c, both the IBAD and RABITS methods strive to improve grain alignment. Another possible solution is the doping of grain boundaries in order to improve connectivity (and to understand the grain boundary problem better), which in turn may help in lessening the required accuracy of grain alignment, thus lowering the production cost [120][121].

2.5.2 Small-current applications

Thin film microwave devices are one of the first small current applications of HTS. Industries [118, 122] are actively involved in developing low-noise oscillators, very-high-Q cavities, delay lines and antenna arrays primarily for use in the cellular market. Whereas normal metals confine microwave properties to the 'skin depth', superconductors do so to the penetration depth. The advantage that superconductors offer is much lower surface impedances: less than 0.8 mΩ in YBCO films at 10 GHz, which is almost two orders of magnitude lower than copper at $T = 77$ K. This advantage provides improved interference rejection capabilities in RF-filters placed in cellular-phone base-stations, thus improving the quality of reception. The present explosion of wireless Internet will no doubt benefit from the improvements that thin film superconductor devices offer.

Much research has being conducted to develop high quality YBCO films, which are grown epitaxially on various substrates via techniques such as ion beam sputtering and laser ablation. YBCO grains line up with the substrate on which the film is grown and films have J_c of several

million Acm^{-2} at 77 K.

Most commercially available superconducting electronic devices are based on the Josephson junction. The SQUID (superconducting quantum interference device) is the most sensitive device for the detection and measurement of magnetic fields and has a wide range of applications. The structure of a SQUID is essentially a superconducting loop with one or two Josephson junctions, and its operation depends upon the combination of flux quantisation and tunneling. SQUIDs, provided the quantity in question can be converted into a magnetic flux, are versatile measuring devices that are able to measure quantities such as current, voltage and resistance, and have been put to use in the search for gravity waves. An important use of SQUIDs is as a non-invasive probe in medicine. Tomographical images are constructed with an array of SQUIDs, which detect the minute magnetic fields generated by organs such as the brain or heart.

Two important areas of superconducting digital circuits are based on the Josephson junction: voltage-state logic, switching from the superconducting state (0) to normal state (1) in a time as short as 1 ps; and flux-state logic (transfer and control of single flux quanta) [124, 125]. The ultimate goal of both technologies is to develop superconducting supercomputers; but a more immediate aspiration seems to be the development of analogue-to-digital converters, digital filters, counters and switching arrays [126 - 128].

A more recent addition to the superconducting family is magnesium diboride (MgB_2), [14, 15] which has the highest recorded conventional superconductor critical temperature, with $T_c = 39$ K. This critical temperature suggests that MgB_2 is an extreme example of a phonon-mediated BCS superconductor [129]. Although the critical temperature is much lower than HTSs, it still enables the use of refrigerators rather than costly cryogens to cool below T_c. From a technological perspective, MgB_2 is straightforward to process and does not suffer the same weak-link problems that HTS materials do [130]. Several groups are producing light-weight superconductor magnets out of MgB_2 wire for magnetic-resonance-imaging systems and magnetic separation [130].

Chapter 3

Granular Superconductivity

Metallic films were the first granular superconductors to be studied [131, 132]. Here, metallic conventional superconductor films such as aluminium were oxidised to form grains with a small average size compared to the coherence length. Above T_c, grains were hardly coupled and little normal conduction could take place. Below T_c, grains were Josephson coupled and the entire film became superconducting.

Intergranular processes principally dominate electrical and magnetic properties of granular HTS systems, hence they are characterised as weakly coupled superconductors[1]. This intergranular 3D Josephson junction network (particularly polycrystalline material) forces transport current to meander and percolate in bulk material in order to minimise dissipation [133 - 135] and it forms the focus of this Chapter.

3.1 Experimental Evidence

One of the most compelling demonstrations of the percolation nature of the supercurrent in polycrystalline HTS material is provided by visual inspection through techniques such as scanning Hall probe, scanning tunnelling and SQUID microscopy [136 - 138]. Visual inspection has also shown that even in highly textured BSCCO/Ag tape and thick film superconductors, it is percolation and not flux pinning that limits the maximum current [139, 140]. This implies

[1] High quality HTS single crystals and epitaxial films containing no or few grain boundaries show no granular properties.

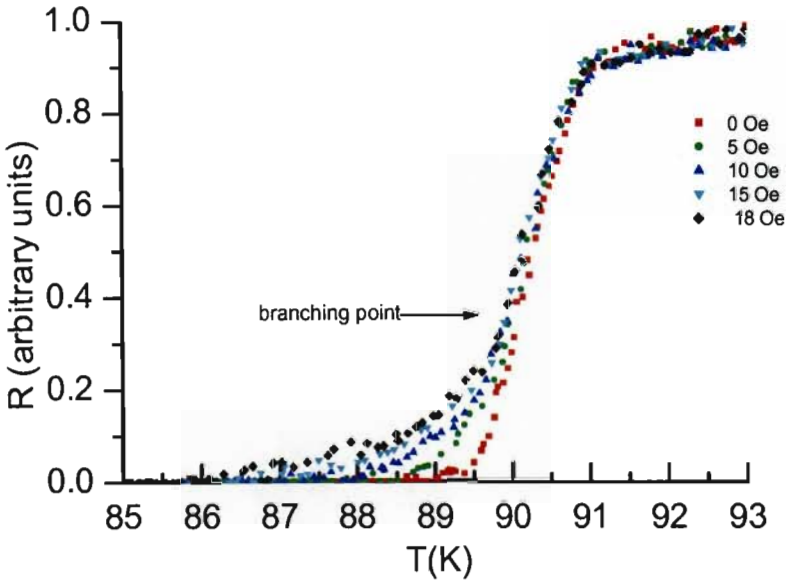

Figure 3-1: Resistance transistion of field-cooled YBCO, demonstrating the weak-link effect 'foot' region (present work).

that GBJs are important in the study of wire and tapes as well as bulk polycrystalline HTS material.

The existence of the 3D Josephson junction network is observed in field-cooled YBCO resistance versus temperature measurements[2], as shown in Figure 3-1. The magnetic field decouples grains and a 'foot-like' structure in the $R(T)$ behaviour below T_c is observed. As the specimen is cooled, all curves are nearly identical until the foot region, where there is a pronounced branching (see Figure 3-1). The common branching point corresponds to all of the available boundaries being in a dissipative state. The non-ohmic nature of the foot results from temperature and field dependency of dissipative grain boundary weak-links, which behave as Josephson junctions. The superconducting paths within the network are influenced by the applied field (ranging from 0 Oe to 18 Oe) and are sensitive to 'small' magnetic fields - typical of Josephson junctions. Similar $R(T)$ relations can be observed for a range of currents instead

[2] A Helmholtz coil was designed and constructed in order to test for the weak-link effect.

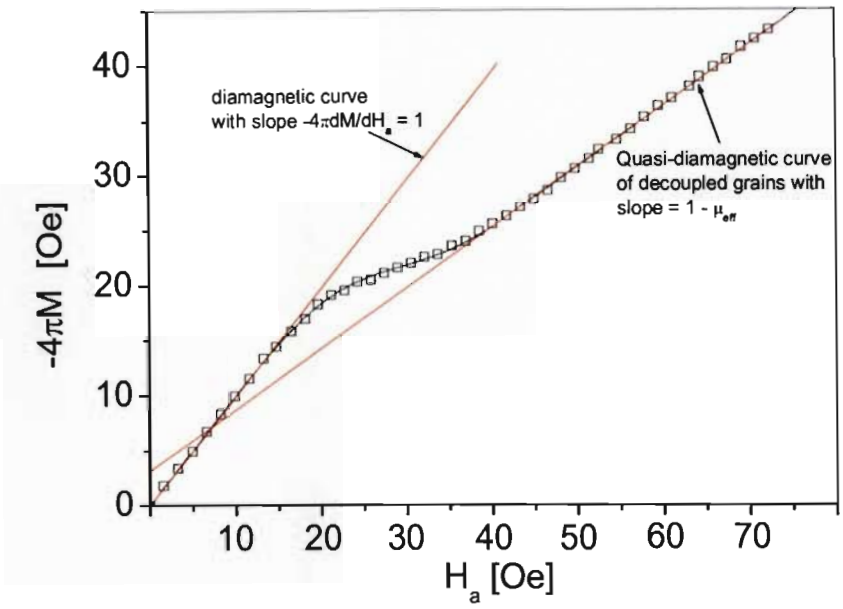

Figure 3-2: Low-field granular magnetisation behaviour of YBCO bar-specimens (11 x 2 x 2 mm^3), with long side parallel to the applied field, consisting of three distinct regions: diamagnetic, shoulder (intergranular flux penetration) and quasi-diamagnetic (present work).

of the applied magnetic field [141].

The granular nature of polycrystalline YBCO also manifests in low-field magnetisation measurements. Here a 'shoulder' feature is observed as grains become decoupled with the increase of an applied magnetic field, as shown in Figure 3-2.

Initially, the specimen is perfectly diamagnetic but as the magnetic field increases beyond the Josephson critical field, H_{c1j}, grains become decoupled and a quasi-diamagnetic region is observed with a slope related to an effective permeability, $1 - \mu_{eff}$. In this region the intergranular current has decreased dramatically, while within the grains the intragranular current increases, corresponding to the Meissner effect in the grains.

3.2 Josephson Junction Network

For a granular bulk HTS in an applied magnetic field less than a characteristic (Josephson) field, the screening current induced along the outer surface of the bulk restricts the field to a maximum depth defined by the Josephson penetration depth[3], λ_J [67], and the bulk of the specimen is perfectly diamagnetic if demagnetisation effects are ignored.

Clem in his columnar grain model [67] assumed a regular array with cubic grains of side length a_0 and $\lambda_J \gg a_0$ ('short' Josephson junction) and obtained the following expression for the Josephson penetration depth:

$$\lambda_J(t) = \sqrt{\frac{c\Phi_o}{4\pi^2 a_o J_{c0j}(t)\mu_{eff}(t)}}, \tag{3.1}$$

where $t = \frac{T}{T_C}$, Φ_o is the flux quantum, $J_{c0j}(t)$ is the junction critical current density and μ_{eff} the effective permeability resulting from grains in the Meissner state. Clem derived an expression for μ_{eff} where the granular HTS medium was approximated by parallel cylindrical grains of radius $R_g \simeq \frac{a_0}{2}$, parallel to the applied magnetic field as shown in Figure 3-3.

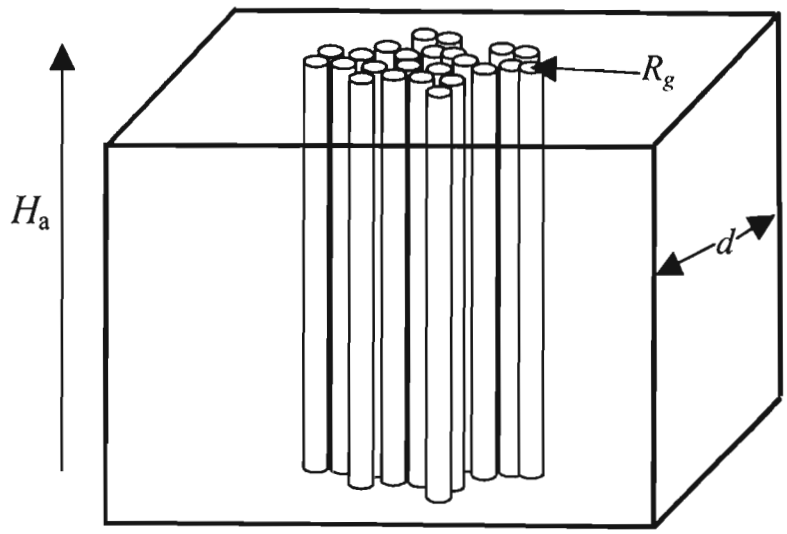

Figure 3-3: Columnar grain approximation: a bulk granular HTS of thickness d has superconducting grains approximated by cylinders of radius R_g aligned parallel to the applied field H_a [67].

[3]The Josephson penetration depth λ_j is for a junction what penetration depth λ is for the bulk and screens magnetic field from the junction.

In the above case Clem obtained

$$\mu_e(t) = f_n + f_s \left[\frac{2I_1(\Lambda)}{\Lambda I_0(\Lambda)}\right], \tag{3.2}$$

where f_n and $f_s = 1 - f_n$ are, respectively, the normal and superconducting volume fractions, and I_0 and I_1 are modified Bessel functions. The factor $\left[\frac{2I_1(\Lambda)}{\Lambda.I_0(\Lambda)}\right]$ is a measure of the fractional deviation of a cylindrical grain from the complete Meissner state, where $\Lambda = \Lambda(t) \equiv a_o/2\overline{\lambda_g}(t)$ and $\overline{\lambda_g}$ is the average granular penetration depth.

3.2.1 Effects of intergranular structural irregularities on critical currents

Experimentally, a distinguishing difference between bulk HTSs compared to conventional superconductors has been observed in the behaviour of critical current versus magnetic field, $I_c(H)$ [109, 142 - 145]. There are three distinct parts in a HTS's $I_c(H)$ behaviour. A low-field region where the critical current decays sharply, followed by a plateau region (unique to HTSs), and finally a high-field region where a rapid decrease in critical current is exhibited, as shown in the sketch in Figure 3-4. There are two contrasting explanations offered for this behaviour. Ekin *et al* [144, 145] suggest that the initial sharp decrease in the critical current is due to the decoupling of weak-links, the middle plateau region corresponds to remaining strong percolation paths and the final decay is attributed to the 'breaking' of these paths.

By contrast, E.Z. Meilikhov's model [100] is based on the structural differences of individual GBJs and suggests that it is too simplistic to expect grain-grain junctions to fall into two extremes; either weakly or strongly coupled junctions. Key to Meilikhov's model is the stochastic nature of HTS Josephson junctions, which is used to explain the unique plateau feature in $I_c(B)$ behaviour. Similar theoretical explanations by other groups have come to the same conclusion as Meilikhov [146, 147]. The explanation is based on inhomogeneities of the intergranular material, i.e. the 'insulator/normal' barrier part of a Josephson junction. Junctions are assumed to be 'stochastic' with a random distribution of the critical current over the area of the junction. The random nature of the current is associated with random structural fluctuations found within the barrier and was first studied in conventional tin-tin oxide-tin junctions [99]. Baron and Paterno in their book '*Physics and Applications of the Josephson Effect*' [98] comprehensively discuss the influence of the local nonuniform Josephson current profiles on

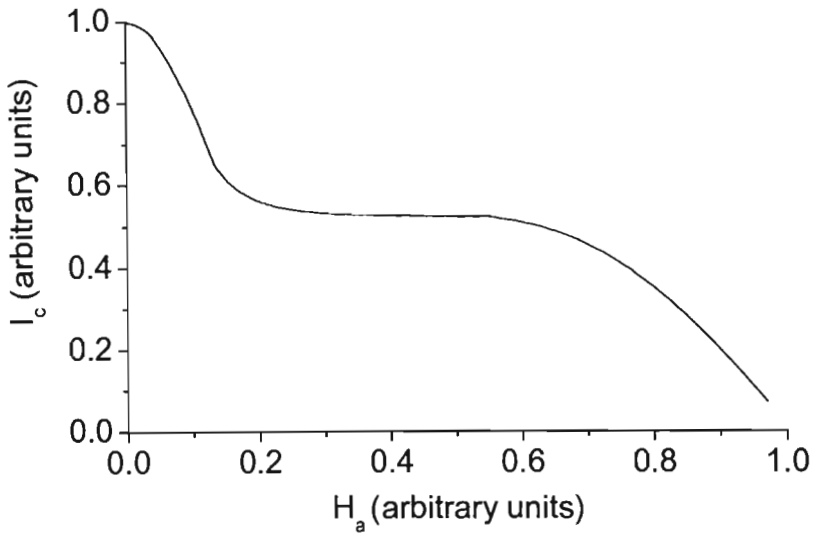

Figure 3-4: Curve showing typical bulk transport critical current density relationship in a HTS as a function of magnetic field.

$I_c(B)$ behaviour, where the physical shape of Josephson junction barriers determines different Josephson critical current profiles, as shown in theoretical curves of i_{cj} in Figure 3-5.

The effect of random fluctuation of a Josephson junction's critical current on the behaviour of $I_c(B)$ reveals a unique plateau feature where I_c is nearly independent of magnetic field, as shown in Figure 3-5 (red curve). This behaviour has been observed experimentally in single YBCO grain-boundaries [64].

Recent research gives further evidence for the random inhomogeneous nature of current in HTS junctions, more specifically GBJs [61, 148 - 151]. The evidence stems from a study concerning the intergranular critical current dependency on misorientation angle of GBs [152]. Here the inhomogeneous nature of the current is attributed to an interplay of faceting in GBs and the d-wave nature of HTSs.

To my knowledge, no association has been made between the field independent component (plateau) of the transport critical current and the interplay of GB faceting and the d-wave nature of HTS in the literature. This seems to imply that the unique field-independent component of $I_c(B)$ behaviour may be a direct consequence of a HTS's order parameter.

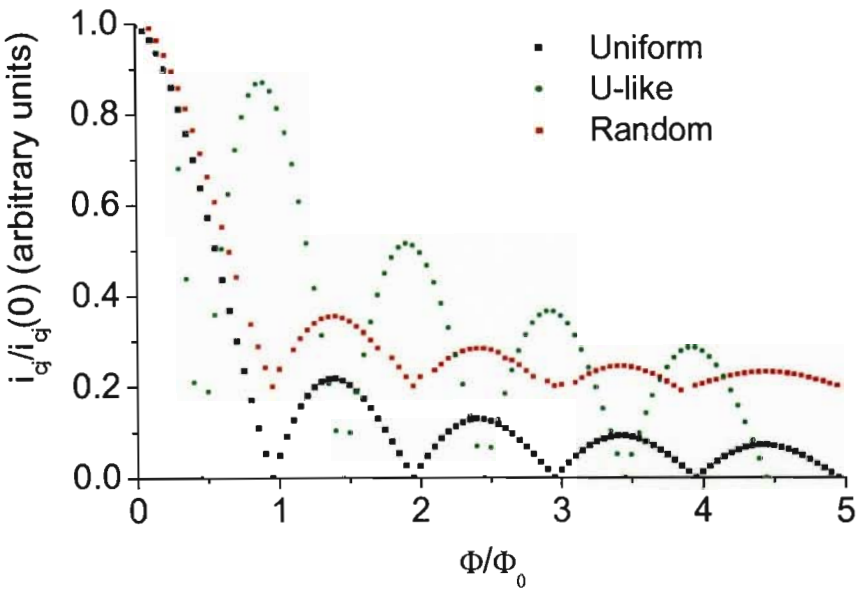

Figure 3-5: Critical current versus magnetic flux dependence of Josephson junctions for various local critical current density distributions: uniform, U-like and random [98].

3.2.2 Magnetic and morphology-dependent intergranular critical current density

Meilikhov and Doyle [153] published an expression for the critical current density dependence on magnetic field, $J_c(H)$, for polycrystalline HTSs. This expression, which is a fit to a magnetic field dependent critical current model incorporating structural fluctuations of Josephson current and the percolation nature of transport current in HTS [100], is used later in this thesis in analysing low-field magnetisation data. A unique feature of this $J_c(H)$ expression compared to other forms is the assumption that each Josephson junction in a 3D weak-link network has a nonuniform random Josephson current profile. A brief summary of this Josephson current model and the percolation nature of transport current is given below.

Structural fluctuations

Central to the development of the abovementioned model is the use of an expression, developed by Yanson [99], that describes the effect of random fluctuations on the Josephson critical current i_{cj}; its reduced form is

$$\frac{i_{cj}(b)}{i_{cj}(0)} = \left[\left(\frac{\sin b}{b}\right)^2 I_1^2(b) + \left(\frac{\cos b}{b}\right)^2 I_2^2(b)\right]^{1/2}, \tag{3.3}$$

where $b = 2\pi\overline{\lambda_g}a_0 B/\Phi_0$ is the reduced flux in the junction. Here a_0, is the dimension of the junction (average grain size) perpendicular to the magnetic field $B_\perp$, Φ_0 is the magnetic flux quantum and $\overline{\lambda_g}$ is the average granular magnetic penetration depth. The functions $I_1^2(b)$ and $I_2^2(b)$ have the following forms,

$$I_1^2(b) = 1 + 2\gamma^2\left\{\sum_{n=1}^{\infty}\alpha_n^2\frac{1-\exp(-2\pi f)}{\pi f}\left[\sum_{n=1}^{\infty}\beta_n\right]^2\right\}$$

and

$$I_2^2(b) = 2\gamma^2\left\{\sum_{n=1}^{\infty}\alpha_{n-1/2}^2\frac{1-\exp(-2\pi f)}{\pi f}\left[\sum_{n=1}^{\infty}\beta_{n-1/2}\right]^2\right\},$$

respectively, where $\alpha_n^2 = \left(\frac{b^2}{b^2-\pi^2n^2}\right)^2\frac{1}{1+n^2/f^2}$, $\beta_n = \left(\frac{b^2}{b^2-\pi^2n^2}\right)\frac{1}{1+n^2/f^2}$, $f = \frac{1}{2\pi}\left(\frac{a_0}{r_0}\right)$ and $\pi f\gamma^2 = \overline{\left(j_c - \overline{j_c}\right)^2}/\left(\overline{j_c}\right)^2$. Here j_c and $\overline{j_c}$ are the local and mean critical current densities respectively, and r_0 is the correlation radius of the junction irregularities, which is determined by the following spatial autocorrelation function

$$\overline{\left[j_c(x_1) - \overline{j_c}\right]\left[j_c(x_2) - \overline{j_c}\right]} = \overline{\left(j_c - \overline{j_c}\right)^2}\exp\left(\frac{-|x_1 - x_2|}{r_0}\right), \tag{3.4}$$

where x_n is a position in the plane of the junction.

According to the above model the local critical current density is dependent on three parameters [100]: (i) the size of the junction a_0 which relates the magnetic field to the reduced flux in the junction b; (ii) the parameter f, which is related to the correlation radius r_0 of structural irregularities in the junction; and (iii) γ and f, which determine the average modulation

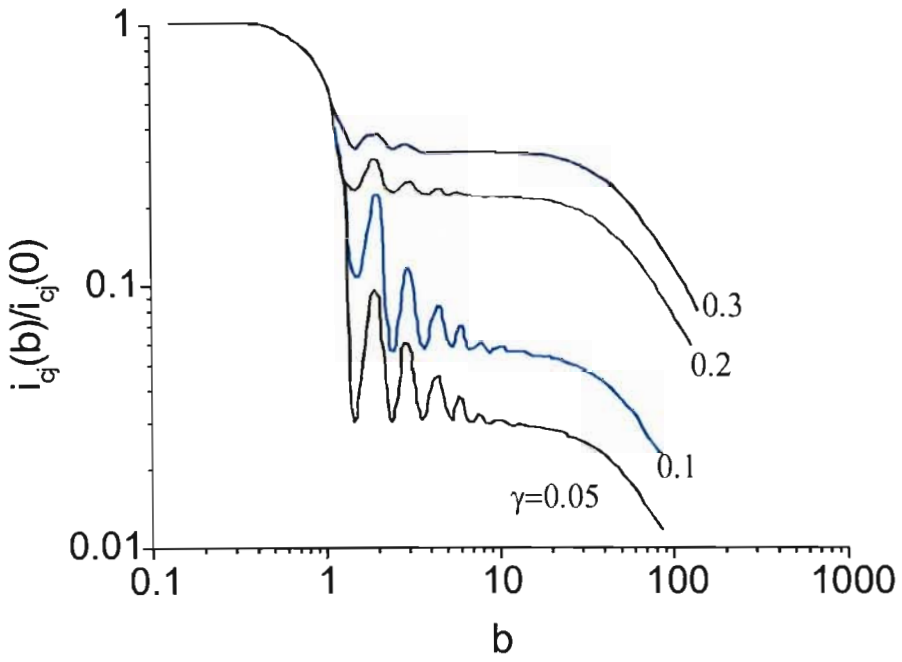

Figure 3-6: Reduced critical current versus dimensionless magnetic field of a single Josephson junction with random structural fluctuations, for $f = 100$ and $\gamma = 0.05$,0.1, 0.2 and 0.3 [100].

depth of the critical current density in the junction, and are dependent on the irregularities. [In HTS Josephson junctions, the source of the random/fluctuating nature of the critical current density may not originate only from structural irregularities but also, as pointed out in the previous section, from an interplay of intergranular faceting and the d-wave nature of the order parameter.]

Figure 3-6 by use of Equation 3.3 demonstrates the magnetic dependence of the critical current of a single Josephson junction with a random fluctuation of a Josephson junction's critical current (similarly as in Figure 3-5). Here the two structurally sensitive parameters were set with $f = 100$ for various values of γ.

Percolation considerations

A percolation model, described in Reference [154] and summarised below, assumes a set of independent Josephson junctions, connecting randomly oriented square superconducting grains. In order to calculate the transport critical current $I_c(B)$ for bulk polycrystalline HTSs, a 'contact'

critical current (intergranular) distribution function $f(i_{c0})$ of junctions was introduced, where that $i_{c0} \equiv i_{cj}(0)$. Experimental evidence suggest $f(i_{c0})$ has the following truncated power-law form,

$$f(i_{c0}) = \begin{matrix} \frac{n+1}{i_0}\left(\frac{i_{c0}}{i_0}\right)^n, & i_{c0} < i_0 \\ 0, & i_{c0} > i_0 \end{matrix} \tag{3.5}$$

with $n = \left(\xi/\overline{d}\right) - 1$ and $\overline{d}$ is the average junction thickness.

The percolation model's network critical current $I_c(B)$ is proportional (and limited) to the smallest critical current i^*(weakest link) that maximises the expression:

$$i_c(B) = const(P - P_c)^{t_i} i^*(P), \tag{3.6}$$

where

$$P(i^*) = \int_{i^*}^{\infty} f(i_{cj}) di_{cj} \tag{3.7}$$

is the inverse of $i^*(P)$ and is the fraction of weak-links which have critical currents $i_{cj} > i^*$. The percolation limit P_c, and the critical conductivity index t_i, do not significantly affect the model and lie within the following ranges: $0.25 < P_c < 0.6$ and $1.0 < t_i < 1.5$. If for a 'cluster of junctions' $P(i^*) > Pc$ then it will provide a path for the superconducting current through the whole system.

Assuming a uniformly square junction of dimensions a_0, with random grain orientation and a strong magnetic field dependence, a modified distribution function is obtained

$$f_j(i_{cj}) = \frac{2}{\pi}\int_0^{\pi/2} f\left\{i_{c0}\left[i_{cj}(b\sin\varphi)\right]\right\} \left|\frac{\partial i_{c0}}{\partial i_{cj}\,(b\sin\varphi)}\right| d\varphi, \tag{3.8}$$

where φ is the angle between the junction plane and the magnetic field.

In order to determine the critical current $I_c(b)$ in the 3D weak-link network of Josephson junctions, the distribution function of Equation 3.5 is substituted into Equation 3.8 and the modified distribution function $f_j(i_{cj})$ is determined; this is then substituted in Equation 3.7 to obtain $i^*(P)$, which is maximised. Meilikhov's results [100] with $f = 100$ and $\gamma = 0.02$, 0.1 and 0.3 are reproduced in Figure 3-7.

It is interesting to note that the 'plateau' region in the curves shown in Figure 3-7 increases

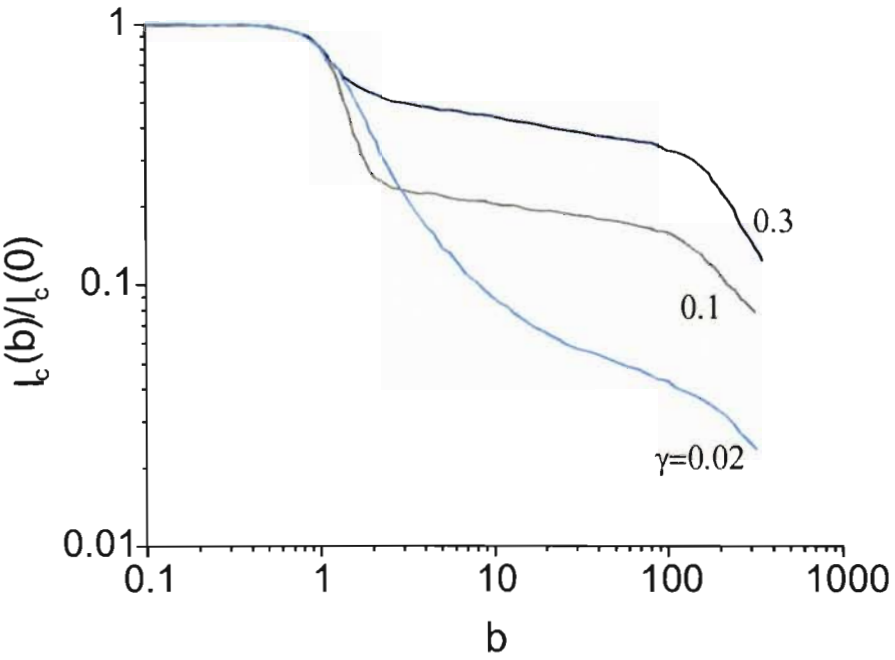

Figure 3-7: Reduced critical current versus dimensionless magnetic field of Josephson junctions with random structural fluctuations, for $f = 100$ and $\gamma = 0.02$, 0.1 and 0.3. [100]

with an increase in γ. This results is an increasing field independent part of the $I_c(b)$ curve, which is obviously advantageous in high power applications. It is suggested here that a possible route to improve the plateau region would be to increase γ though its association with the irregularities in GBJs via the process of doping.

Meilikhov and Doyle [153] fitted the following expression,

$$\frac{J_c(b)}{J_{c0}} = a \exp(b/b_0)^m + c, \tag{3.9}$$

to the above results, where the constant c accounts for the plateau feature in critical current versus magnetic field results with $m = 1$ and $a \approx 1.25$.

Section 1.4.2 introduced Bean's critical state model (CSM). The following section introduces an intergranular CSM, based on Equation 3.9.

3.3 Intergranular critical state model

As discussed in Section 3.1, assuming a zero demagnetisation coefficient, a bulk granular HTS is in the Meissner state for the applied magnetic field $H_a < H_{c1j}$, where H_{c1j} is the intergranular critical field for the GBJs in the low-field region, $0 \leq H_a \leq H_{c1g}$, where H_{c1g} is the lower critical field for the HTS grains. When $H_a \geq H_{c1j}$ it becomes energetically favourable for Josephson currents to form Josephson vortices, each carrying one magnetic flux quantum Φ_0, along the grain-boundaries. In a similar manner to Abrikosov vortices in conventional type-II superconductors, Josephson-vortices penetrate into intergranular material with a characteristic (Josephson) penetration depth λ_J. Increase of Josephson fluxon penetration into intergranular material is eventually prevented by current loops consisting of percolation networks of coherent coupled grains, which extend azimuthally around the HTS specimen, and smaller current loops around clusters of coupled grains[4].

An intergranular CSM can be used to determine the intergranular critical currents from low-field magnetisation measurements. There are numerous CSMs which discuss HTS low-field magnetisation measurements [155]. Doyle and Doyle [156] have developed an intergranular CSM from the critical state equation given by Equation 1.56 together with an empirical expression for the intergranular critical current density, which later was shown theoretically [153] to be consistent with Equation 3.9. The Doyle model is fitted to isothermal zero-field-cooled magnetisation measurements, $M(H_a, T)$ in the low-field region. The remainder of this section will review their treatment, and will be used later in this thesis due to morphological insights it offers in the analyses of magnetisation measurements in polycrystalline HTSs.

The model considers that a zero-field cooled long cylindrical HTS specimen of radius R that is cooled to below T_c. Once a temperature of study T is reached, an applied field H_a is increased from zero within the low-field region. For fields greater than H_{c1j}, Josephson fluxons penetrate irreversibly into the intergranular material with a characteristic length, the Josephson penetration depth, λ_j. The Josephson penetration depth is assumed to be of the same order or larger than the average grain size, a_0. This assumption is later confirmed to be correct. The field penetration into intragranular material (grains) extends to a depth equal to an average

[4] In this treatment conventional flux pinning in the junctions is ignored.

granular penetration depth $\overline{\lambda_g}$.

The local mean internal field $\mathbf{H}(\mathbf{r})$ was assumed to be cylindrically symmetric and parallel to $\mathbf{H}_a$, with a radial field gradient given by a cylindrically symmetric form of the CSM:

$$\frac{dH}{dr} = \pm \left(\frac{4\pi}{c}\right) J_{cj}\left(H,T\right), \tag{3.10}$$

where $J_{cj}\left(H,T\right)$ is the effective local shielding current density (equivalent to the transport current density).

The magnetisation of a specimen, with a radius R and an effective permeability $\mu_{eff}(T) \equiv B/H$, is

$$-4\pi M = H_a - \frac{2\mu_{eff}}{R^2}\int_0^R H(r) r dr. \tag{3.11}$$

An expression, with superconducting and morphological parameters, for an explicit form of $M(H_a,T)$ from Equations 3.10 and 3.11 is achieved by developing explicit expressions for $\mu_{eff}(T)$ and $J_{cj}(H,T)$. The explicit expression chosen for $\mu_{eff}(T)$ is Equation 3.2, which was discussed in Section 3.2.

The intergranular tunnelling current density $J_{cj}\left(H,T\right)$ can be represented (Section 1.4.3) as

$$J_{cj}\left(H,T\right) = J_{c0j}(T)G(H,T), \tag{3.12}$$

where $J_{cj}(H,T) = I_{cj}(T)/A$, and A is the area of a junction. It is necessary to modify $J_{c0j}(T)$ and $G(H,T)$ to adequately describe the HTS system of a percolative network comprised of GBJs.

Variations of the field dependent component G have been discussed by several authors [40, 161, 162] and used in critical state models. These range from Kim-type models [163, 164] ($G \propto (1/H)$ or $G \propto (1 - H/H_0)^{-1}$), exponential dependence ($G \propto \exp(1 - H/H_0)^{-n}$), where H_0 and n are model-specific parameters or are determined empirically, to G being independent of H (Bean model). The resulting modified CSMs were then applied to the magnetisation behaviour of HTSs in the low-field region [100, 155].

The work of Meilkhov [100, 154] on polycrystalline HTS material, which includes considerations of current fluctuations within GBJs and percolation behaviour as discussed in Section 3.2,

predicts the characteristic intermediate field-independent plateau feature of $J_c(H)$. This led Doyle and Doyle [156] to use the following empirical expression for the critical current density for polycrystalline HTS material in the present low-field region[5]

$$J_c\left(H,T\right) = J_{c0}\left(T\right)\left[\exp\left(\frac{-H}{H_0}\right) + \delta\right] \tag{3.13}$$

or

$$J_c\left(H,T\right) = J_{c0j}\left(T\right)\exp\left(\frac{-H}{H_0}\right) + J_{c1j}(T), \tag{3.14}$$

where, from Ambegaokar-Baratoff theory (Equation 1.60) $J_{c0j}(T) = J_{c0}F(T)$, $J_{c1j}(T) = \delta J_{c0j}$ where δ is a characteristic constant of the junction network. The model parameter $H_0 = H_0(T)$ is a characteristic field of the average junction.

The empirical expression for the critical current density J_c given by Equation 3.13 is substituted into Equation 3.10 and integrated to obtain the average local internal field,

$$H(r) = H_0 \ln\left[\left\{\left(1+\delta\alpha\right)e^{-\epsilon(1-r/R)} - 1\right\}/\delta\right] \tag{3.15}$$

where R is the specimen raduis, $\alpha = \exp(H_a/H_0)$, $\epsilon = (4\pi/c)\,J_{c0}\delta R/H_0$ and $\delta = J_{c1}(T)/J_{c0}(T)$. The reduced flux penetration distance into the specimen is defined as $x_0 = 1 - r_0/R$, where r_0 is the flux penetration radius (i.e. such that $\mu_{eff}H = 0$ for $r \leq r_0$), and is then given by

$$x_0 = \frac{1}{\epsilon}\ln\left[\frac{1+\delta\alpha}{1+\delta}\right].$$

To determine the magnetisation of the specimen Equation 3.15 is substituted into Equation 3.11 and then integrated by parts, yielding:

for $x_0 \leq 1$,

$$-4\pi M = H_a\left[1-\mu_{eff}\right] + H_a\left[1-\mu_{eff}\right] + \tag{3.16}$$

$$H_0\left[\frac{\epsilon}{6}\left\{1-(1-x_0)^3\right\} + \frac{1}{\epsilon^2}\left|\sum_{k=0}^{\infty}Q_k z^{2+2k} + 2\Omega\sum_{k=0}^{\infty}R_k z^{1+2k} - \Omega^2\ln\left(\sinh z\right)\right|_{z=\ln(1+\delta)}^{z=\Omega+\epsilon}\right],$$

[5]The expression was later theoretically confirmed by Equation 3.9 [153].

and for $x_0 \geq 1$,

$$-4\pi M = H_a\left[1-\mu_{eff}\right] + H_0\left[\frac{\epsilon}{6}+\frac{1}{\epsilon^2}\left|\sum_{k=0}^{\infty} Q_k z^{2+2k} + 2\Omega\sum_{k=0}^{\infty} R_k z^{1+2k} - \Omega^2 \ln\left(\sinh z\right)\right|_{z=\Omega}^{z=\Omega+\epsilon}\right], \tag{3.17}$$

where $\Omega = \ln(1+\delta\alpha) - \epsilon$, $Q = 2^{2k}B_{2k}/(2+2k)(2k)!$, $R_k = 2^{2k}B_{2k}/(2k+1)!$ and B_{2k} are the Bernoulli numbers. Equations 3.16 and 3.17 are valid for all $|z| \leq \pi$ and the series converges sufficiently by $k = 4$. Finally, Equations 3.16 and 3.17 are fitted to experimental isothermal $M(H_a)$ curves where the temperature-dependent variables $J_{c0}(T)$, $\delta = J_{c1}(T)/J_{c0}(T)$, $H_0(T)$ and $\mu_{eff}(T)$ are free fitting parameters.

3.4 Characteristic fitting parameters

In this study careful selection of appropriate models for parameters has been made in order to constrain fits to achieve maximum insight into understanding the role grain boundary Josephson junctions (GBJs) have on the critical current in polycrystalline HTS. Here, three of the four fitting parameters, $J_{c0}(T)$, $\delta = J_{c1}(T)/J_{c0}(T)$ and $H_0(T)$, which are related to the critical-state model reviewed in the previous section, will be discussed. The effective permeability, μ_{eff}, fitting parameter has already been discussed in Section 3.2.

3.4.1 Zero-field critical current density, $J_{c0}(t)$

A modified Ambegaokar-Baratoff model (Equation 1.60) for a single junction, corrected for order parameter suppression at the junction interfaces [157 - 160]

$$J_{c0}(t) = J_{c0I}\left\{\frac{\Delta_i(t)}{\Delta_i(0)}\tanh\left[\frac{\Delta_i(t)}{2k_B t T_c}\right]\right\} \tag{3.18}$$

is fitted to $J_{c0}(T)$ data. Here $J_{c0I} = \left[\frac{4}{\pi a_o^2}\right]\left[\frac{\pi\Delta_i(0)}{eR_n}\right]$, R_n is the normal state junction resistance, Δ_i is the suppressed gap parameter at the junction boundaries given by $\Delta_i = \Delta_\infty(t)\tanh[\omega(t)]$ with $\omega(t) = x_o/(\sqrt{2}\xi_S(t))$ where x_o is the suppression range for the gap parameter near the junction boundaries, $\Delta_\infty(t)$ is the gap parameter far from the junction boundaries and $\xi_S(t) \propto \sqrt{(1+t^2)/(1-t^2)}$ is the effective coherence length in the supercon-

ducting material.

The use of Equation 3.18 in the fitting process, which is to be discussed in detail in Section 5.2, results in average normal state junction (GBJ) resistance values R_n.

3.4.2 Field-independent reduced critical current density, $\delta(T)$

The critical current density expression used in the CSM, Equation 3.14, includes a field independent reduced critical current density component $J_c(T)$ and a field dependent component $J_c(T,H)$, which decreases exponentially with applied field. A unique feature of the CSM is the field-independent parameter $\delta = J_{c1}(T)/J_{c0}(T)$. Due to its association with the morphological parameter γ discussed in Section 3.2.2, δ can be expressed in the following form

$$\delta \approx \left[\frac{2r_0}{a_0}\right]^{1/2} \psi_r, \tag{3.19}$$

where a_0 is the average grain diameter, $\psi_r = \sqrt{\overline{(j_c - \overline{j_c})^2} / \overline{(j_c)}^2}$, is the root-mean-squared relative fluctuation of critical current density in the average GBJ, and r_0 is the correlation radius of the fluctuations, a measure of the inhomogeneities, which is determined by the autocorrelation function Equation 3.4.

The empirical expression for the critical current density for polycrystalline HTS material, Equation 3.14, suggests that $\delta = J_{c1}(T)/J_{c0}(T)$ is independent of temperature, as was assumed by Doyle and Doyle [156]. However, it is quite possible that δ is a function of temperature indirectly, which will discussed later.

A number of publications have studied structural fluctuations within Josephson junctions [99, 147, 165, 166]. For example, Yanson [99] has studied the effect of thermal and structural fluctuations on single Sn-SnO-Sn junctions. He observed that thermal fluctuations destroyed superconductivity in the junction. On the other hand, structural fluctuations within the barrier (SnO) did not destroy superconductivity but 'smeared out' the $I(H)$ interference pattern to a constant current, independent of magnetic field. Barone *et al* [165] studied photosensitive Josephson junctions (Pb-CdS-In) and derived values for the average amplitude of fluctuations from the average correlation radius.

Fehrenbacher *et al* [147] theoretically investigated different types of disorders, including

stochastic disorder, within Josephson junctions. They also predicted the existence of the $I(H)$ plateau for random disorder within the junction. They found that the plateau depends on the ratio of $\overline{r_0}/\lambda_J$, where $\overline{r_0}$ is the length scale of disorder (average correlation length), and is associated with pinning centres and the average Josephson penetration depth λ_J. They concluded that for $\overline{r_0}/\lambda_J \approx 1$ there is no plateau, and that the plateau would exist only for the case of $\overline{r_0}/\lambda_J \ll 1$.

Sarnelli *et al* [166] found that a current component independent of field strength is associated with thin-film YBCO GBJ bicrystals. They found that the 'residual current' (plateau) was sensitive to ozone and the misorientation angle. A general decrease of the residual current was observed with temperature, with a rapid decrease near T_c.

More recently, the study of structural fluctuations has been investigated by the use of the abovementioned intergranular CSM, Equation 3.13. Studying the CSM's characteristic fitting parameters versus temperature, various aspects of the nature of polycrystalline HTS material have been observed [156]. YBCO specimens with different average grain sizes, 2.2 μm and 5.8 μm, were found to have constant $\delta = 0.01$ and 0.042 respectively in the temperature range 69 K to $T_c(= 92.5$ K). In another YBCO study [167], it was observed that δ significantly increases in the temperature range $50 < T < 70$ K . This increase was attributed to the oxygen deficient YBCO phase in the GBJ becoming superconducting. We have studied the variation of δ with silver doping [120], and this research will be discussed in detail in Chapter 5.

3.4.3 Weak-link network characteristic field, $H_0(t)$

In this work a 'short' weak-link junction model for $H_0(t)$ behaviour has been assumed, because the Josephson penetration length λ_j (Equation 3.1) is estimated to be greater than the average junction length a_0; this is proved to be correct later. The characteristic field $H_0(t)$ has the following form,

$$H_0(t) = \eta \frac{B_o}{\mu_{eff}(t)} \cong \eta \frac{\phi_o}{\mu_{eff}(t)[2\lambda_g(t) + d]a_o}, \tag{3.20}$$

where B_o is the induction in the plane of an average junction corresponding to a single flux quantum ϕ_o in the junction, $\eta \approx 1$ is a geometrical/morphological constant which allows for superconducting anisotropy, grain-shape anisotropy and average GBJ orientation and d is the effective junction-barrier width [167].

3.5 Reversible Magnetisation - High-field Analysis

In this study, a modified approach to Doyle and Doyle's low-field analysis [156] of polycrystalline HTSs has been developed. This modified approach results in a more constrained intergranular analysis and is due to the inclusion of high-field magnetisation measurements.

In their low-field magnetisation measurement analysis, Doyle and Doyle compared results of fitting the parameter $\mu_e(t)$ to Clem's columnar model, Equation 3.2. The comparison, using the penetration depth $\lambda(T = 0)$ as a fitting parameter, was accomplished with the use of the Gorter-Casimir two fluid, Equation 1.16 and the BCS penetration depth, Equation 1.52.

In this study an average granular penetration depth $\overline{\lambda_g}$ is determined from isothermal high-field magnetisation measurements in the intermediate-field region, $H_{c1} \ll H \ll H_{c2}$. In this region the irreversible term of the magnetisation response, M_{irr}, is equal to zero (more or less)[6]. Kogan *et al* [168, 169] developed a procedure to extract the penetration depth from the remaining magnetic component in this region, that is, the equilibrium/reversible magnetisation term M_{eq} [the Kogan procedure assumes two magnetisation componets, $M_{irr}+ M_{eq}$]. The equilibrium magnetisation term is a consequence of supercurrrents associated with vortices penetrating the superconductor.

3.5.1 Kogan analysis - an outline

Kogan *et al's* work [168, 169] may be summarised briefly as follows. Kogan *et al* noted that the high values of GL-parameter, κ associated with HTSs, allow a study of magnetic field penetration depth based on magnetic measurements in the field range $H_{c1} \ll H \ll H_{c2}$. In this range, the HTSs act as ordinary London superconductors. This results from the fact that the small magnetic cores are widely separated and almost uniform field penetration can be assumed due to vortex overlap, that is, λ significantly exceeds average intervortex spacing L ($\xi \ll L \ll \lambda$).

Kogan et al showed that in this field range M_{eq} is linear in the logarithm of the applied field

[6]This implies the pinning is inadequate to pin flux lines and as a result the intra-critical current approaches zero

and for polycrystalline HTSs the slope of $M_{eq}(\ln H)$ is given by:

$$\frac{dM_{eq}}{d\ln(|H|)} = \frac{\Phi_0}{64\pi^2\overline{\lambda_g}^2} g(\zeta) \tag{3.21}$$

$$\text{where } g(\zeta) = \zeta^{-1/3}\left[\zeta + \left(\zeta^2 - 1\right)^{-1/2} \ln\left(\left(\zeta^2 - 1\right)^{1/2} + \zeta\right)\right],$$

and Φ_0 is the flux quantum, $\overline{\lambda_g} = \left[\lambda_{ab}^2 \lambda_c\right]^{1/3}$is the average granular penetration depth and $g(\zeta)$ is a correction factor that depends on a superconductor anisotropy factor $\zeta = \frac{\lambda_c}{\lambda_{ab}}$, which originates when anisotropy is incorporated into GL theory via an effective mass tensor. The value for ζ in the literature varies from 4-7 [170, 171]; in this work a value of $\zeta = 5$ was assumed, which results in a value of $g(\zeta) = 3.2$.

As discussed above, an important consequence of using high-field magnetisation measurements to establish $\lambda(t)$ is that it gives the CSM low-field analysis a more experimental foundation, i.e. $\lambda(t)$ data is not theoretically calculated but derived from measurements. Furthermore, Doyle and Doyle's comparison with Clem's columnar model relied on measurements taken from SEM images in order to estimate an average grain size. The estimation of grain size based on SEM images can be problematic due to variations of grain size, grain-boundaries being difficult to identify and clusters of strongly coupled grains acting magnetically as an effective (larger) grain or 'cluster'. In this study an effective radius r_{eff}, a measure of strongly coupled grains (or cluster size), is preferred as a fitting parameter, instead of the penetration depth, when comparing $\mu_e(t)$ data (derived from CSM analysis) to Clem's model.

Chapter 4

Experimental

Silver (Ag) doped YBCO was chosen for this study due to Ag being used in many different HTS applications, such as: sheath material in wire and tapes, target, substrate and buffer material and an additive in thin/thick films [172 - 175]. The use of Ag has been identified as a factor in resistance of the normal state as well as improving mechanical strength [176] and current-carrying capacity. One of the most important parameters in determining the usefulness of a superconductor is the critical current density J_c. The limitations of J_c are the occurrence of weak-link GBJs and weak flux-pinning strength. All of the abovementioned applications have GBJ in varying concentrations and the effect of Ag doping on GBJ would make an interesting study. Hence, specimen morphology, magnetisation and resistance measurements were performed on various Ag doped YBCO specimens in an attempt to understand the role of Ag in increasing J_c in HTS material, specifically in bulk polycrystalline YBCO.

4.1 Specimen preparation and doping

High quality (99% pure) YBCO powder was purchased from Seattle Ceramics Specialists, Incorporated with the particle size of the powder falling in the range: 1-3 μm. The YBCO powder was pressed directly into bars[1] with dimensions, 11 x 2 x 2 mm. The powder was placed between two 'spacers' and pressed for a period of approximately 15 minutes under uniaxial pressure at

[1] This route skipped the typical laborious process of cutting bars from a sintered YBCO disc specimen [156, 160, 167], which wasted valuable YBCO powder.

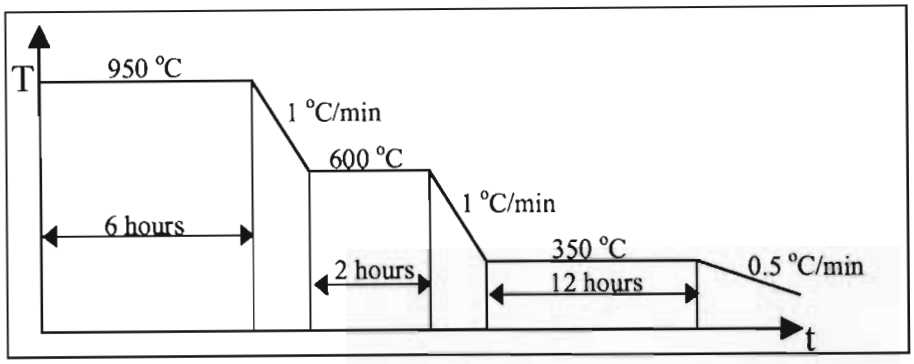

Figure 4-1: Typical temperature profile of sintering and annealing process.

about 45 MPa.

4.1.1 Silver doping experiment

In several Ag doping experiments, silver in the form of silver oxide (Ag_2O) was introduced to YBCO's constituent reagent material [177, 178]. Silver introduced via this route not only collects in grain boundaries but also freely in grains. In the present investigation we wished only to dope the grain boundaries and the following method was used: Ag doped specimens were prepared by introducing Ag_2O to the YBCO precursor powder prior to the heating process. Introducing Ag by this means facilitated silver to reside in grain boundaries, as the SEM images in Section 4.2 show.

The following specimens were prepared, with percentage Ag doping by weight: YBCO (0% Ag), YBCO (2% Ag), YBCO (5% Ag) and YBCO (10% Ag). Mixing of the YBCO and Ag_2O powder was done in a mechanical mixer for approximately 10 minutes and then pressed.

The pressed specimens were sintered in an oxygen atmosphere at 950 ^{0}C for 6 hours and annealed at 350 ^{0}C (YBCO absorbs oxygen best at this temperature) for 12 hours. The duration of the sintering process was empirically determined with the objective that the Ag should preferentially remain in grain boundaries. It was hypothesised that the longer the sintering time the greater the chance that Ag might accumulate intragranularly, which we did not want. The following program outlines the exact temperature profile used:

Once the above heat treatment was complete the density of each specimen was determined;

Table 4.1: Ag- experiment specimen densities

Specimen (YBCO)	Density
0% Ag	5.5 g/cm^3 ± 0.1
2% Ag	5.5 g/cm^3 ± 0.1
5% Ag	5.8 g/cm^3 ± 0.1
10% Ag	6.0 g/cm^3 ± 0.1

the results are shown in Table 4.1.

4.2 Specimen Morphology

Scanning electron microscope (SEM) and optical microscope images were taken of the Ag doped specimens to confirm that Ag had collected in the grain-boundaries (GBs) and not in the grains.

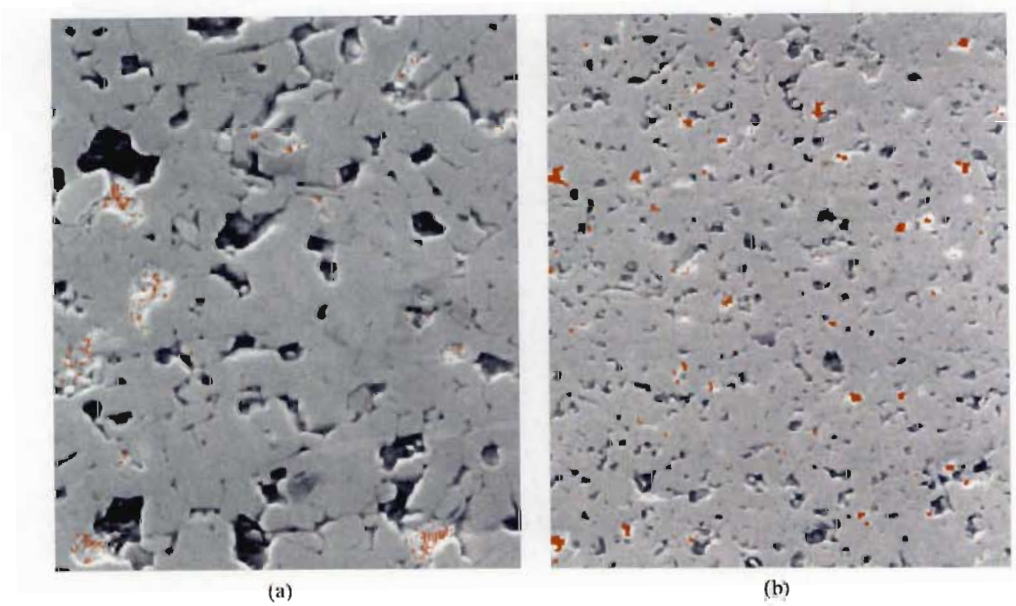

Figure 4-2: SEM images - 5% Ag-doped specimen (a) x 1200 and (b) x 500 magnification. EDX confirmed that Ag, shown as red, collected predominantly in the grain-boundaries and voids.

SEM images of the 5% Ag doped specimen are shown in Figure 4-2, depicting the typically granular nature of all fabricated specimens. The concentration of Ag in GBs and mainly in voids was confirmed using Energy Dispersive X-Ray Analysis (EDX); the Ag is marked red in Figure

4-2. The SEM evidence of Ag collecting in the GBs is more evident in the 2D 'impessions' left behind by grains that have been plucked/cleaved out during the polishing process of specimen preparation, thus exposing the GBs.

Optical microscope images of both the 0% Ag doped and 5% Ag doped specimens are shown in Figure 4-3.

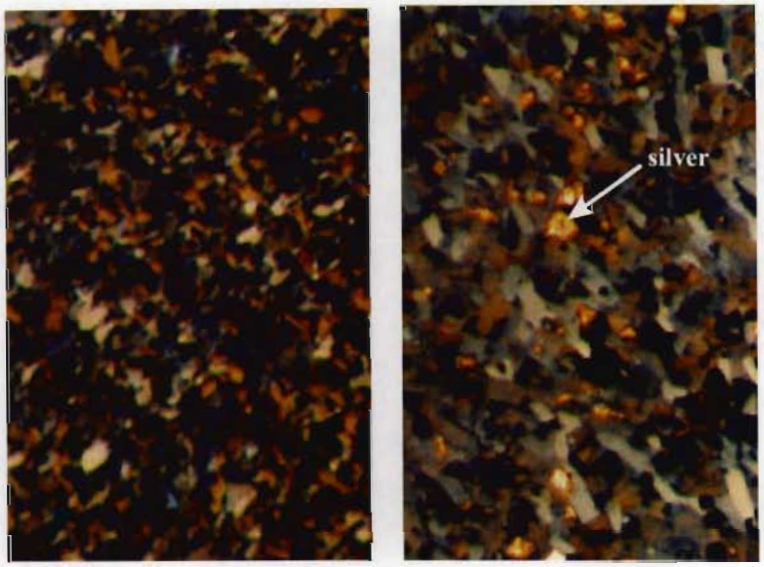

Figure 4-3: Optical images x 128 magnification (a) 0% Ag-doped specimen and (b) 5% Ag-doped specimen, with silver 'clusters' apparent.

A noticeable difference between the doped and undoped specimens, as shown in Figure 4-3, was the average grain size. Ag doping was found to increase the average grain size: from an average of 3 μm (Control) to 8 μm (10% Ag doped).

Figure 4-3 (b) confirmed the segregation of Ag in voids in doped specimens. Both SEM and optical images indicated that the Ag had melted and would have permeated YBCO specimens most likely via less resistant paths offered by grain boundaries. Even though sintering was at 950 ^{0}C; the melting temperature of the silver is lowered from 960 ^{0}C due to the oxygen atmosphere of the heat treatment.

4.3 Magnetisation measurements

Data logging and control was achieved by a data acquisition and control board (ACPC 16-16 C90) produced by Strawberry Tree Incorporated[2], which was installed in a computer running Microsoft Windows. The board had an icon-driven graphic user interface with 8 x analogue inputs (16 bit resolution) and 16 x input/output digital lines. Appropriate icon-based computer programs were easily 'built' to interface to hardware for magnetisation and resistance measurements and a PID temperature controller for a cryorefrigerator system.

A vibrating sample magnetometer (VSM) was used to make magnetisation measurements in the temperature range 72.5 K $\leq T \leq T_c$. Isothermal, zero-field-cooled magnetisation measurements were conducted in two regions: low field ($0 \leq H_a \leq 60$ Oe) and high field ($0 \leq H_a \leq 2000$ Oe). The applied field increased monotonically at a rate of 1 Oes^{-1} for low-field measurements and 20 Oes^{-1} for high-field measurements. The field was applied parallel to the long axis of each specimen and was generated by a liquid nitrogen cooled copper solenoid. The Earth's magnetic field in the specimen was estimated at less than 0.2 Oe. Temperature control was achieved with a commercial Lakeshore temperature controller where control was better than ± 0.05 K. The VSM was housed in a liquid helium cryostat. Unfortunately, due to the age of the cryostat, only liquid nitrogen temperatures were obtainable; the coldest temperature of approximately 72.5 K was reached via pumping on the liquid nitrogen. For a comprehensive description of the VSM/cryostat read reference [179].

Raw magnetisation data was displayed in real-time on a monitor and stored to a computer's hard drive to be analysed later. Limited real-time processing of magnetisation data, for example, the derivative of the magnetisation curve, was plotted simultaneously with the magnetisation data, and was used to indicate the shoulder part of the low-field magnetisation ($M - H_a$) curve (see Figure 3-2).

Raw data stored on the computer's hard drive was processed into magnetisation measurements, i.e. data was normalised to the volume of the specimen and adjusted for the demagnetising coefficient, which will be discussed further in Chapter 5.

[2] Now owned by Iotech Incorporated.

4.3.1 Low-field results

A comparison of typical low field adjusted $M - H_a$ data at $T = 72.5$ K for various Ag doped specimens is shown in Figure 4-4.

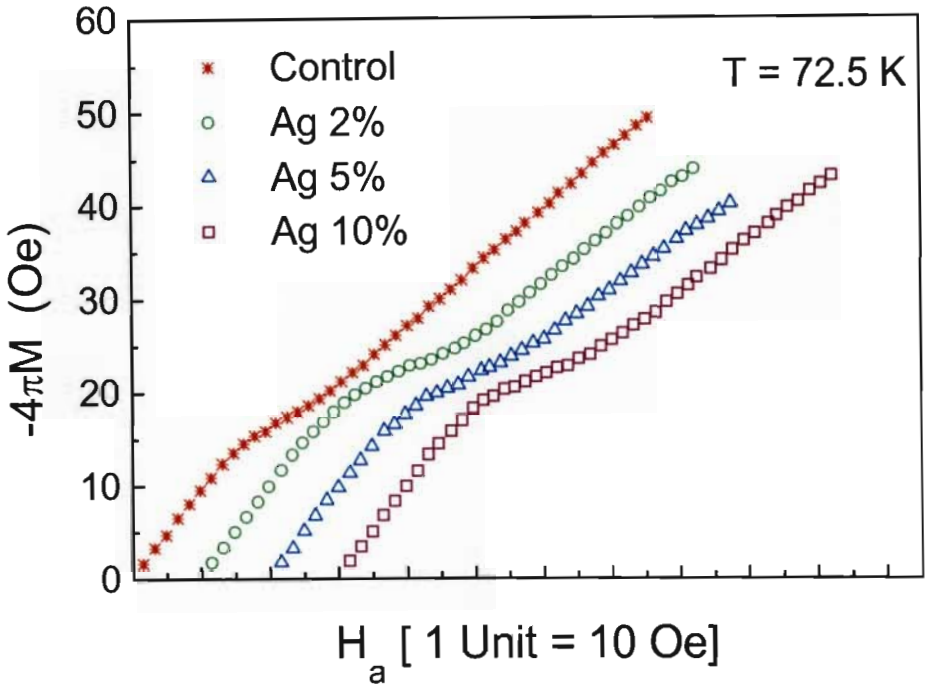

Figure 4-4: Comparison of low-field magnetisation of silver-doped 0%, 2%, 5% and 10% YBCO curves at $T = 72.5$ K. Each specimen's magnetisation response is clearly different. Note that for clarity the origins of the curves has been shifted by 10 Oe.

Key features of a typical low-field HTS curve are: (i) the initial diamagnetic region, where the entire specimen screens out the applied magnetic field, typically up to a few Oersteds for polycrystalline HTSs; (ii) intergranular field penetrate region (shoulder), where field penetrates the intergranular regions; and (iii) the quasi-diamagnetic region with a slope equal to $1 - \mu_{eff}$, where grains or strongly coupled 'clustered' grains screen out the applied field.

Figures 4-5 to 4-8 show low-field magnetisation isothermal curves, in a range $72 \lesssim T \lesssim 91.5$ K, for Ag doping experiments: control, 2% Ag, 5% Ag and 10% Ag respectively (note the black lines in the figures are merely a guide to the eye and are not theoretical fits).

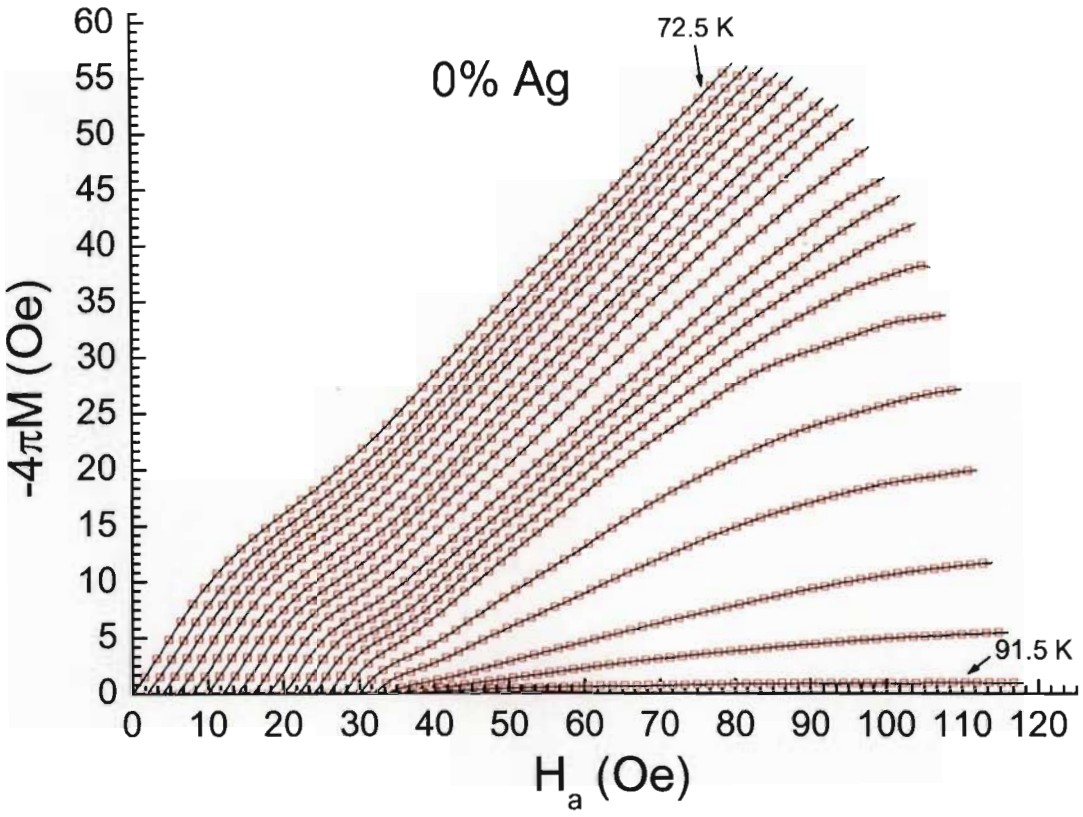

Figure 4-5: Isothermal low-field curves for the control specimen in the temperature range 72.5 K - 91.5 K, in steps of 1 K. Note that the origin of each curve has been shifted by 2 Oe for clarity.

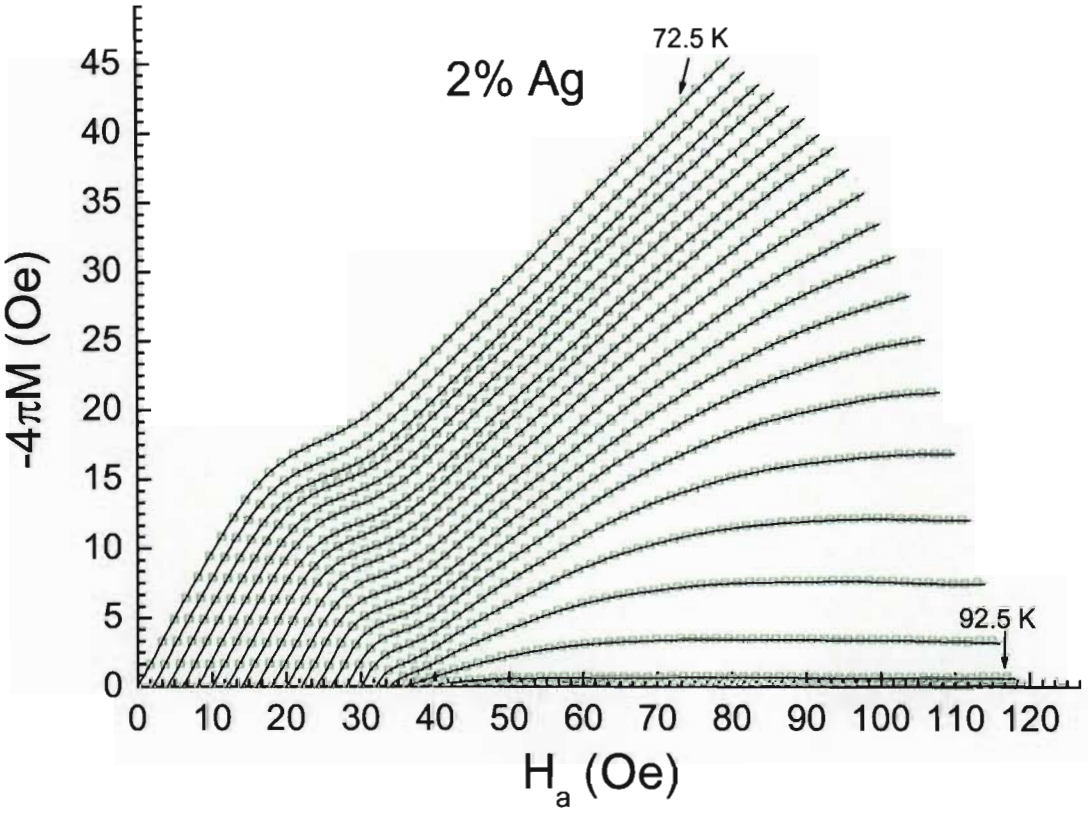

Figure 4-6: Isothermal low-field curves for the 2% Ag specimen in the temperature range 72.5 K - 91.5 K, in steps of 1 K. Note that the origin of each curve has been shifted by 2 Oe for clarity.

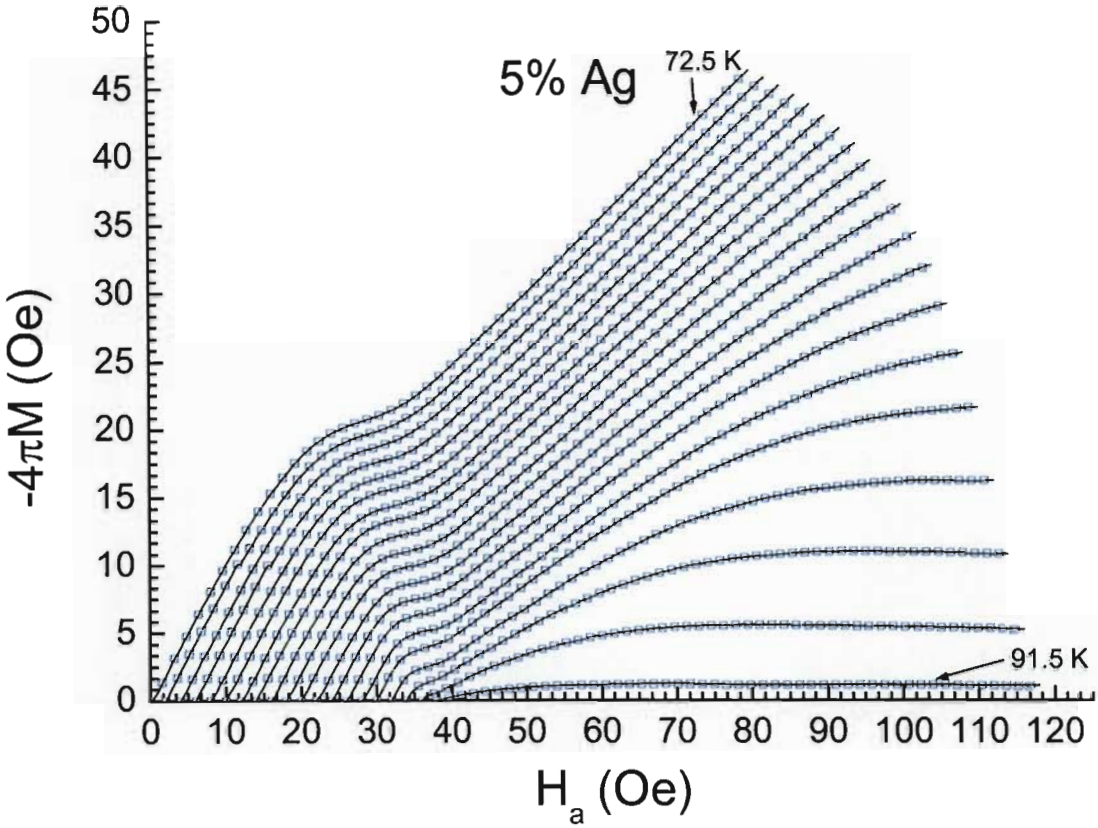

Figure 4-7: Isothermal low-field curves for the 5% Ag specimen in the temperature range 72.5 K - 91.5 K, in steps of 1 K. Note that the origin of each curve has been shifted by 2 Oe for clarity.

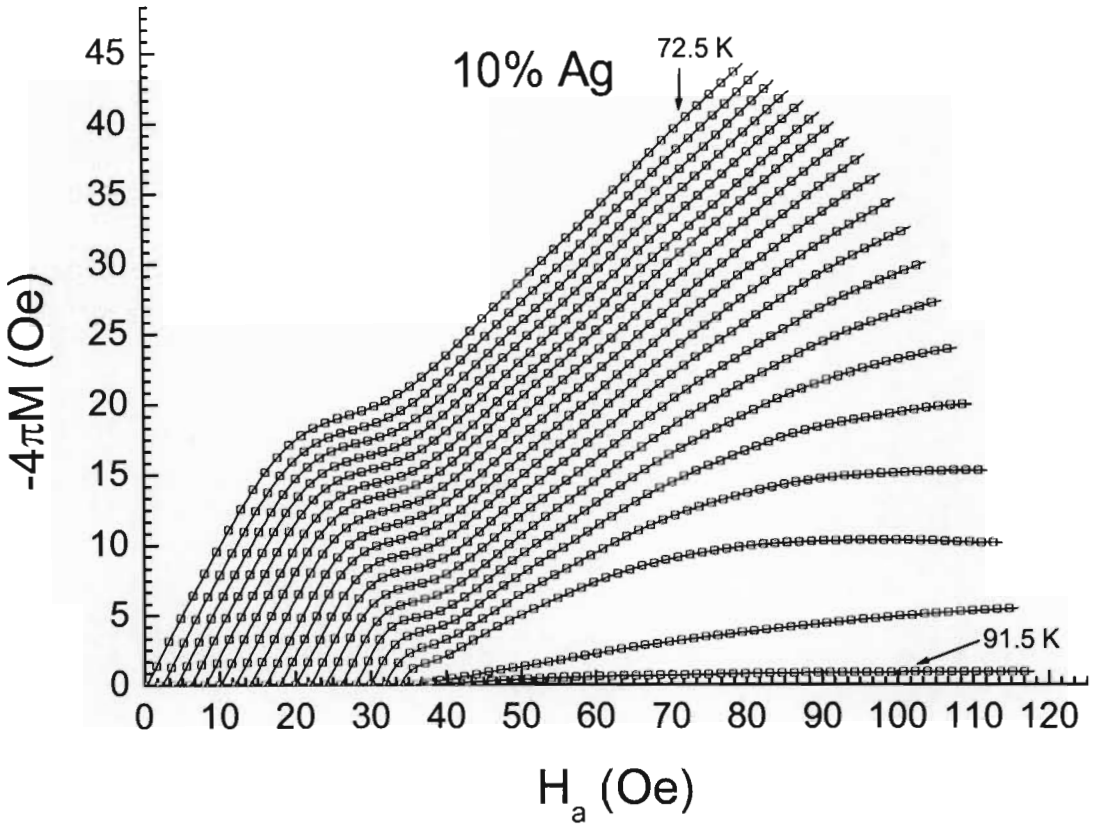

Figure 4-8: Isothermal low-field curves for the 10% Ag specimen in the temperature range 72.5 K - 91.5 K, in steps of 1 K. Note that the origin of each curve has been shifted by 2 Oe for clarity.

4.3.2 High-field results

Figure 4-9 shows a comparison of various Ag doped high-field magnetisation measurements for $T = 72.5$ K. High-field measurements were used to estimate the average granular penetration depth of each specimen (and consequently to estimate an average 'cluster' size for each specimen).

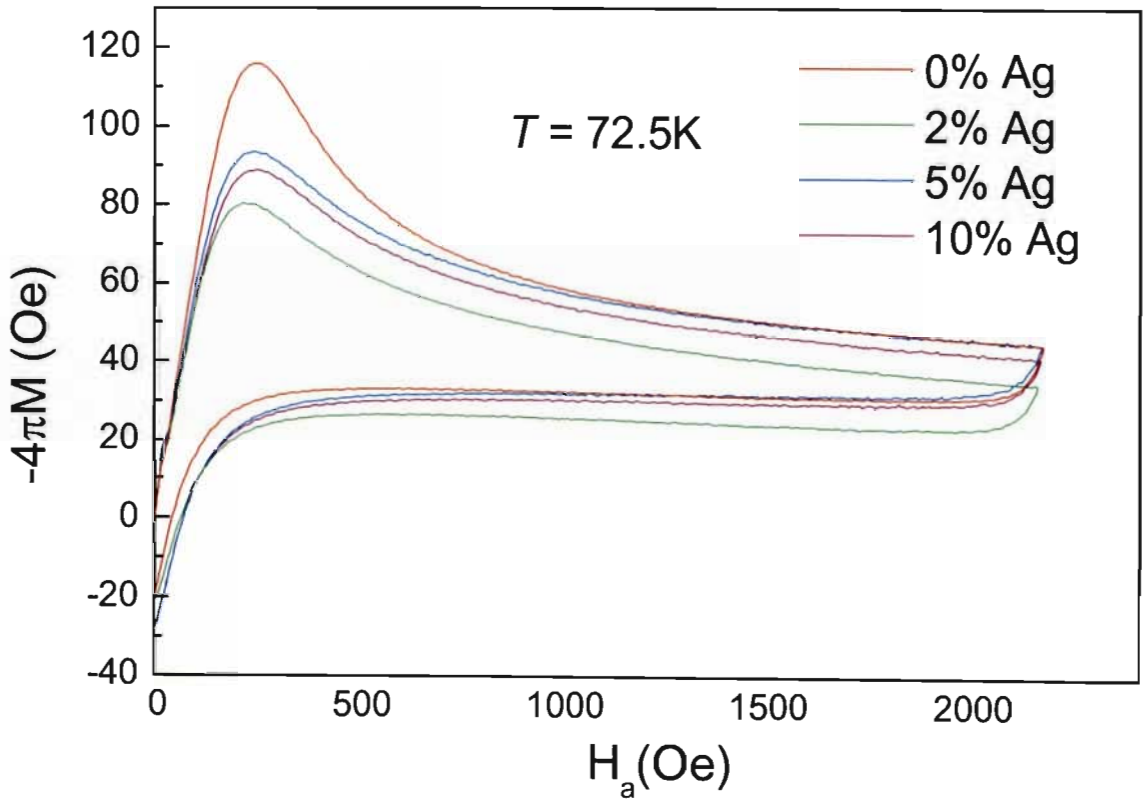

Figure 4-9: Comparison of high-field magnetisation Ag-doped 0%, 2%, 5% and 10% YBCO curves at $T = 72.5$ K.

Key features of a typical curve are: (i) the initial flux penetration at about $H_a \approx 10$ Oe (barely apparent in the curves); (ii) the critical field, H_{c1}(the peak of the curve)[3]; and (iii)

[3]This is not exactly H_{c1}as pinning and surface barrier effects are not accounted for.

trapped flux that remains in the specimen after the field has been cycled back to zero (H_a = 0 Oe). Another feature is the lack of significant increase in flux pinning in the intragranular regions with respect to an increase in Ag doping. This is based on the fact that an increase in intragranular current, due to an increase in intragranular flux pinning, is typically observed when doping type-II superconductors with small quantities of impurities such as Ag which pin flux. The CSM [36], as described in Section 1.4.2, predicts that intragranular current is proportional to the magnetisation width (ΔM). Figure 4-9 shows no such increase in the magnetisation width with doping. The lack of increase in pinning with Ag doping can be considered as additional evidence that Ag concentrates mainly in the intergranular regions.

Figures 4-10 to 4-13 show a selection of high-field magnetisation measurements of the Ag doped specimens in the temperature range 72.5 K - 88.5 K.

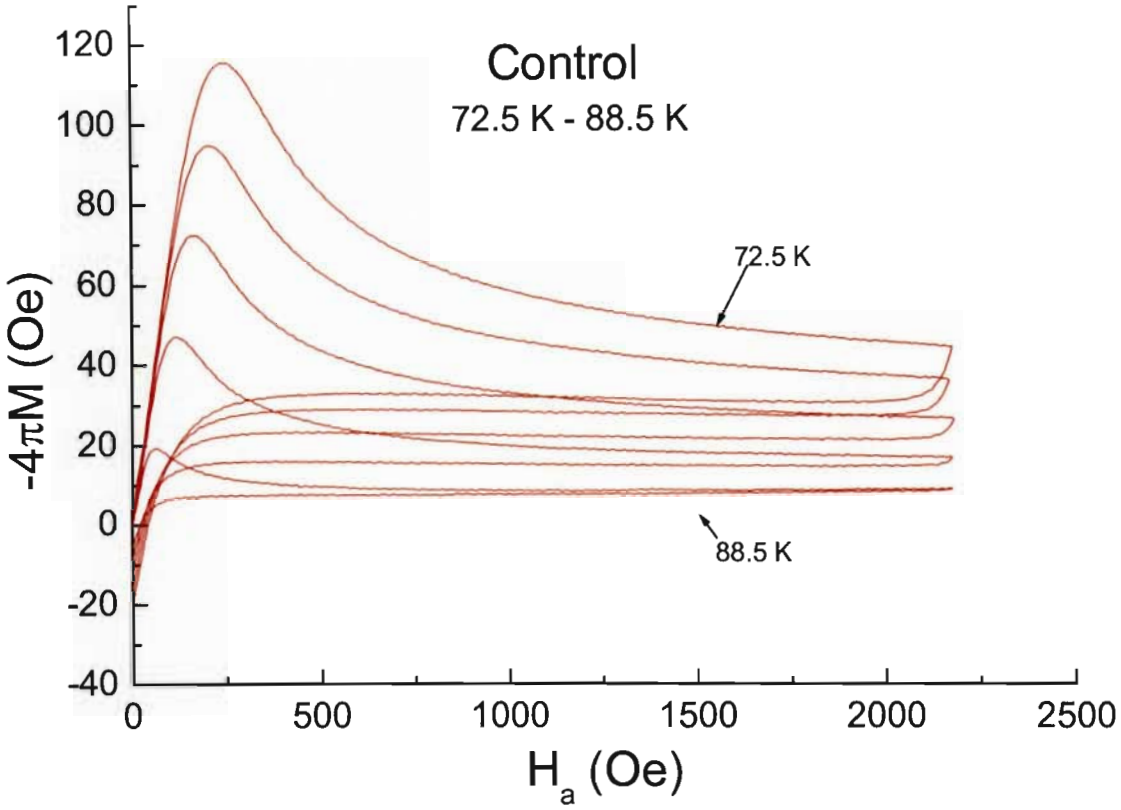

Figure 4-10: Isothermal high-field curves for the control specimen in the temperature range 72.5 K - 88.5 K, in intervals of 4 K.

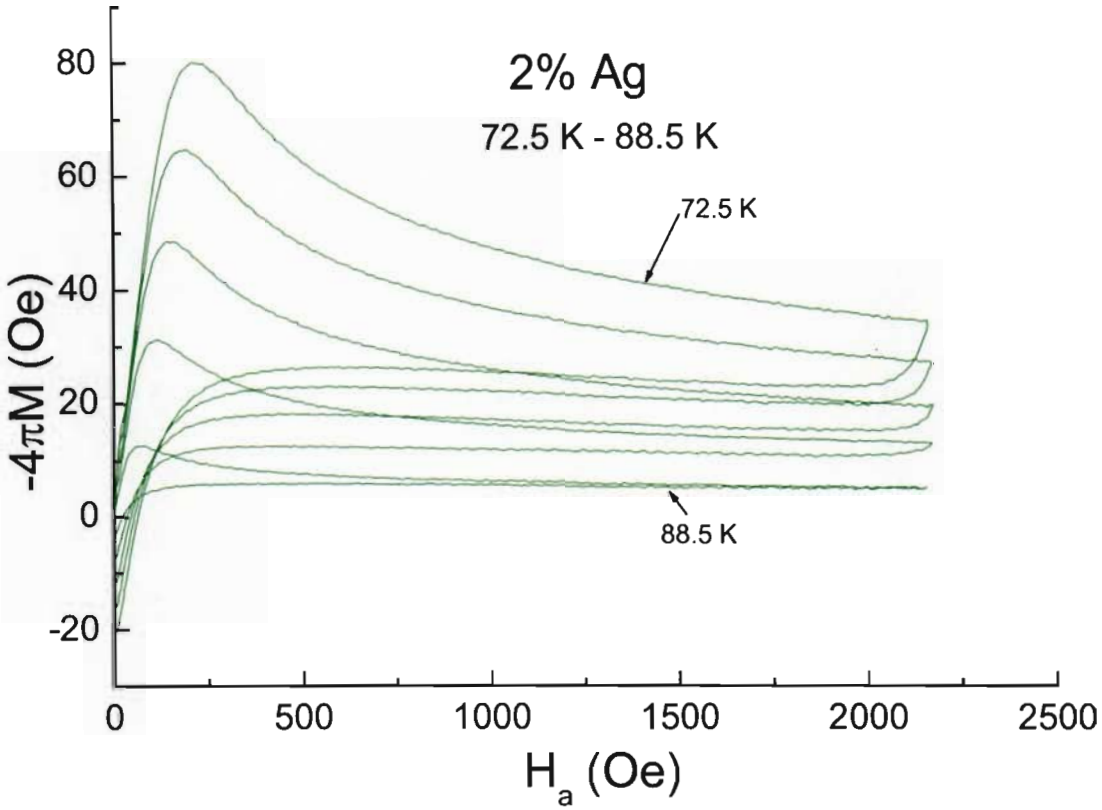

Figure 4-11: Isothermal high-field curves for the 2% Ag specimen in the temperature range 72.5 K - 88.5 K, in intervals of 4 K.

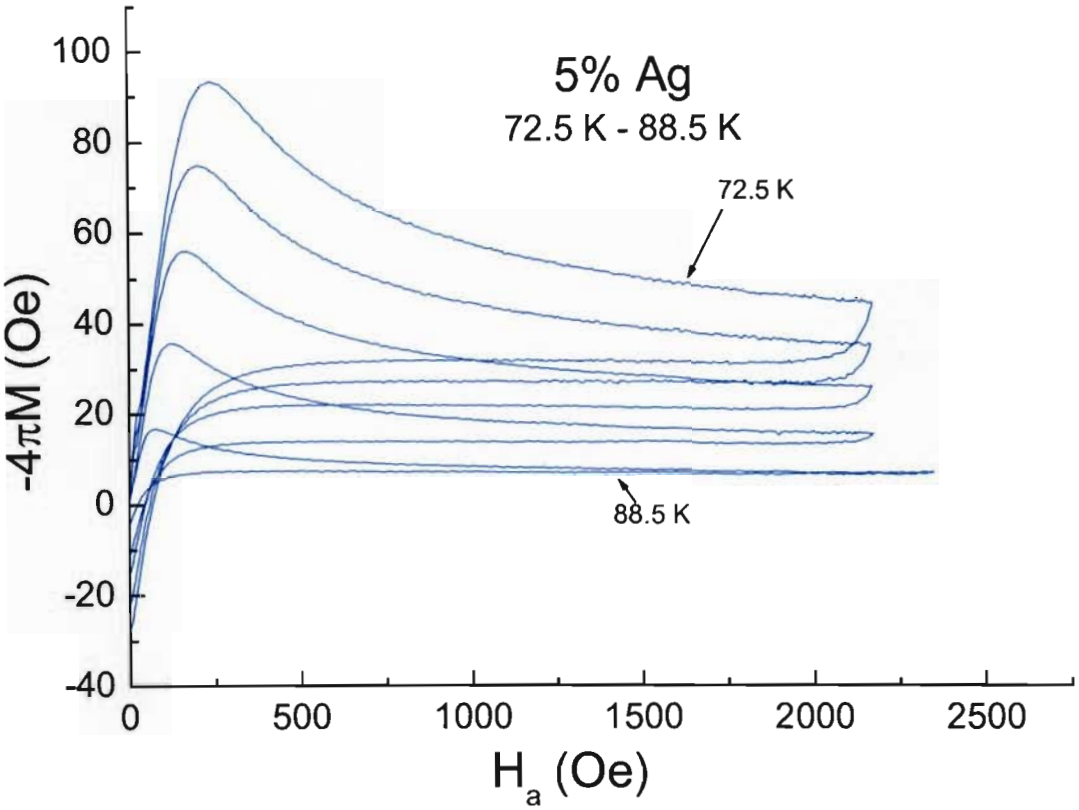

Figure 4-12: Isothermal high-field curves for the 2% Ag specimen in the temperature range 72.5 K - 88.5 K, in intervals of 4 K.

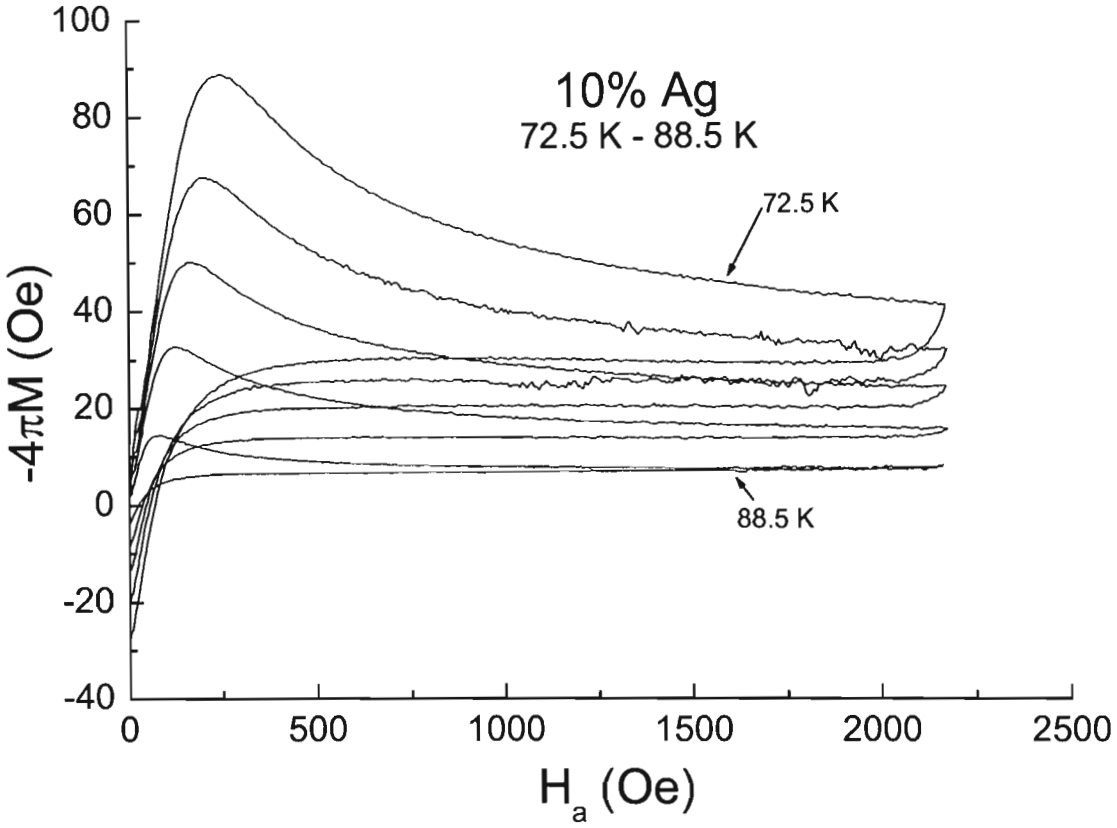

Figure 4-13: Isothermal high-field curves for the 2% Ag specimen in the temperature range 72.5 K - 88.5 K, in intervals of 4 K.

4.4 Resistance measurements

Resistance measurements were made using a GB15 cryogenic refrigerator manufactured by CryoMech Incorporated. A cold-head housed the resistance experiment. Inside the housing a copper cold stage coupled to the experimental stage; here specimens, a thermometer and heater were attached.

A control computer program was written to interface with the refrigerator system. The program (along with peripheral interface electronics) controlled the refrigerator; from simply switching it 'on' and 'off' via the computer keyboard to PID temperature control of the experimental stage, with control better than ± 0.05 ^{o}C.

A feature of the control program was the monitoring of the output power of the heater mounted on the experimental stage. This feature was useful in protecting the heater from over stressing and burning out. The control program switched the refrigerator 'off' when the heater was 100% 'on'. The refrigerator was re-switched 'on' when the heater power measured 50%. The heater was constructed out of constantan wire (diameter equal to 0.5 mm).

A Lakeshore Inc. platinum thermometer (Resistance Temperature Device PT-111) was fitted to measure the temperature of the experimental stage. The control program determined the resistance of the thermometer via the standard '4-wire' method. To avoid Joule heating of the thermometer a current of 100 μA was used. The thermometer had resistance versus temperature calibration tables from 325 K to 14 K, which were programmed into the control program.

Resistance measurements of specimens were achieved by the standard '4-wire' resistance method where the current was controllable from $\pm$ 5 μA to $\pm$10 mA. The current was kept as small as possible as Joule heating could affect resistance measurements, especially at the contacts.

It was found that the best contacts onto the specimens were made by gold sputtering onto the specimen followed by a small blob of silver paste (SPI®). Silver wire was secured to each contact. A 10 minute curing process in an oxygen atmosphere at 350 ^{o}C was used. The specimen was then mounted onto the experimental stage in the refrigerator with a little vacuum grease.

To achieve accurate resistance measurements a 1 Hz bipolar signal generator (quasi-DC) was used as a current source. This helped in decreasing the effects of contact resistance. With this

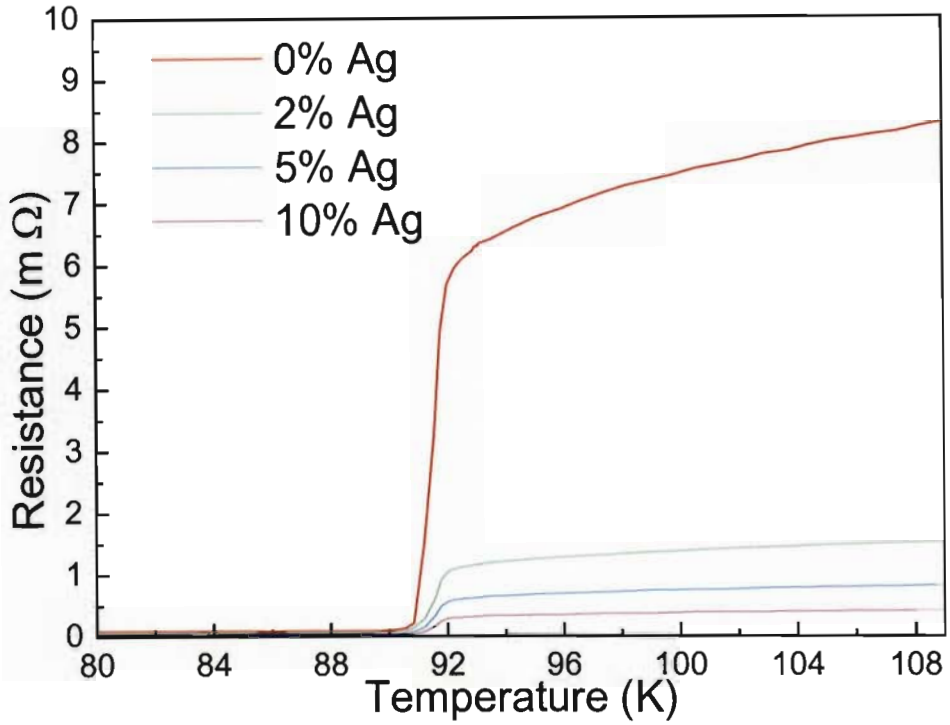

Figure 4-14: Resistance measurements of Ag-doped YBCO specimens.

setup the voltage across the specimen in one direction would be added to the voltage drop in the opposite direction and then averaged, resulting in a single data point. A software low-pass filter, effectively filtering out mains 50 Hz noise, was also configured in order to give a better signal to noise ratio.

Both sets of 4-wire resistance measurement leads (thermometer and specimen) including the leads that connected the heater, were wrapped around the cold stage of the refrigerator in order to thermally anchor the experimental stage from heat conducted from the laboratory into the experiment.

Figure 4-14 shows resistance versus temperature curves of the Ag-experiment. The significant effect was the lowering of the normal resistance for the silver doped specimens. This can be attributed to better conducting silver compared to room temperature YBCO and bigger grains (fewer resistive grain boundaries). The critical temperatures T_c of all specimens were within 1 K of each other, at about 92 K.

Chapter 5

Results and discussion

Central to this study is the effect of Ag doping on intergranular properties of YBCO. The critical state model (CSM), represented by Equations 3.16 and 3.17, was fitted to isothermal zero-field-cooled low-field magnetisation measurements using characteristic temperature dependent variables as free fitting parameters. After the fitting, the temperature dependencies of each parameter was analysed using appropriate models in order to determine the effects of Ag doping.

Before analysing the temperature dependence of each fitting parameter, an average (effective) 'cluster' size needed to be determined. This was achieved by considering the average granular penetration depth $\overline{\lambda_g}(T)$ of each specimen obtained from isothermal zero-field-cooled high-field magnetisation measurements. The resulting penetration depths were used in the fitting of the CSM effective permeability fitting parameter $\mu_{eff}(T)$, from which a measure of the average 'cluster' size resulted. The derived effective 'cluster' size was then used in fitting CSM temperature dependent variables $J_{c0}(T)$ and $H_0(T)$ and δ to appropriate models. Finally, the results of all model fits, experimentation and the influence of Ag doping on the YBCO system is discussed.

5.1 High-field regime

In previous intergranular CSM analyses [156, 160] both the Gorter-Casimir two-fluid and BCS models for temperature dependence of the penetration depth were used to generate data for $\overline{\lambda_g}(T)$. The penetration depth had no 'link' with experimental measurement specific to each

specimen, i.e. values were not derived from measurements but rather from models.

In the present work the technique suggested by Kogan [169] has been adopted to derive values for $\overline{\lambda_g}(T)$ from the reversible part of magnetisation $M_{rev}(H_a)$ in the intermediate-field domain $H_{c1g} << H_a << H_{c2g}$.

5.1.1 Determination of average granular penetration depth, $\overline{\lambda_g}(T)$

In Section 3.5 it was shown that the average granular penetration depth $\overline{\lambda_g}(T)$ can be determined from the a plot of reversible magnetisation M_{eq} versus the logarithm of the applied field $\ln(H_a)$ by use of the following relationship:

$$\frac{dM_{eq}}{d\ln(H_a)} = \frac{\Phi_0}{64\pi^2\overline{\lambda_g}^2}.g(\zeta). \tag{5.1}$$

Here Φ_0 is the flux quantum and $g(\zeta)$ is a correction factor that depends on a superconductor anisotropy factor $\zeta \equiv \frac{\lambda_c}{\lambda_{ab}}$.

Using high-field measurements, such as those shown in Figure 4-10 to 4-13, an estimate of the M_{eq} component for each isotherm was determined by using the following relationship $M_{eq}(H) = (M^- - M^+)/2$, where $M^-(M^+)$ is the magnetisation measured in decreasing (increasing) field, respectively, as illustrated in Figure 1-6.

Figure 5-1 shows typical plots of M_{eq}versus $\ln(H_a)$ for the YBCO (5 % Ag) specimen as extracted from the high-field measurements shown in Figure 4-12. As predicted by the Kogan theory M_{eq} is, within experimental error, linear in the logarithmic of applied field H_a for all measurement taken[1].

In order to fit Equation 5.1 to the above isotherms, $\overline{\lambda_g}$ was used as fitting parameter with the correction factor $g(\zeta) = 3.2$ (see Section 3.5). The above procedure was repeated for the other Ag doped specimens, where the resulting fitting parameter $\overline{\lambda_g}(t)$ of each isotherm is plotted in Figure 5-2. The figure includes the BCS prediction for the penetration length, which is discussed in the next section, along with an explanation of the scatter that occurs close to T_c.

[1] Demagnetisation effects can be ignored here, unlike in low-field measurements (Section 5.2) where they are more predominant.

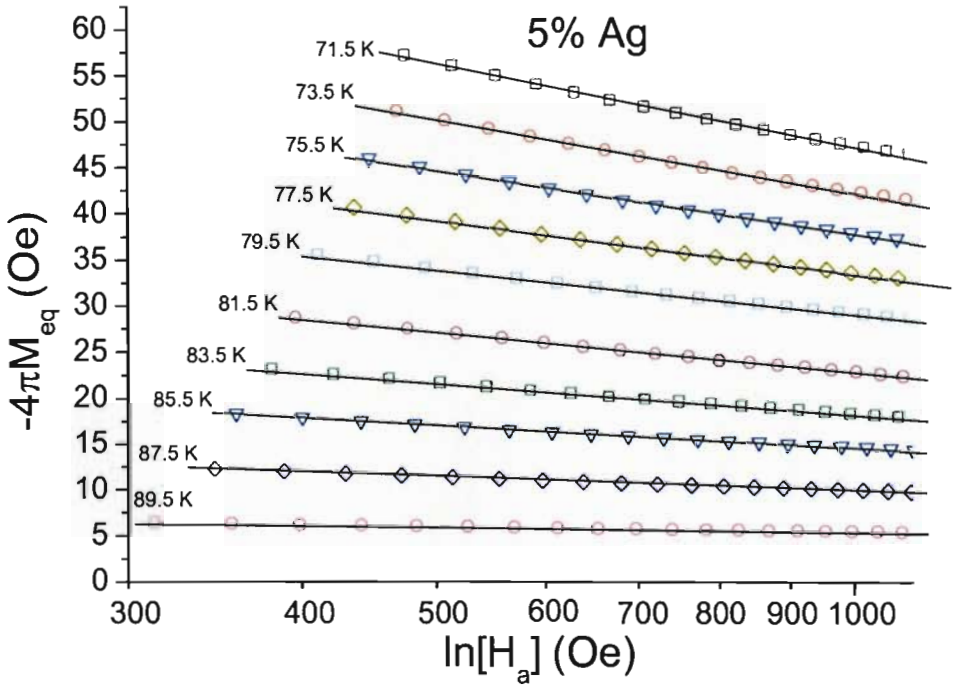

Figure 5-1: Plots of -$4\pi M_{eq}$ versus $\ln H_a$ at various temperatures for 5% Ag YBCO specimen.

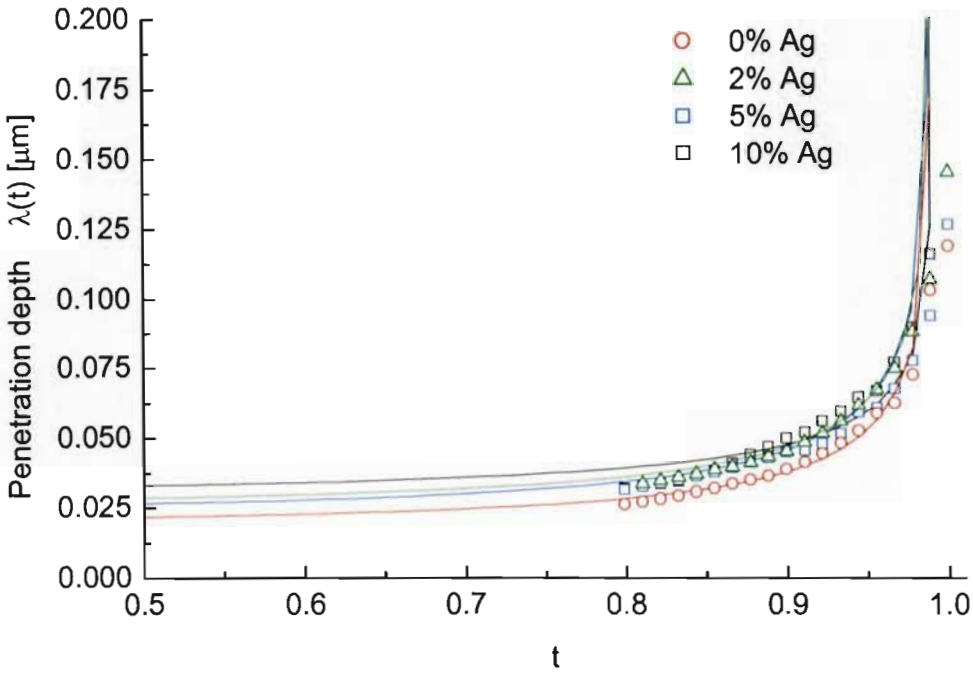

Figure 5-2: Average granular penetration depth $\overline{\lambda_g}$ and theoretical BCS fits versus reduced temperature $t{=}T/T_{c,m}$ for the Ag-doping experiment.

Table 5.1: Predicted T_c based on the logarithmic slope $dM_{eq}/dln(H_a)$ and theoretical fitting parameters, λ_0 and n.

Specimen	0% Ag	2% Ag	5% Ag	10% Ag
$T_{c,m}$ (K)	89.5 ±0.1	90.1 ±0.1	90.6 ±0.1	89.2 ±0.1
$\lambda_0(\mu m)$	0.211 ±0.001	0.279 ±0.001	0.259 ±0.001	0.324 ±0.001
n	-0.56 ±0.01	-0.50 ±0.01	-0.54 ±0.01	-0.37 ±0.01

Determination of critical temperature, $T_{c,m}$

In order to fit the BCS theoretical penetration depth expression, Equation 1.52, to the above penetration depth data (as shown in Figure 5-2) the critical temperature needed to be determined. The critical transition temperature for each Ag doped YBCO specimen was determined from reversible/equilibrium magnetisation derivative plots, shown in Figure 5-1. The reasoning is based on the GL relationships of Equations 1.36, 1.35 and 1.32, for which the following relationships holds near T_c:

$$\frac{1}{\lambda^2} \propto T - T_c \propto n_s. \tag{5.2}$$

The above relationships, combined with Kogan's penetration depth Equation 5.1, where $dM_{eq}/d\ln(H) \propto 1/\lambda^2$, implies that when $dM_{eq}/d\ln(H) = 0$, $n_s = 0$, which defines the 'magnetic' critical transition temperature $T_{c,m}$.

Figure 5-3 shows a plot of the magnetisation derivative, $dM_{eq}/d\ln(H)$ versus temperature for the Ag doping YBCO experiment, where extrapolation of the linear fits is used to yield the critical transition temperatures $T_{c,m}$ for each Ag doped YBCO specimen. The resulting values of $T_{c,m}$ were used for the fitting of theoretical curves to $\overline{\lambda_g}$ data in Figure 5-2.

The critical temperatures $T_{c,m}$ obtained from the above penetration depth analysis for Ag doped specimens are tabulated in Table 5-1. The results were similar to those obtained from resistance measurements; namely, the 5% Ag specimen has the highest T_c with the 10% Ag specimen having the lowest.

Once $T_{c,m}$ values were obtained for each specimen, an assumption of strong BCS coupling, namely, $\beta_c = 5.5$ (energy gap $2\Delta = 5.5kT_c$), was assumed to fit theory to experimentally determined values of $\overline{\lambda_g}(T)$. Most HTS experiments suggest $4 \leq \beta_c \leq 7$ [180 - 182].

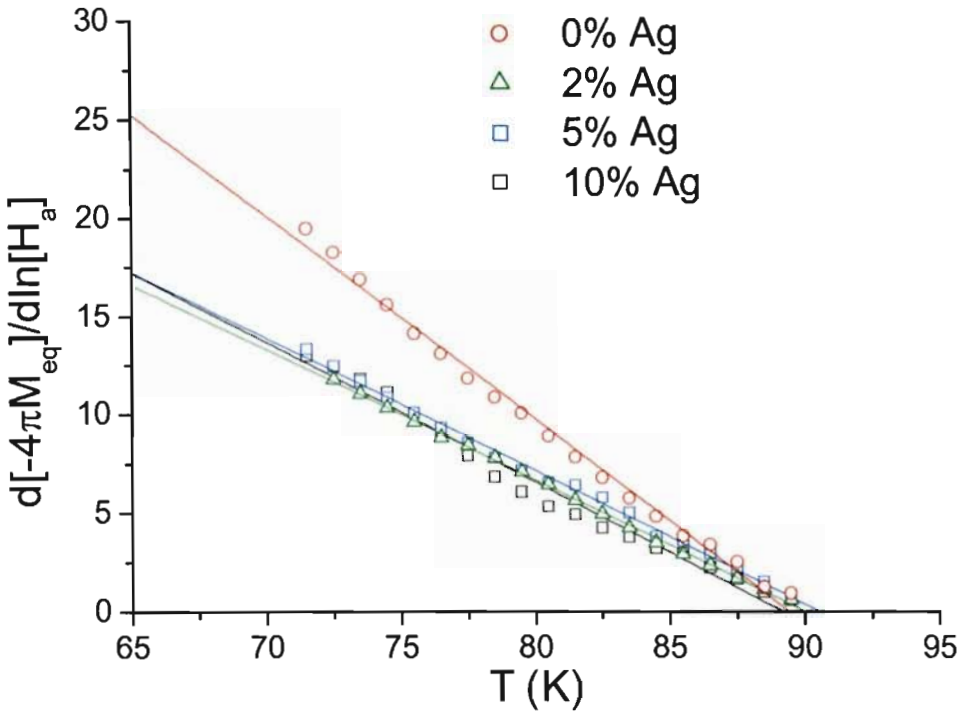

Figure 5-3: Equilibrium magnetisation derivative, $dM_{eq}/d\ln(H)$ versus t, for various Ag-doped YBCO specimens. The intercepts define $T_{c,m}$.

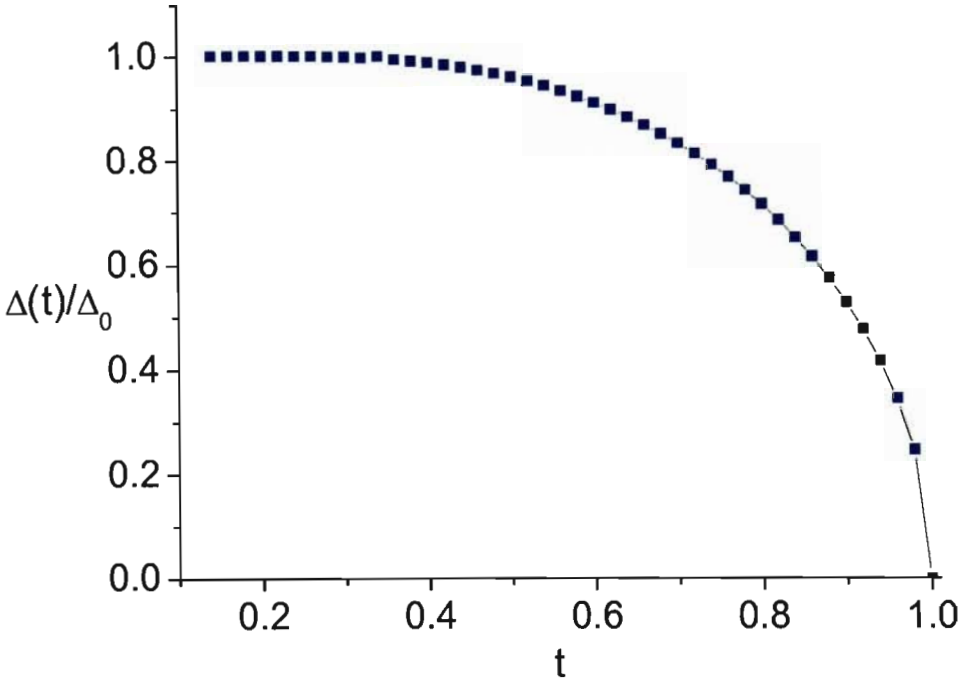

Figure 5-4: A plot of Muhlschlegel's tabulated values for the reduced gap parameter, $\Delta(t)/\Delta(0)$.

The temperature dependence of penetration depth, discussed in the summary of the BCS theory in Section 1.3.5 and represented specifically in Equation 1.52, namely,

$$\lambda(t) = \lambda_0 \left[\frac{\Delta(t)}{\Delta_0} \tanh\left(\frac{\beta_c}{4t} \frac{\Delta(t)}{\Delta_0} \right) \right]^n , \tag{5.3}$$

was fitted to the $\overline{\lambda_g}(t)$ data. The $\overline{\lambda_g}(t)$ fits are plotted in Figure 5-2 where λ_0 and n were used as fitting parameters. Here n is related to the ratio of mean free path and coherence length and λ_0 is the magnetic penetration depth at $T = 0$ K. Interpolated values for the reduced gap parameter, $\Delta(t)/\Delta(0)$ were obtained from Muhlschlegel's tabulated values [34], which is shown in Figure 5-4. The large gradient observed in $\Delta(t)/\Delta(0)$ for $0.98 < t < 1$ accounts for the rapid change of the $\overline{\lambda_g}$ fits for the corresponding temperature range.

Values for fitting parameters λ_0 and n are tabulated in Table 5-1 for various Ag doped specimens. The penetration depth was assumed to be an average granular value for the ab-

and c-directions, and the results are consistent with other values obtained elsewhere [183, 184, 170].

The values for λ_0 increase by approximately 50% with an increase in Ag doping from 0-10%. This observation is similar to that of Pippard for a Sn doping experiment (and other similar doping experiments) [25, 185, 186], where the penetration depth increased by a factor of two when doped with 3% indium.

The values of n for the Ag doped specimens fall into roughly two limits - 'dirty' with $n = -1/2$ (0%, 2% and 5% Ag doped specimens) and 'clean' with $n = -1/3$ for the 10% specimen. A possible explanation for this change in limit type with Ag doping is that n is sensitive to the density of physical defects and foreign atoms through its mean free path association. This then suggests that the 10% specimen's grains may have a reduced density of physical defects. The association of reduced defects with Ag doping has been identified via direct morphological measurements [18, 188] but not from penetration depth analysis as done above.

5.2 Low-field regime - critical state model fitting

The entire fitting procedure of the intergranular critical-state model (CSM), represented by Equations 3.16 and 3.17, including demagnetisation corrections was accomplish by means of a computer algorithm, which uses a weighted least-square procedure. Figure 5-5 shows a typical fit (sold line) to $M - H_a$ data (open squares). The weighting procedure forces good fits to the shoulder region - the region of intergranular flux penetration.

The fitting procedure corrects for demagnetisation effects as follows: specimens (11 x 2 x 2 mm) were approximated by an ellipsoid and a linear correction for the demagnetising field was achieved by use of the relation $H_i = H_a \left[1 - D_m(1 - \mu_{eff})\right] - 4\pi M D_m$, where H_i is the mean internal field, D_m is the demagnetisation factor along the long axis and μ_{eff} is a field-dependent effective permeability. The demagnetisation factor was determined by interpolation of tabulated data [190] and for the present case it is $D_m = 0.0774$.

The field dependence of $\mu_{eff} = 1 + \chi$, where $\chi \equiv \frac{dM}{dH}$ is the susceptibility, results from adjusting its value between field boundaries H_1 and H_2, which define the shoulder region of the

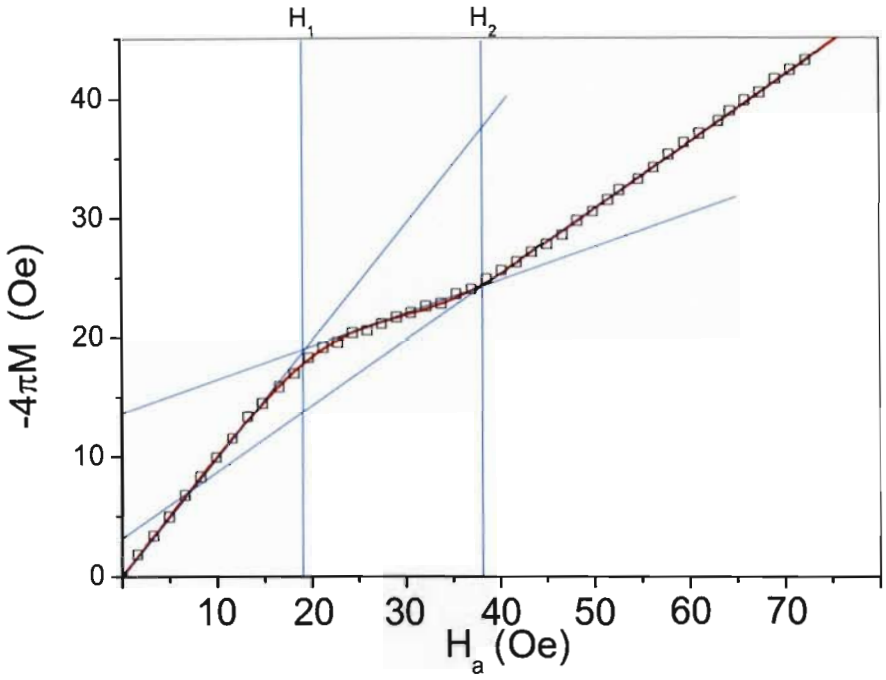

Figure 5-5: Typical intergranular critical state model fit (red solid line) to $M - H_a$ data (open squares). H_1 and H_2 define the shoulder region and the three regimes of χ.

$M(H)$ curve, as shown in Figure 5-5. The algorithm sets $\chi = -1$ for $H_a < H_1$, $\chi = \mu_{eff} - 1$ for $H_a > H_2$ and linearly interpolates values between -1 and $\mu_{eff} - 1$ for the range $H_1 < H_a < H_2$. The algorithm assumes a value μ_{eff} derived from a fit to uncorrected experimental $M - H_a$ data at each temperature. It then iterates to a final value for μ_{eff} when fitting within a specified error. Thus values for all four CSM temperature-dependent fitting parameters, J_{c0}, δ, H_0 and μ_{eff}, are obtained for each $M(H)$ isotherm.

The fitting procedure requires, and is sensitive to, all four parameters. Consider the curve in Figure 5-5: here (i) the quasi-diamagnetic slope is determined by μ_{eff}; (ii) the position and shape of the shoulder region is determined by H_0 and J_{c0}; and (iii) extrapolation of the quasi-diamagnetic linear region back to $H_a = 0$ yields a nonzero residual diamagnetic magnetisation, which is a measure of the field-independent current density component, J_{c1}.

The fits of the CSM algorithm to experimental $M - H_a$ data for all specimens and at all temperatures are accurate to within a small experimental scatter as illustrated in Figures 5-6 to 5-9 for the control, 2% Ag, 5% Ag and 10% Ag specimen respectively.

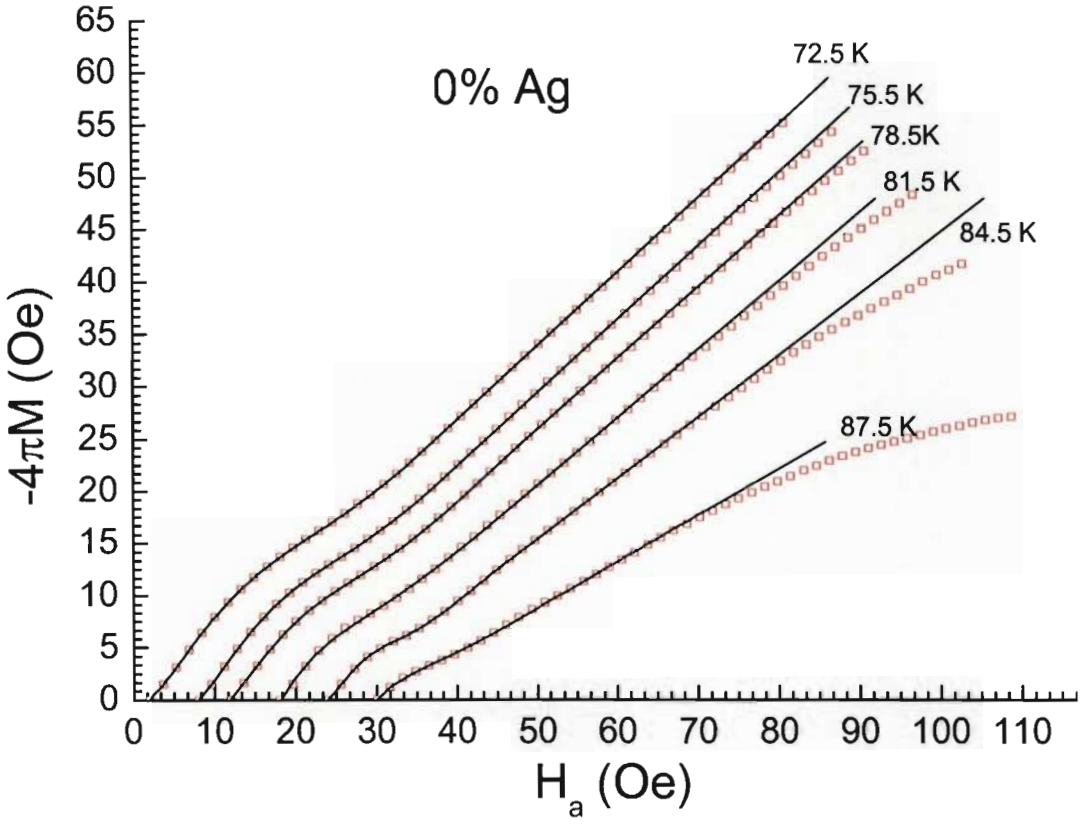

Figure 5-6: A few representative critical-state model fits (solid curves) to experimental $M - H_a$ data (open squares) for 0% Ag doped specimen. Note that the origin of each curve is shifted for clarity.

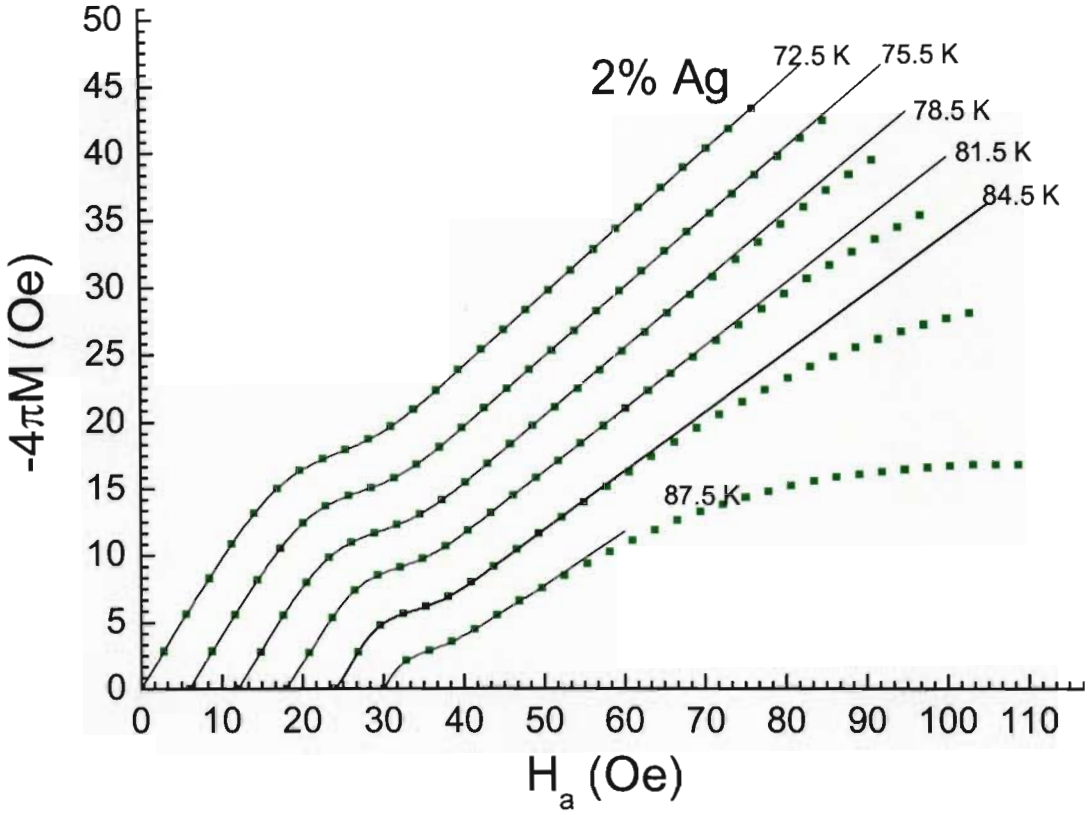

Figure 5-7: A few representative critical-state model fits (solid curves) to experimental $M - H_a$ data (open squares) for 2% Ag doped specimen. Note that the origin of each curve is shifted for clarity.

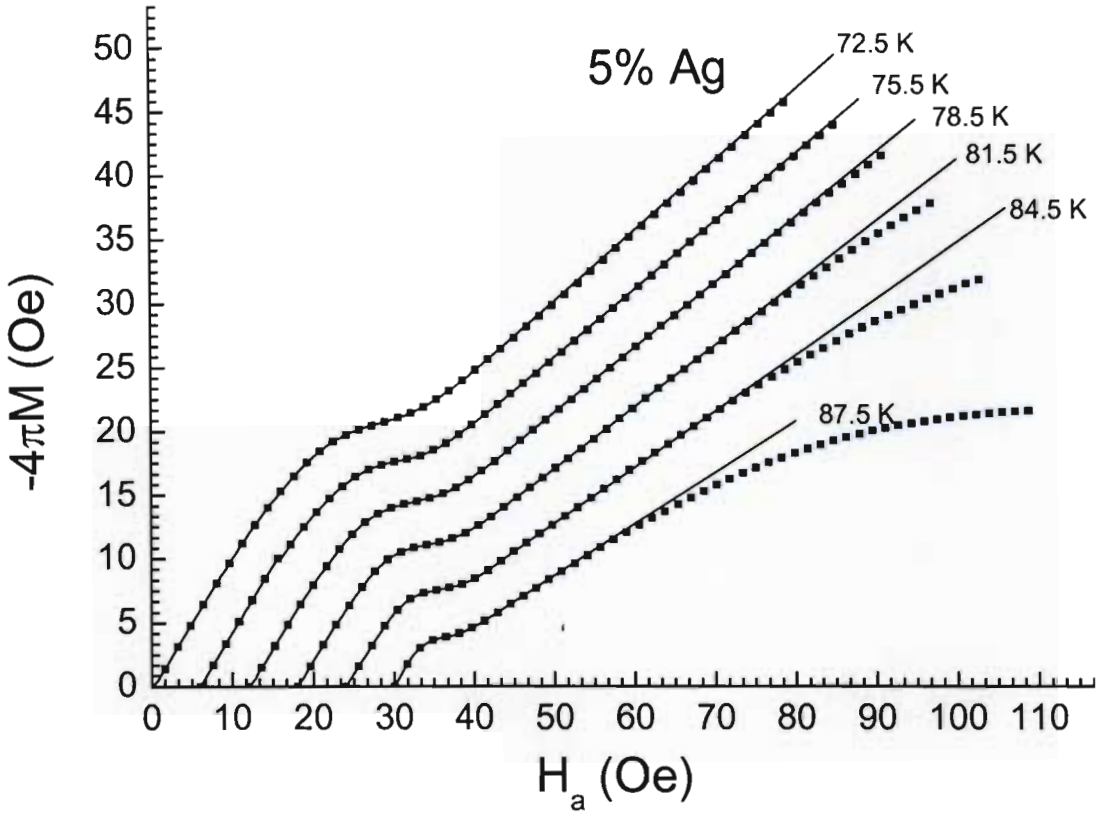

Figure 5-8: A few representative critical-state model fits (solid curves) to experimental $M - H_a$ data (open squares) for 5% Ag doped specimen. Note that the origin of each curve is shifted for clarity.

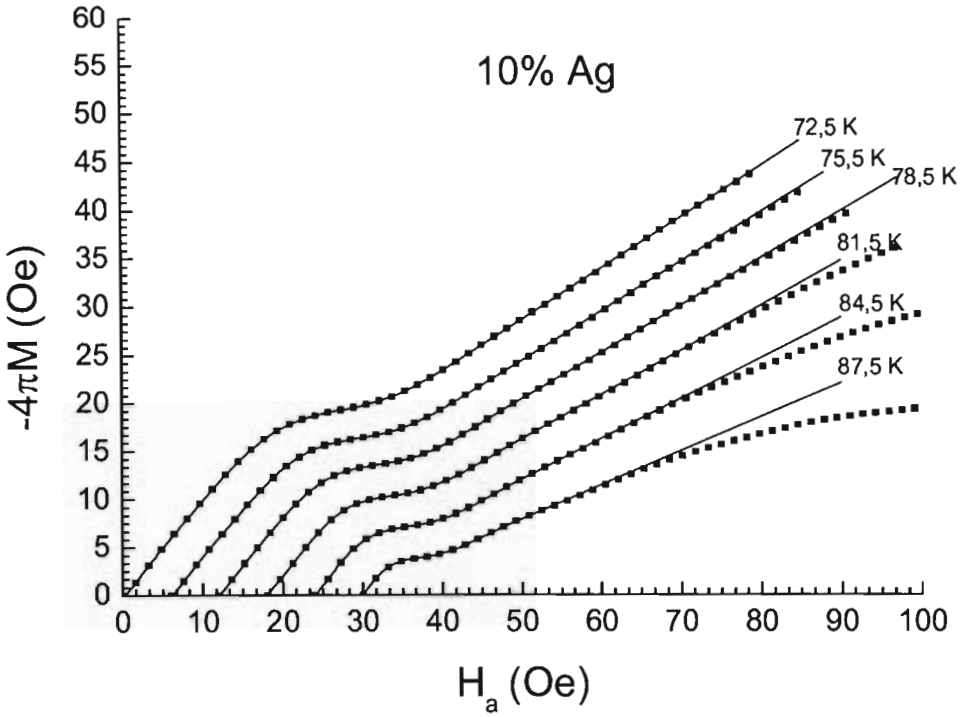

Figure 5-9: A few representative critical-state model fits (solid curves) to experimental $M - H_a$ data (open squares) for 10% Ag doped specimen. Note that the origin of each curve is shifted for clarity.

5.2.1 Temperature dependence of characteristic CSM parameters

Once the fitting procedure of the CSM to $M - H_a$ data was completed for all specimens, the temperature variations of the four CSM characteristic fitting parameters were compared with theory and appropriate model predictions. These latter fits yield, *inter alia*, values for various characteristic lengths of the average grain boundary Josephson junction (GBJ) and these will now be individually discussed.

Effective permeability, $\mu_{eff}(t)$

In the columnar grain model (Section 3.2), the effective permeability μ_{eff} of Equation 3.2 accounts for partial screening of intragranular material and for a non-superconducting volume fraction in the material. The $\overline{\lambda_g}(t)$ data, derived from the analysis discussed in Section 5.1 and

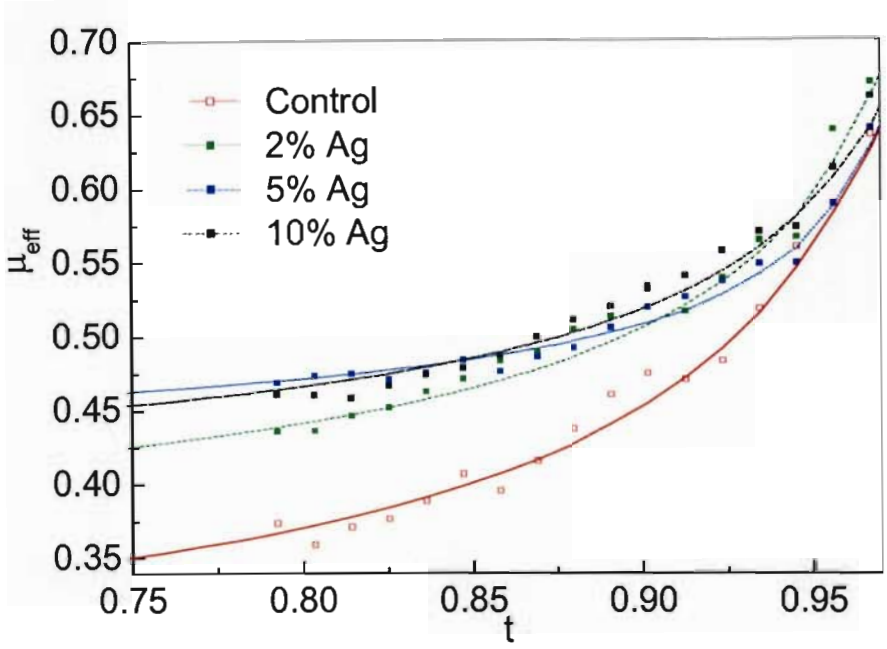

Figure 5-10: Effective permeability μ_{eff} as a function of reduced temperature $t = T/T_c$, for the various Ag-doped specimens. The μ_{eff} data are shown as symbols as described by the legend. The curves are derived from the columnar grain approximation model, Equation (3.2) with $\overline{\lambda_g}(t)$ data derived from Kogan high field analysis.

plotted for each Ag specimen in Figure 5-2, was used to fit the columnar grain model to $\mu_{eff} - t$ data, where $t = T/T_c$ is the reduced temperature. The fitting parameters used were the average grain size a_o and normal volume fraction f_n. Each parameter has different resulting values for the different Ag doped specimens in the temperature range 72.5 K to T_c. Fits to the $\mu_{eff} - t$ data of Equation 3.2 are shown in Figure 5-10 and the effective permeability at $t = 0$ and the fitting parameters are summarised in Table 5-2.

The resulting values for average grain size (or, more strictly speaking in this study, the average superconducting cluster size) a_o are used for other characteristic CSM parameter fits,

Table 5.2: Free fitting parameters a_0 and f_n for each specimen and values of the effective permeability at $T = 0$ K.

Specimen	0% Ag	2% Ag	5% Ag	10% Ag
$\mu_{eff}(0)$	0.27(7)	0.36(5)	0.43(3)	0.40(2)
$a_0(\mu m)$	3.94(4)	5.15(0)	9.07(4)	6.37(2)
f_n	0.06(5)	0.20(4)	0.34(3)	0.28(9)

i.e. $H_0 - t$ and $J_{c0} - t$ data. Predicted values of a_o for the Ag doped specimens are of the same order of magnitude as those measured from polarised optical micrographs. The results summarised in Table 5-2 show that the addition of Ag in the range 2% - 10% seems to enhance grain growth. The presence of silver in grain boundaries may be the reason for the increase in a_o, where it acts as a 'flux' during grain growth. The idea of Ag acting as a fluxing agent is supported by research done into the peritectic temperature of Ag/YBCO mixtures, which is up to 40^0C below that of YBCO's peritectic temperature [191]. The decrease in a_o for the 10% Ag specimen indicates a limit for the extent of Ag doping which gives a maximum of the average grain size.

The normal volume fraction f_n increased with Ag doping, since Ag contributes directly to f_n as it does not superconduct. A decrease in f_n with Ag doping resulted in the 10% Ag specimen, and may be due to residue Ag which migrated to the surface of the specimen.

Average Josephson-junction characteristic field, $H_0(t)$

The behaviour of the characteristic field, $H_0 - t$ for the various Ag doped specimens is shown in Figure 5-11, where it is compared with the prediction of Equation 3.20 discussed in Section 3.4.3. $H_0(t)$ is the characteristic magnetic field for the decay of $J_c(H)$ (Equation 3.13). [It is not only intergranular magnetic penetration though H_0 that is of interest but, more importantly from a large-scale application point of view, the 'height' of the plateau region, discussed in Section 3.2.1. The higher the plateau the higher the critical current density in a large magnetic field.]

In the fitting procedure the effective junction barrier d and geometrical/morphological constant η were treated as fitting parameters, and together with the results from previous fits, $\mu_e(t)$

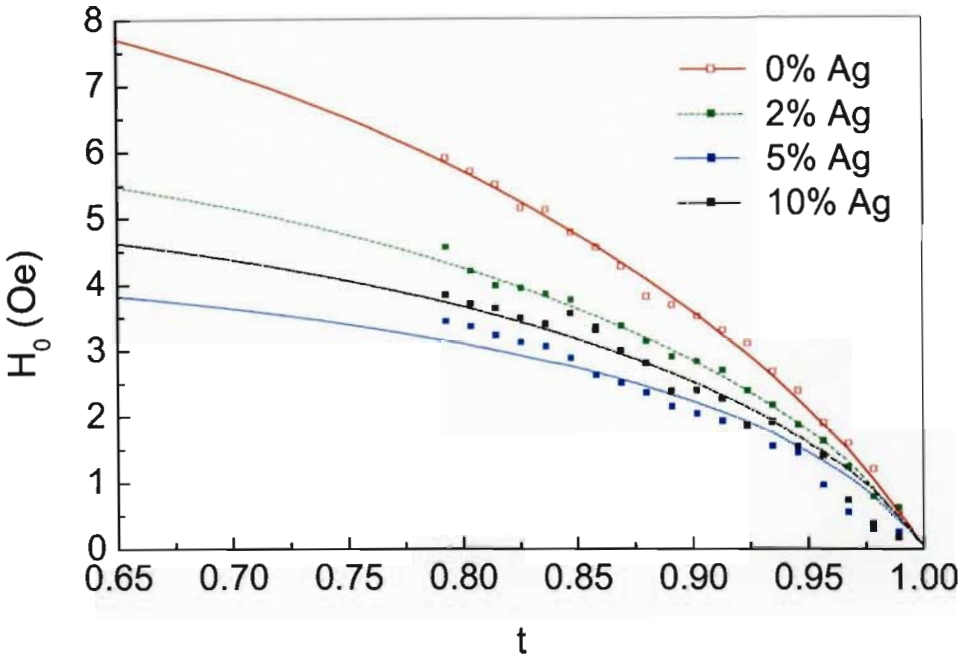

Figure 5-11: Characteristic field theoretical fits (curves) to $H_0 - t$ Ag-doped YBCO data (symbols).

and $\lambda_g(t)$, were used to fit Equation 3.20 to $H_0 - t$ data. The results of the fitting procedure are tabulated in Table 5-3 for each specimen.

A characteristic of Equation 3.20 is that $H_0(t)$ is inversely proportional to grain size, a_o. This relationship is evident in the behaviour of $H_0 - t$; where the 5% Ag doped specimen have the largest grain size and the control specimen the smallest.

The values obtained for the effective junction-barrier width d are orders of magnitude smaller than the average grain size for each specimen and is within the sub-nanometre range which is typical of the junction width found in polycrystalline material [67, 92, 93]. The values obtained

Table 5.3: Free fitting parameters, d and η for each specimen.

Specimen	0% Ag	2% Ag	5% Ag	10% Ag
d [nm]	0.13(2)	0.13(5)	0.09(9)	0.10(4)
η	0.32(1)	0.31(5)	0.59(3)	0.47(4)

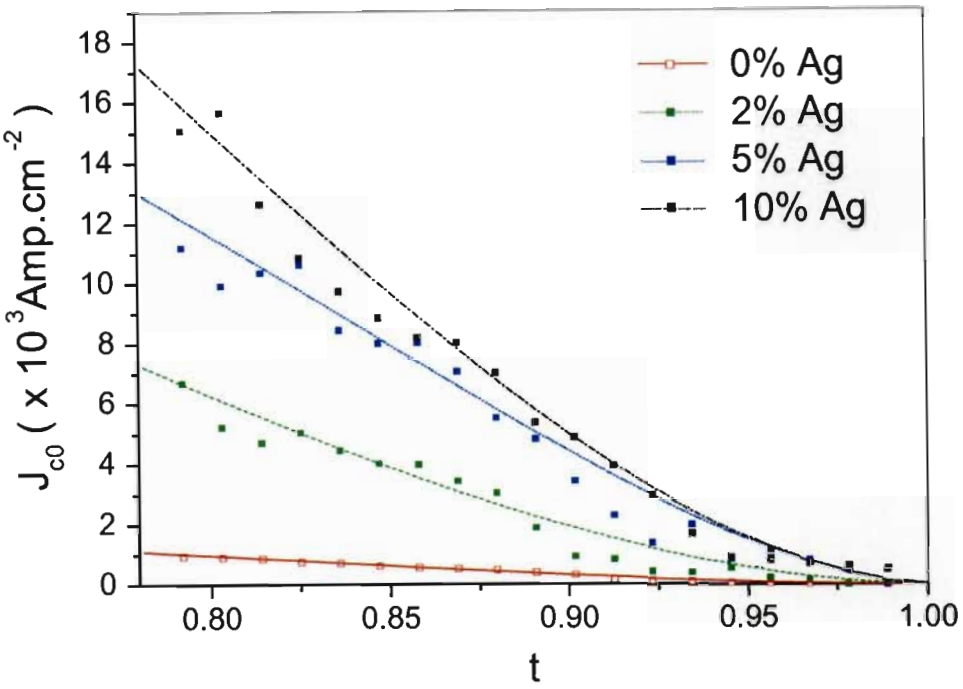

Figure 5-12: Zero-field critical current density $J_{c0} - t$ data (symbols) for various Ag-doped specimens. The curves are Ambegaokar-Baratoff junction fits.

for η agree with model expectation that $\eta \approx 1$.

Zero field critical current, $J_{c0}(t)$

Zero-field critical current density $J_{c0} - t$ data for the Ag doped specimens along with Ambegaokar-Baratoff SIS junction fits, Equation 3.18, are shown in Figure 5-12.

The behaviour of the $J_{c0} - t$ data in Figure 5-12 suggests thermally activated phase slippage (TAPS) [161, 192], where J_{c0} is zero for temperatures less than T_c for all specimens with the possible exclusion of the 10% Ag specimen. The onset of TAPS seems to be most apparent in the 0% Ag specimen, possibly due to a lack of pinning sites, and less with Ag doped specimens. The problem here is the resolution of the data is a limiting factor.

Muhlschlegel's tabulated values for the reduced gap parameter $\Delta(t)/\Delta(0)$, which are plotted in Figure 5-4, and a_0 and T_c from the high-field analysis, were used along with fitting parameters $\omega(0)$ and R_n to fit Equation 3.18 to $J_{c0} - t$ data. The fitting parameters for each specimen are

Table 5.4: Free fitting parameters, $\omega(0)$ and R_nA for each specimen, along with predicted $J_{c0}(0)$ values.

Specimen	0% Ag	2% Ag	5% Ag	10% Ag
$\omega(0)$	1.87(9)	1.41(5)	2.54(7)	1.81(4)
$J_{c0}(0)$ [A/cm^2]	3380	29200	31000	53900
R_nA [Ω.m^2]	7.00(8)	0.75(7)	0.79(3)	0.44(1)

Table 5.5: Results of CSM fitting parameter, reduced field-independent component, δ for each specimen.

Specimen	0% Ag	2% Ag	5% Ag	10% Ag
δ	0.038(5)	0.014(3)	0.009(2)	0.005(1)

tabulated in Table 5-4.

The fitted values for the parameters, $\omega(0)$ for each specimen do not show any strong relationship with doping and values obtained were comparable to values obtained elsewhere [64, 156]. It is apparent from $J_{c0}(t)$ fits that $J_{c0}(0)$ increases with Ag doping of YBCO. This implies an overall increase in intergranular critical current density with Ag doping and is related to a decrease in the resistivity of the intergranular material, R_nA/d (A is the area of an average junction which is proportional to the grain size).

The decrease in resistivity with increasing Ag doping may be attributed to a proximity effect resulting from the presence of Ag in GBJs and/or 'cleaner' GBJs free of secondary impurities. [A similar result was found in the normal resistance versus Ag doping experiment, which is shown in Figure 4-15.] The idea that Ag doping decreases the amount of impurities in GBJs (and hence the resitivity) via a fluxing mechanism is strongly supported in the next section.

Reduced field-independent critical current, δ

As discussed in Section 3.4.2, the reduced field-independent component δ of the critical current density weak-link network is sensitive to the degree of random structural irregularities in GBJs. The behaviour of $\delta = \frac{J_{c1}(T)}{J_{c0}(T)}$ is expected to be independent of temperature (expect near T_c where all length scales are diverging) and is tabulated for all specimens in Table 5-5. Similarly, Doyle *et al* [156] found the same constant temperature behaviour for δ in YBCO.

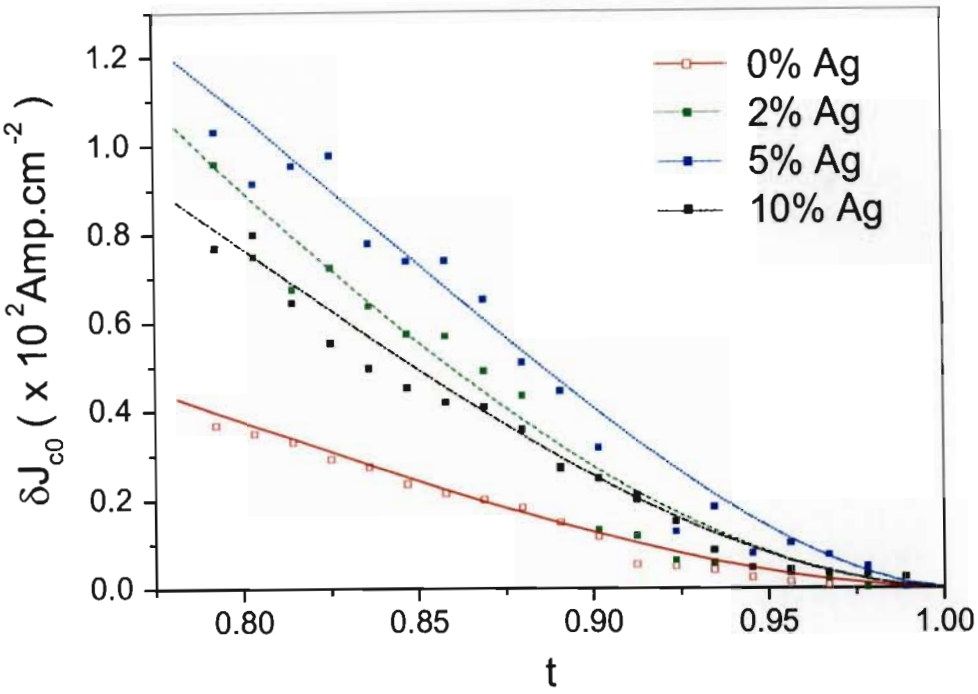

Figure 5-13: Field-independent critical current density $J_{c1} - t$ data (symbols) with fits for various Ag-doped specimens; $J_{c1} = \delta J_{c0}$.

From Equation 3.14), the field-independent critical current density has the form, $J_{c1}(t) = \delta J_{c0}$ and is shown in Figure 5-13 for each of the Ag doped specimens. The following Equation 5.4 is a 2D expression for δ [98, 165]

$$\delta = \left(\frac{4A}{S}\right)^{1/2} \Psi. \tag{5.4}$$

Here S ($\propto a_0^2$) is the average junction area, A is a measure of the average area of structural non-uniformities and $\Psi = \psi_r / J_{c0}$ is a reduced-root-mean squared relative fluctuation of the critical current density in the average GBJ. It is apparent from this expression that the junction area may effect the interpretation of results obtained for δ. Hence, the influence of junction area S (grain size) on the results for δ were normalised out by calculating $J_{c1} S^{1/2} \propto A^{1/2} \psi_r$ and is shown in Figure 5-14.

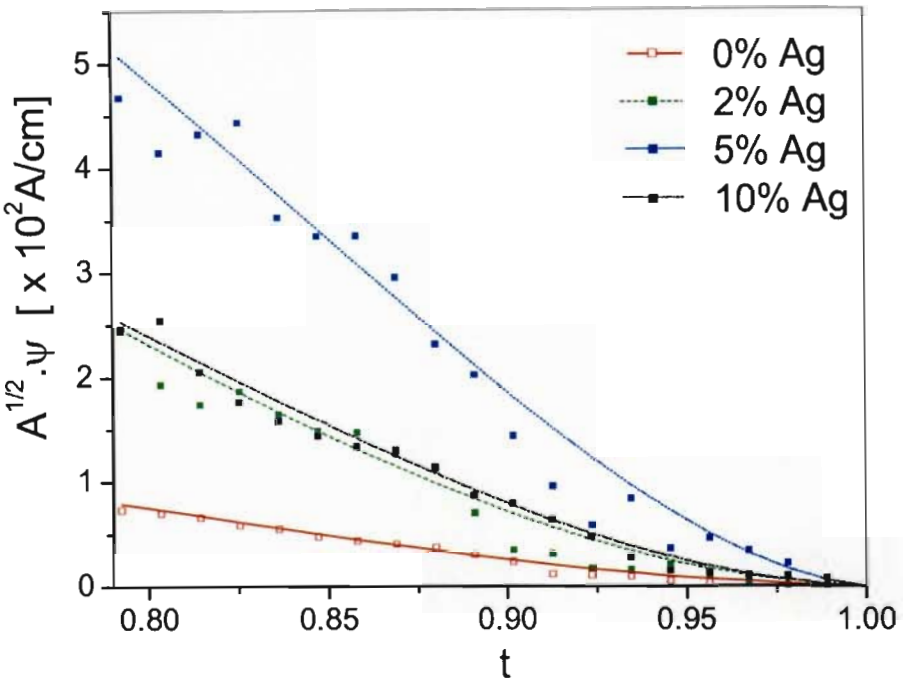

Figure 5-14: A measure of the degree of structural fluctuations $A^{1/2}\psi$ in the average GBJs for Ag-doped YBCO specimens.

It is apparent from Figure 5-13 that J_{c1}, which is sensitive to structural fluctuations through δ, increases with increasing Ag dopant concentration in the range 0%Ag to 5%Ag at all temperatures. This together with the consideration of the above expression for δ (Equation 5.4) and the plot shown in Figure 5-14, suggests that the presence of Ag in the intergranular regions leads to an increase in the structural fluctuations in GBJs. This is supported by the conclusion of the analysis of $J_{c0}(t)$ fits, namely that a decrease in R_n is due to the presence of Ag in the GBJs (proximity effect). However, what is different from the $J_{c0}(t)$ results, when compared to the results of $J_{c1}(t)$, is that $J_{c0}(t)$ increases in the range 0%Ag to 10%Ag compared to an increase in $J_{c1}(t)$ in the range 0%Ag to 5%Ag followed by a decrease for the 10%Ag doped specimen. This decrease in $J_{c1}(t)$ for the 10%Ag specimen suggests a more homogeneous connectivity of grains [193] - at this concentration, the Ag appears to adopt a 'scavenging' (fluxing) nature which results in a corresponding decrease in fluctuations in the GBs. An increase in $J_{c0}(t)$

at 10%Ag is due to an increase in Ag (proximity effect) coupled with a decrease of impurities (fluxing nature), both of which result in decrease in R_n.

The scavenging mechanism is proposed to be as follows: initially Ag dissolves considerable amounts of oxygen (all heat treatments were done in an oxygen atmosphere) [194, 195]. This leads to a decrease in Ag melting point from 960°C (in an inert atmosphere) to about 930°C (in O_2) [196]. The Ag may also react with localised barium-rich areas, leading to a further decrease in the melting point of Ag [197]. Finally, the melted Ag 'moving' through grain-boundaries, 'scavenges' and absorbs impurities, leaving cleaner, narrower and less stressed grain-boundaries.

5.2.2 Other Ag doping experiments

A number of HTS Ag doping experiments [187, 198 - 204] have concluded that Ag doping does improve superconducting properties, but have contradictory conclusions in relation to the optimum doping concentrations and processing methods.

Sintering temperatures, the form and the manner in which Ag is introduced to HTS all play an important role in determining the exact manner Ag effects characteristics of HTS. For example, Ag has been introduced as an oxide [204], Ag-powder [187] and $AgNO_3$ [188], which has resulted in different optimum doping concentrations. In reference [187] YBCO pellet samples were prepared via the standard solid-state reaction method. The samples were crushed into a fine powder and mixed with various amounts of 'Ag-powder', then pressed into pellets and sintered. It was found that intergranular critical current was enhanced for 10%Ag doping, but for more than 15%Ag doping a decrease in intergranular critical current resulted. In another experiment [204], which used Ag in its oxide form, it was found that the intergranular critical current showed a maximum at 20%Ag doping. The difference in optimum doping concentration in these two cases may arise from the different heat treatments employed, where sintering was 920^0C and 930^0C respectively for different durations and/or the different manner in which Ag was introduced.

The 'fluxing' mechanism whereby Ag improves grain connectivity has been hypothesised along with some evidence from microscopy analyses [197], but in the present work there is good evidence to support the fluxing nature of Ag, which is based on a morphologically dependent superconducting analysis. To conclude, the role of Ag doping in the improvement of intergran-

ular critical current is a combination of a proximity-effect, where the presence of Ag in grain boundaries reduces the normal state grain boundary resistance, and a 'fluxing' mechanism, where Ag scavenges impurities from the grain-boundaries.

Figure 5-15 shows the critical current density $J_c(H = 5\ \text{Oe}, t)$ for all Ag doped specimens using the CSM, Equation 3.13. Based on the plots in Figure 5-15, it is clear that the maximum critical density is obtained in the 10%Ag specimen.

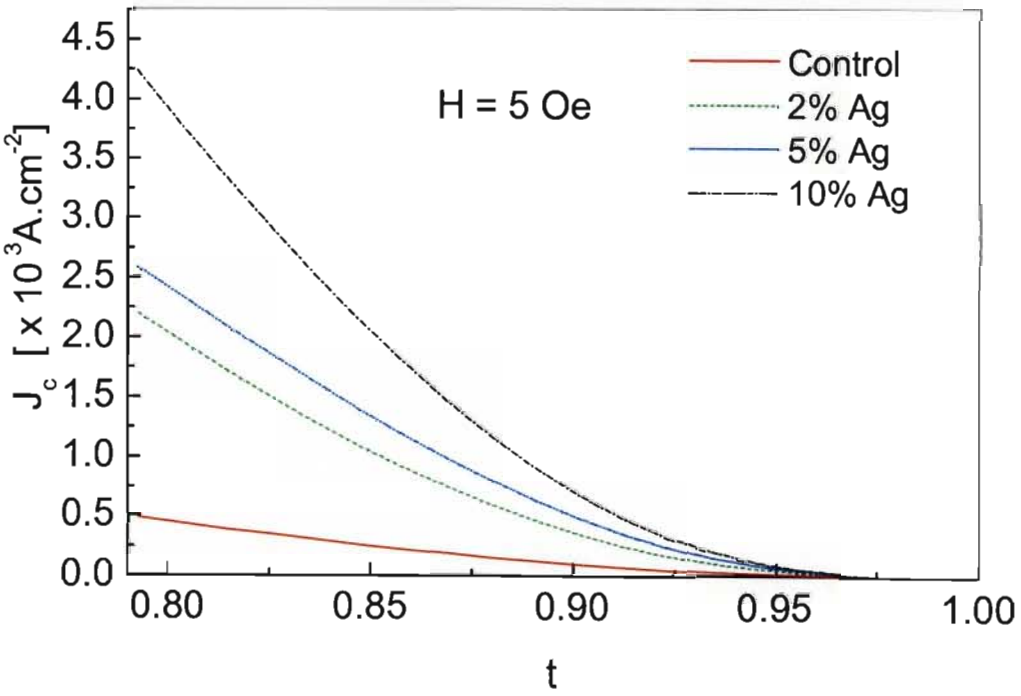

Figure 5-15: Critical current density for polycrystalline Ag-doped YBCO specimens for $H = 5$ Oe obtained from the CSM, $J_c(H,t) = J_{c0}(t)[\exp(\frac{-H}{H_0} + \delta]$, Equation 3.13. Where $J_{c0}(t)$, $H_0(t)$ and δ are obtained from fits.

5.2.3 Short junction criterion

In the above CSM analysis, in particular in the derivation of Equation 3.20 for H_0, GBJs were assumed to be 'short' weak-links in nature, i.e. the Josephson penetration depth, λ_J, is greater than the junction length ($\approx a_0$). The 'short' junction criterion has been confirmed by substituting appropriate values into the expression for the λ_J (Equation 3.1) for different Ag

Table 5.6: Short junction criterion - calculated values for Josephson penetration depth, λ_J for temperatures 0 K and 90 K and grain size for each specimen.

Specimen	0% Ag	2% Ag	5% Ag	10% Ag
$a_0(\mu\text{m})$	3.9	5.2	9.1	6.4
$\lambda_J(T = 0\text{ K})(\mu\text{m})$	3.7	5.4	8.2	6.1
$\lambda_J(T = 90\text{ K})(\mu\text{m})$	8.3	18.1	23.4	14.0

doped specimens. Interpolated results of λ_J are tabulated in the Table 5-6 for the range 0 K$< T <$ 90 K, where the criterion $\lambda_J > a_0$ holds for the entire experimental range, and more or less satisfied the criterion for all temperatures.

Chapter 6

The influence of silver on the joining of large single HTS domains

The reason for the inclusion of the following set of HTS joining experiments is that they complement the insight achieved from Ag doping of polycrystalline YBCO. The effect of Ag doping of GBJs suggests that the Ag doping may help in the difficult process of joining large single HTS crystal domains.

6.1 Introduction - applications of large single domain HTS material

Large single domain HTSs are used in many large scale applications; for example, magnets, rotors for superconducting motors, current limiters and magnetic levitated flywheel energy systems [205 - 208]. In flywheel applications the HTS bearings give the system stability (due to flux pinning) and lift. The levitation force is directly proportional to the HTS bearing size; and hence it is important to fabricate as large a superconducting bearing as possible. Due to the complex structure of HTSs it is difficult to grow large enough bulk bearings consisting of one single domain, especially in a complex shape such as a ring, which may be used in flywheel applications [205 - 208]. The current procedure is to grow as large as possible single domain HTSs (of a few cms) and then to join them [209 - 211]. Due to maximum flux-pinning

requirements, the HTS material of choice is YBCO rather than the more anisotropic BSCCO.

There are a number of joining techniques: multi-seeded joining [212], melt-texturing bonding [213] and solder joining [214 - 216]. Joining of HTSs is not the focus of this thesis, and hence we will not discuss the first two techniques and concentrate only on the third soldering technique; that is, joining single domain YBCO with HTS solder.

The HTS system, $YbBa_2Cu_3O_{7-x}$, has a lower peritectic temperature than the parent material YBCO and was selected as the core constituent in the solder [210, 217, 218]. The joining procedure consists of melting the HTS solder below the parent HTS peritectic temperature and then cooling it in order to physically (and electrically) join the parent material.

The joining process attempts to produce a seam between two superconducting domains. The seam must have similar microstructure and superconducting transport qualities to that of the parent/single domain HTS material. A good join should comprise few voids, pores and trapped secondary phases. It is commonly found that, although the joined sample (in particular the join) is superconducting, there is a reduction in the critical current density J_c. The objective is to have the critical current density of the seam (inter-domain) as close to that of the parent material as possible.

6.2 Experiment

The work discussed in this chapter is based on experiments conducted by Jarvis and Pillay [220]. A short description of our solder-joining experiment and results is given below. The parent material was large single domain seed grown $YBa_2Cu_3O_{7-x}$ (Y123), which were sourced from Superconductive Components Incorporated (USA, Ohio). The following reagents were used in the development of different solder compounds: $YbBa_2Cu_3O_{7-x}$ (Yb123), $Yb_2Ba_1Cu_1O$ (Yb211) and AgO_2.

Yb123 was chosen as the solder because it is a HTS with a critical temperature T_c = 89 K and a crystalline structure similar to YBCO, but with a lower peritectic temperature (approximately 925^0C) compared to the parent material, which has a peritectic temperature of approximately 1010^0C. The inclusion of Yb211 was based on the 'Y-diffusion controlled' model for the growth mechanism of YBCO [217]. We assumed that Yb123 would follow similar

Table 6.1: List of various solders. Solders 1 to 3, an investigation into the optimum Yb123:Yb211 ratio. Solders 4 to 6, the effect of Ag-doping on solders 1 to 3.

Solder	Composition
1	Yb123
2	60% Yb123 : 40% Yb211
3	75% Yb123 : 25% Yb211
4	95% (Solder 1) : 5% Ag_2O
5	95% (Solder 2) : 5% Ag_2O
6	95% (Solder 3) : 5% Ag_2O

decomposition dynamics to YBCO. When YBCO is heated above its peritectic temperature it decomposes into $Y_2Ba_1Cu_1O$ (Y211) solid and a Ba-Cu rich liquid phase. The semi-solid melt is slowly cooled to minimise the number of YBCO nuclei and to maintain a stable growth front. Once a nucleation site forms, a constant supply of Yttrium (in our case, Ytterbium) is required for rapid growth in the ab [110] direction. It has been shown [217] that this growth will be sustained provided there is a dissolution of Y211 particles in the liquid ahead of the growing interface. The inclusion of AgO_2 in the above reagent list was based on the conclusion arrived at in Chapter 5 namely that Ag acts as a flux and consequently aids in improving the joining process.

6.2.1 Sample Preparation

The parent material (single domain YBCO) was hexagonal in shape, with a side and thickness of approximately 25 mm and 10 mm respectively. Rectangular 'prismatic' samples were cut from the parent with dimensions: 4 x 2.5 x 2 mm (a x b x c-axis respective). A total of six different solders were prepared (see Table 6.1). Solders 1, 2 and 3 consisted of Yb123, to which Yb211 was added, in order to determine the optimum ratio of Yb123:Yb211. The ratios 60:40 and 75:25 have been used elsewhere [218, 221]. Solders 4 to 6 were the same as samples 1 to 3, but with the addition of 5%Ag doping by weight.

These solders were mixed with a small amount of glycerine, which was used as a wetting agent to allow for easy application of the solder to the parent material. After the application of the solder, samples were assembled (with bc faces joined) and stablised with a jig (made of high grade stainless steel), which maintained a constant pressure of 5 kPa on the join. The

assembly was placed in a furnace with an oxygen atmosphere at a temperature of 980^0C for 1 hour and cooled at a rate of 5^0C per hour to room temperature. After the heat treatment, the samples were fixed in resin and the cross sectional area reduced to 2.5 x 0.2 mm by use of a grinding wheel. The cross sectional area was reduced in order to facilitate measurements of the critical current. Samples were cleaned ultrasonically and silver contacts were fixed to samples for standard 4-wire resistance measurements.

6.3 Results and conclusions

SEM images were used to examine the microstructure and quality of the superconducting joins. Figure 6-1 shows an SEM image of Sample 1. In the figure, the vertical crack on the right-hand-

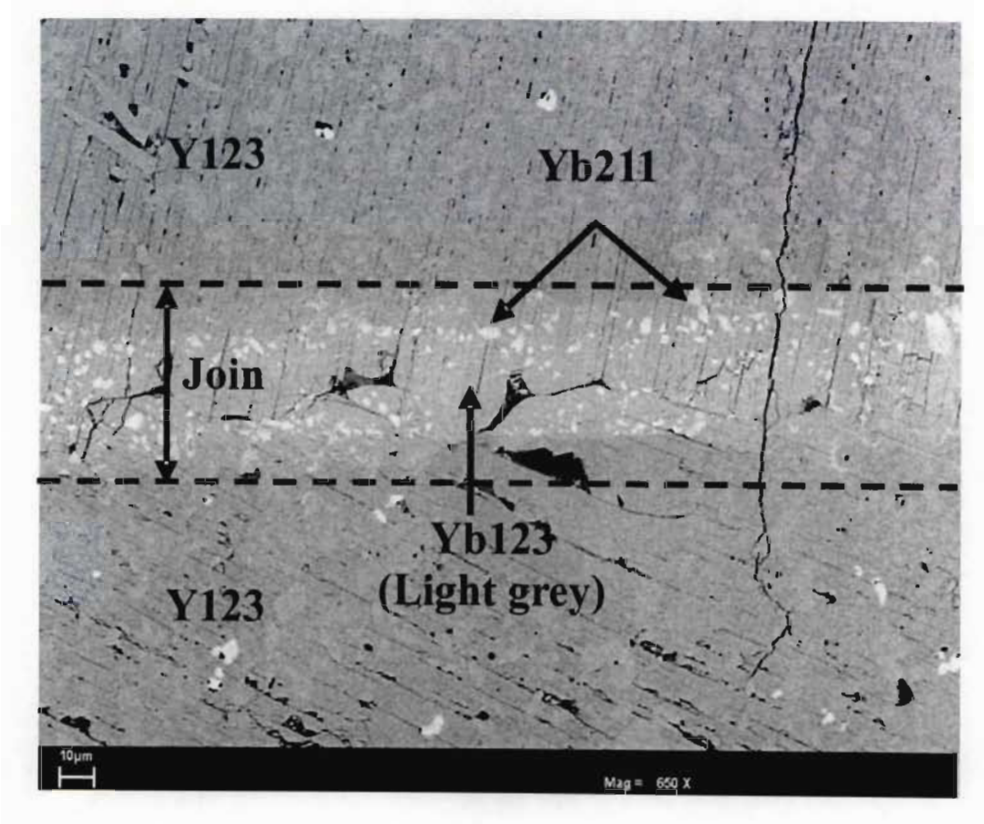

Figure 6-1: SEM image at magnification x 650 of Sample 1.

side is an indication that a good mechanical join was achieved - cracks along the join would be an obvious problem for high critical currents across the join.

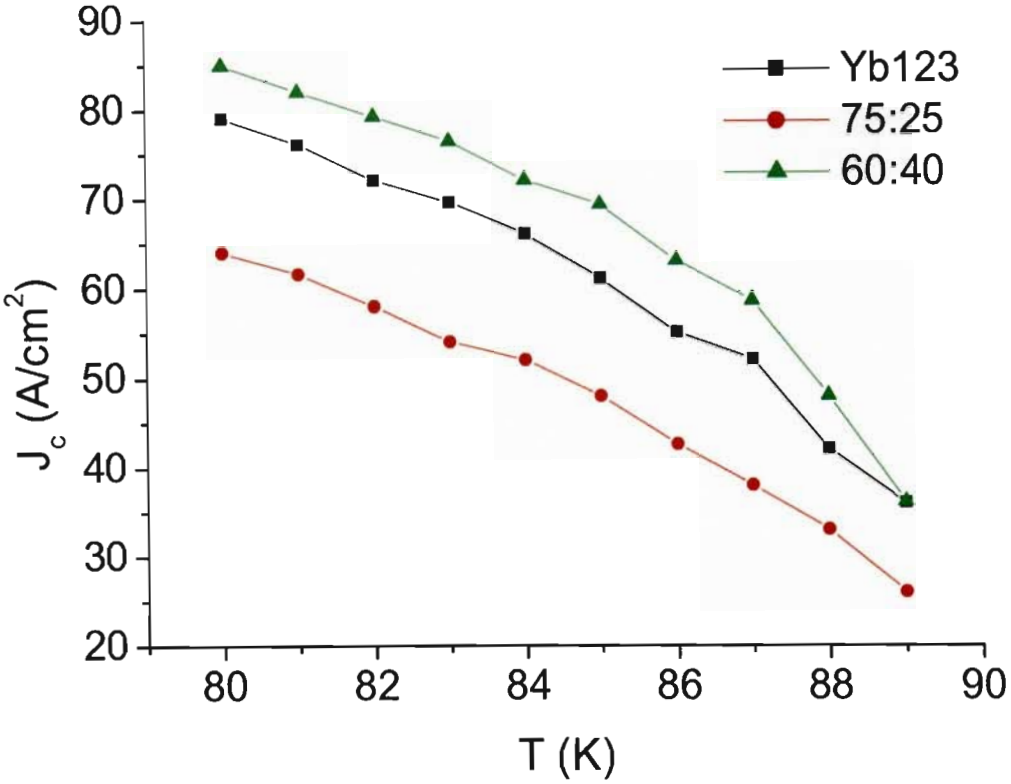

Figure 6-2: Critical current measurements for various solders with different Yb123:Yb211 ratios.

Transport measurements were conducted on each sample. The current in each sample was gradually increased, until a voltage of 1 μV was measured across the join. This was used as an indication that the join was not in a superconducting state. Results of the transport measurements are given in Figures 6-2 and 6-3.

Often in HTS joining experiments, conclusions pertaining to the quality of joins are made without conducting transport measurements, which are the most critical measurements relating to the join. This was demonstrated in the Samples (1 to 3), where SEM images indicated that Sample 1 had the most homogenous join, but not the best transport measurement, as shown in Figure 6-2. Thus SEM images are useful in indicating a potentially good join but, ultimately, transport measurements must be used. In our research of the optimum ratio of

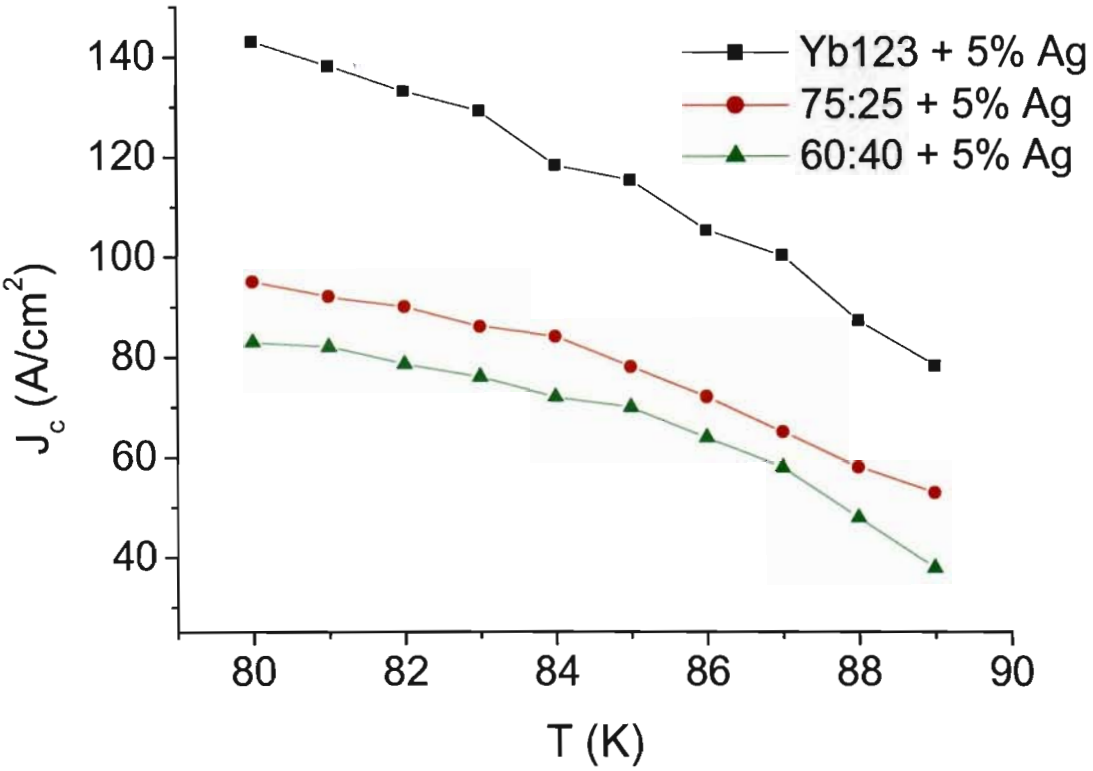

Figure 6-3: Silver experiment, critical current measurements for various solders with different Yb123:Yb211 ratios doped 5% Ag.

Figure 6-4: Large single hexagonal domain YBCO specimen with side and thickness of approximately 25 mm and 10 mm respectively. The sample was cut in half corner to corner and then joined with solder 4.

Yb123:Yb211, the 60:40 mix (without Ag) gave the best transport measurement. The best transport measurement results were achieved with solder 4 (Yb123 + 5%Ag), and with no Yb211 component, see Figure 6-3.

A final solder experiment was conducted to compare parent material with the optimum solder (solder 4). Here an entire single domain YBCO specimen (see Figure 6-4) was cut diagonally in half, then rejoined with the solder and the quality of the join tested.

The join was achieved using a similar heat treatment to that used in the joining of smaller specimens, but a slower cooling rate of 2^0C/hour was used as it was assumed that this would achieve a stronger mechanical join, thereby maximising the critical current. Once the halves were joined, an applied magnetic field of 0.2 T was used to trap a magnetic field in the specimen. A Hall-effect field probe was used to map position (x, y) versus trapped transverse magnetic field above the joined specimen. Magnetic measurements where taken in steps of 2 mm and covered the entire area of the hexagonal specimen. Figure 6-5 shows the resulting plots of the specimen before and after the joining procedure.

Figure 6-6 shows a cross section of three magnetic profiles of the parent specimen: before the cut, with the cut halves pushed back together (but not joined), and the soldered specimen. The quality of the joined specimen compares favourably with the parent/uncut state, with a 5% decrease in the peak magnetisation remnant field. The Ag scavenging mechanism along with the proximity effect identified in Chapter 5 may account for better joins resulting from solder 4.

It has been established that the presence of Ag lowers the peritectic temperature of Y123 [222] and most probabely that of Yb123, resulting in a better quality join. In recent work

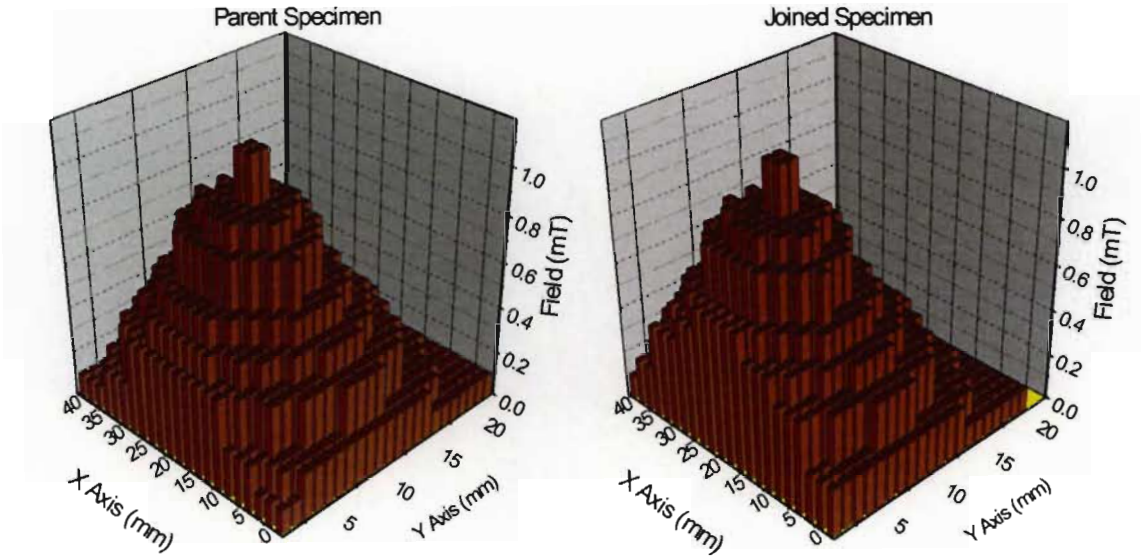

(a) (b)

Figure 6-5: (a) Magnetisation remnant field map of uncut parent specimen. (b) Field map of joined YBCO specimen using solder 4, the join is at y = 10 mm

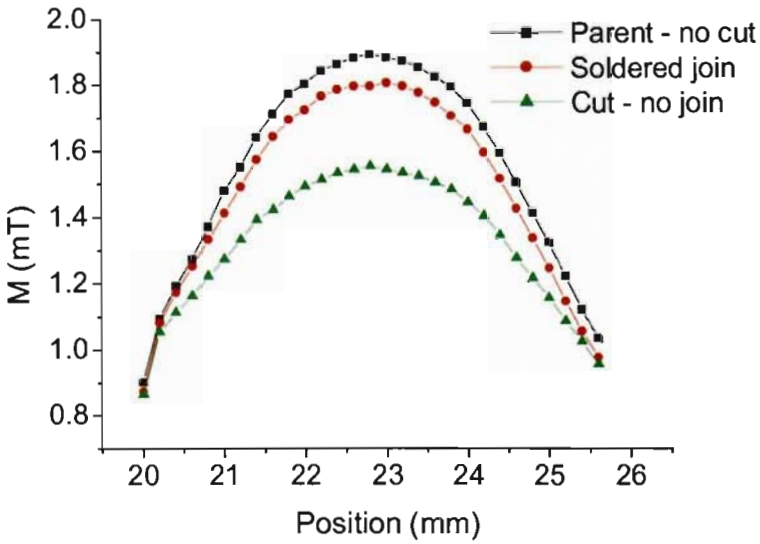

Figure 6-6: Magnetic profile comparison of uncut, cut and soldered YBCO specimen.

the lowering of the HTS melting point temperature was demonstrated to great effect by using Ag foil [223-225], which induced interface melting of bulk melt textured YBCO specimens. It was found that the thickness of the foil was a critical parameter in the establishment of a high quality join; 25μm foil gave superior joins compared to 50μm foil. The Ag-foil technique is easily scaled for complex and large areas; for example, superconducting platforms, and appears to be a superior technique compared to the HTS superconducting solder method described in this chapter.

Chapter 7

Conclusion

7.1 Summary

Grain-boundaries (GBs) made up of a dislocation network, as well as macroscopic cracks, voids and secondary inclusions, and the consequences relating to the order parameter symmetry and GB facets, affect the coupling of grains in polycrystalline HTSs on various spatial scales. This thesis details a study of the effect Ag doping has on polycrystalline HTS YBCO, focusing in particular on the effect Ag has on GBs in various Ag doped YBCO specimens.

The study was inspired by (i) a number of different Ag doping experiments of HTS, which all concluded that Ag doping improves superconducting properties (many papers postulate reasons for the improvements but offer little proof); and (ii) a critical state model (CSM) that is different from other CSMs due to its morphological foundation. It was thought that by analysing a combination of resistance and magnetic measurements, insight into the role of Ag doping in improving superconducting properties could be established and hence a more meaningful understanding of the mechanism/s involved.

Analysis of high-field measurements ($H_a > H_{c1}$) resulted in the estimation of the average magnetic penetration depth versus temperature. This helped in the determination of an 'average cluster size' – a term used in this thesis to mean strongly coupled grains. [It was also established that due to the method of introducing Ag to the YBCO system and the heating process used, not much Ag had diffused into the intragranular material – a desirable outcome as the focus of this study is on the effects of doping on intergranular properties.] The average cluster size

along with a CSM was used in the analysis of low-field measurements ($H_a < H_{c1}$).

It was shown that normal volume fraction, f_n increased with Ag doping with no noticeable effect on the junction width d. The increase in $J_{c0}(0)$ with Ag doping is related to a decrease in the resistivity of the intergranular material, which may be attributed to a proximity effect resulting from the presence of Ag in grain boundary Josephson junctions (GBJs). A decrease in the 10% Ag specimen's reduced field-independent component of the critical current density weak-link network δ, implied 'cleaner' GBJs free of secondary impurities.

Results gave interesting insight into the manner in which Ag affects GBJs i.e. grain-boundaries acting as Josephson junctions. It was concluded that the improvement due to Ag doping was a combination of (i) a proximity effect where trace amounts of Ag residing in the GBJs decrease the normal resistance of the GBJ, and (ii) a scavenging mechanism, which rids GBJs of impurities leaving them cleaner and less stressed.

Other experiments demonstrate the existence of the 'weak-link effect', for example field-cooled HTSs resistance versus temperature measurements, but they do not offer the same insight that above mention magnetic based methodology offers.

7.2 Future Work

Superconducting wire is one of the key applications of HTSs which in the future will hopefully provide cheap, low loss and high transport current wires/tapes. The technological realisation of this potential has been problematic, mainly due to the anisotropic nature of HTS, which manifests in the weak-link effect.

It has been proposed in this thesis that doping can help in the understanding and improvement of the weak-link effect. Calcium doped YBCO heterostructures of epitaxial films [121] have revealed an improvement in grain-to-grain coupling. The improvement is thought to be due to divalent Ca replacing Y (the two elements are approximately the same size) and supplying more charge carriers (holes) to the YBCO system, specifically to the GBJs where it is thought that there is a local hole deficiency. Initially, an improvement to intergranular critical currents was observed in bicrystal YBCO specimens when doped with 30% Ca. Unfortunately, the excessive doping of the YBCO system led to a decrease in T_c to approximately 80 K, which

implied no overall improvement of intergranular coupling at liquid nitrogen temperatures. In order to avoid this problem, multilayers of undoped and Ca-doped YBCO were fabricated and showed good results, where T_c remains high but intergranular coupling improved more than six-fold. This improvement has been explained by Ca from the doped layers diffusing into the GBs of the undoped layer during fabrication. Another Ca-doping YBCO experiment [226] confined Ca to GBs via a 'gel doping process'; here a decrease in T_c and an increase in critical current density was observed.

Presently we are studying the influence of hydrogen doping on GBJ. The objective here is to relieve stresses in GBs, specifically at dislocations in the GBs, which may help improve the grain-to-grain coupling. The main problem in this study is confining the mobile hydrogen to the intergranular and not the intragranular material.

Appropriate doping provides an interesting approach to improving intergranular critical current in HTSs, as demonstrated in the Ag doping experiment. Calcium and other doping YBCO experiments would make interesting research using the methodology described in this thesis. It is hoped that the use of this methodology/'tool' may help in the understanding and improvement of GBJs in HTS systems.

References

[1] H. Kamerlingh Onnes, *Commun. Phys. Lett.* 120b, **3** (1911).

[2] W. Meissner and R. Ochsenfeld, *Naturwissesschaft* **21**, 787 (1933).

[3] A. A. Abrikosov, *Sov. Phys. JETP* **5** 1174 (1957).

[4] J. G. Bednorz and K. A. Müller, *Z. Phys. B* **64**, 189 (1986).

[5] L Gao, Y.Y. Xue, F. Chen, Q. Xiong, R. L. Meng, D. Ramirez, C. W. Chu, J. H. Eggert, H. K. Mao, *Phys. Rev. B* **50**, 4260 (1994).

[6] Explaining high-Tc superconductors, *Physics World* **December**, 55 (1999).

[7] F. London and H. London, *Proc. Roy. Soc. (London) A* **149**, 71 (1935).

[8] V. L. Ginzburg and L. D. Landau, *Zh. Eksperim. i.Teor. Fiz.* **20**, 1064 (1950).

[9] J. Bardeen, L. N. Cooper and J. R. Schrieffer, *Phys. Rev.* **108**, 1175 (1957).

[10] I. Giaever, *Phys. Rev. Lett.* **5**, 147 (1960).

[11] B. D. Josephson, *Phys. Rev. Lett.* **1**, 251 (1962).

[12] P. W. Anderson and J. M. Rowell, *Phys. Rev. Lett.* **10**, 230 (1963).

[13] M. K. Wu, J. R. Ashburn, C. J. Torng, P. H. Hor, R. L. Meng, L. Goa, Z. J. Huang, Y. Q. Wang and C. W. Chu, *Phys. Rev. Lett.* **58**, 908 (1987).

[14] J. Akimitsu, *Symp. on Transition Metal Oxides*, (Sendai) (2001).

[15] J Nagamatsu, N Nakagawa, T Muranaka, Y Zenitani and J Akimitsu, *Nature* **410**, 63 (2001).

[16] D. Dimos, P. Chaudhari, J. Mannhart, F. K. Le Goues, *Phys. Rev. Lett.* **61**, 219 (1988).

[17] S. E. Babcock, X. Y. Cai, D. L. Kaiser, D.C. Larbalestier, *Nature* **347**, 167 (1990).

[18] C.B. Eom, A.F. Marshall, Y. Suzuki, B. Boyer, R.F. W. Pease, T.H. Geballe, *Nature* **353**, 544 (1991).

[19] N.D. Browning, M.F. Chisholm, S.J. Pennycook, *Interface Science* **1**, 309 (1993).

[20] E.Z. Meilikhov, *Physica C* **226**, 69 (1994).

[21] R. Hedderich, T. Schuster, H. Kuhn, J. Geerk, G. Linker, M. Murakami, *Appl. Phys. Lett.* **66**, 3215 (1995).

[22] C. Kittel and H. Kroemer, *Thermal Physics*, 2nd ed., Freeman, 298, (1980).

[23] M. Tinkham, *Introduction To Superconductivity*, 2nd ed., McGraw-Hill, Chap. 4 (1996).

[24] C. J. Gorter and H. B. G. Casimir, *Phys. Z.* **35**, 963 (1934).

[25] A. B. Pippard, *Proc. Roy. Soc.* **A216**, 547 (1953).

[26] L. P. Gor'kov, *Soviet Phys. -JETP* **9**, 1364 (1959).

[27] W. H. Kleiner, L. M. Roth, and S. H. Autler, *Phys. Rev.* **133**, A1226 (1964).

[28] U. Essmann and H. Träuble, *Phys. Lett.* **24A**, 526 (1967).

[29] J. Bardeen, L. N. Cooper and J. R. Schrieffer, *Phys. Rev.* **106**, 162 (1957).

[30] J. Bardeen, Nobel Lecture, *Science* **181**, 1209 (1973); *Physics Today* **26**, 41 (1973).

[31] L. N. Cooper, Nobel Lecture, *Science* **181**, 908 (1973); *Physics Today* **26**, 31 (1973).

[32] L. N. Cooper, *Phys. Rev.* **104** 1189 (1956).

[33] Z. Schlesinger, R. T. Collins, F. Holtzberg, C. Field, G. Koren and A. Gupta, *Phys. Rev. B* **41**, 11 237 (1990).

[34] Mühlschlegel, *Z. Phys.* **155**, 313 (1959).

[35] J. Bardeen, L. N. Cooper and J. R. Schrieffer, *Phys. Rev.* **108**, 1175, (1957).

[36] C.P. Bean, *Phys. Rev. Lett.* **8**, 250 (1962).

[37] B. D. Josephson, *Phys. Lett.* **1**, 251 (1962).

[38] B. D. Josephson, *Rev. Mod. Phys.* **34**, 216 (1964).

[39] B. D. Josephson, *Rev. Mod. Phys.* **46**, 251 (1974).

[40] V. Ambegaokar and A. Baratoff, *Phys. Rev. Lett.* **10**, 486 (1963); erratum, **11**, 104 (1963).

[41] J.M. Rowell, *Phys. Rev. Lett.* **11**, 200 (1963).

[42] A. W. Sleight and J. L. Gillson, P. E. Bierstedt, *Solid State Commun.* **17**, 27 (1975).

[43] K. Höck, H. Nickisch and H. Thomas, *Helv. Phys. Acta* **56**, 237 (1983).

[44] K.A. Müller and J. G. Bednorz, *Science* **237**, 1133 (1987).

[45] C. W. Chu, P. H. Hor, R. L. Meng, L. Gao and Z. J. Huang, *Science* **235**, 567 (1987).

[46] C. W. Chu, P. H. Hor, R. L. Meng, L. Gao, Z. J. Huang and Y. Q. Wang, *Phys. Rev. Lett.* **58**, 405 (1987).

[47] G. Bednorz, K.A. Müller and M. Takashige, *Science* **236**, 73 (1987).

[48] P. H. Hor, L. Gao, R. L. Meng, Z. J. Huang, Y. Q. Wang, K. Forster, J. Vassilious, C. W. Chu, M. K. Wu, J. R. Ashburn and C. J. Torng, *Phys. Rev. Lett.* **58**, 911 (1987).

[49] G. Hammerl, H. Bielefeldt, B. Goetz, A. Schmehl, C. W. Schneider, R. R. Schulz, H. Hilgenkamp and J. Mannhart, *IEEE Transact. Appl. Supercond.* **11**(1), 2830 (2001).

[50] D.P. Norton, A. Goyal, J.D. Budai, D.K. Christen, D.M. Kroeger, E.D. Specht, Q. He, B. Saffian, M.Paranthaman, C.E. Klabunde, D.F. Lee, B.C. Sales, F.A. List, *Science* **274**, 755 (1996).

[51] R. J. Cava, *Scientific American* **263**, 42 (1990).

[52] Y. Tokura and T. Arima, *Jpn. J. Appl. Phys.* **29**, 2388 (1990).

[53] R. J. Cava, B. Batlogg, C. H. Chen, E. A. Rietman, S. M. Zahurak and D. J. Werder, *Nature* **329**, 423 (1987).

[54] C. Jaing and J. P. Carbotte, *Phys. Rev. B* **45**, 10 671 (1992).

[55] C. C. Tsuei, J. R. Kirtley, C. C. Chi, Lock See u-Jahnes, A. Gupta, T. Shaw, J. Z. Sun and M. B. Ketchen, *Phys. Rev. Lett.* **73**, 593 (1994).

[56] J. H. Miller, Q. Y. Ying, Z. G. Zou, N. Q. Fan, J. H. Xu, M.F. Davis and J. C. Wolfe, *Phys. Rev. Lett.* **74**, 2347 (1995).

[57] D. A. Wollman, D. J. Van Harlingen, D. J. Lee, W. C. Lee, D. M. Ginsberg and A. J. Legget, *Phys. Rev. Lett.* **71**, 2134 (1993).

[58] D. A. Brawner and H. R. Ott, *Phys. Rev. B* **50**, 6530 (1994).

[59] D. J. Van Harlingen, *Rev. Mod. Phys.* **67**, 515 (1995).

[60] Y. Ishimaru, J. Wen, K. Hayashi, Y. Enomoto and N. Koshizuka, *Jpn. J. Appl. Phys.* **34**, L1532 (1995).

[61] H. Hilgenkamp, J. Mannhart and B. Mayer, *Phys. Rev. B* **53**, 14 586 (1996).

[62] P. Chaudhari,J. Mannhart, D. Dimos, C. C. Tsuei, J. Chi, M. M. Oprysko and M. Scheuermann, *Phys. Rev. Lett.* **60**, 1653 (1988).

[63] D. Dimos, P. Chaudhari, J. Mannhart and F. K. LeGoues, *Phys. Rev. Lett.* **61** 219 (1988).

[64] J. Mannhart, P. Chaudhari, D. Dimos, C. C. Tsuei and T. R. McGuire, *Phys. Rev. Lett.* **61** 2476 (1988).

[65] J. F. Kwak, E. L. Venturini, D. S. Ginley and W. Fu, *Novel Superconductivity*, eds. S. A. Wolf and V. Z. Kresin, Plenum Press, New York, 983 (1987).

[66] R. L. Peterson and J. W. Ekin, *Phys. Rev. B* **37**, 9 848 (1988).

[67] J. R. Clem, *Physica C* **153-155**, 50 (1988).

[68] S. E. Babcock and D. C. Larbalestier, *J. Mater. Res.* **5**, 919 (1990).

[69] H. W. Zandbergen, R. Gronsky and G. Thomas, *J. Microsc. Spectrosc. Electron.* **13**, 307 (1989).

[70] M. F. Chisholm and S. J. Pennycook, *Nature* **351**, 47 (1991).

[71] V. J. Emery, *Nature* **337**, 306 (1988).

[72] N. Nücker, J. Fink, J. C. fuggle, P. J. Durham and W. M. Temmerman, *Phys. Rev. B* **37**, 5158 (1988).

[73] A. Bianconi, A. C. Castellano, M. D. Santis, P. Delogue, A. Gargano and R. Giorgi, *Solid State Commun* **63**, 1135 (1987).

[74] J. D. Jorgensen, B. W. Veal, W. K. Kwok, G.W. Crabtree, A. Umezawa, L.J Nowicki and A. P. Paulikas, *Phys. Rev. B* **36**, 5731 (1987).

[75] Z. G. Ivanov, P. A. Nilsson, D. Winkler, J. A. Alarco, T. Claeson, E. A. Stepantsov and A. Ya. Tzalenchuk, *Appl. Phys. Lett.* **59**, 3030 (1991).

[76] J. M. Philips, *J. Appl. Phys.* **79**, 1829 (1996).

[77] D. P. Norton *et al.*, *Appl. Phys. Lett.* **57**, 1164 (1990).

[78] R. Gross and B. Mayer, *Physica C* **180**, 235 (1991).

[79] M. Kawasaki *et al.*, *Appl. Phys. Lett.* **62**, 417 (1993).

[80] M. Kawasaki, P. Chaudhari and A. Gupta, *Appl. Phys. Lett.* **68**, 1065 (1992).

[81] E. Z. Meilikhov, *Physica C* **271**, 277 (1996).

[82] H. W. Zandbergen, R. Gronsky and G. Thomas, *J. Microsc. Spectrosc. Electron.* **13**, 307 (1988).

[83] F. Deslanders, B. Raveau, P. Dubots and D. Legat, *Solid State Commun.* **71**, 407 (1989).

[84] C. C. Tsuei, J. R. Kirtley, C. C. Chi, Lock See Yu-Jahnes, A. Gupta, T. Shaw, J. Z. Sun and M. B. Ketchen, *Phys. Rev. Lett.* **73**, 593 (1994).

[85] J. H. Miller, Q. Y. Ying, Z. G. Zou, N. Q. Fan, J. H. Xu, M. F. Davis and J. C. Wolfe, *Phys. Rev. Lett.* **74**, 2347 (1995).

[86] D. A. Wollman, D. J. Van Harlingen, D. J. Lee, W. C. Lee, D. M. Ginsberg and A. J. Legget, *Phys. Rev. Lett.* **71**, 2134 (1993).

[87] K. A. Müller, *Nature* **377**, 133 (1995).

[88] D. J. Van Harlingen, *Rev. Mod. Phys.* **67**, 515 (1995).

[89] I. Iguchi and Z. Wen, *Phys. Rev. B* **49**, 12388 (1994).

[90] H. Hilgenkamp, J. Mannhart and B. Mayer, *Phys. Rev. B.* **53**, 14586 (1996).

[91] J. Mannhart and H. Hilgenkamp, *Supercond. Sci. Technol.* **10** 880 (1997).

[92] M. Däumling, E. Sarnelli, P. Chaudhari, A. Gupta, J. Lacey, *Appl. Phys. Lett.* **61**, 1355 (1992).

[93] O. M. Froehlich, H. Schulze, A. Beck, B. Mayer, L. Alff, R. Gross, R. P. Huebener, *Appl. Phys. Lett.* **66**, 2289 (1995).

[94] T. T. Tan, S. Li, H. Cooper, W. Gao, H. K. Liu and S. X. Dou, *Supercond. Sci. Technol.* **14** 471 (2001).

[95] J. Horvat, W.G. Wang, R. Bhasale, Y. C. Guo, H. K. Liu and S. X. Dou, *Physica C* **275**, 327 (1997).

[96] A. Goyal, E. D. Specht, D. K. Christen, D. M. Kroeger, A. Pashitski, A. Polyanskii, D. C. Larbalestier, *JOM* **October** (1996).

[97] A. Barone, G. Paterno, M. Russo and R. Vaglio, *Phys. Stat. Sol.* **41**, 393 (1977).

[98] A. Barone and G. Paterno, *Physics and Applications of the Josephson Effect* Wiley, New York (1982).

[99] I. K. Yanson, *Sov. Phys. JETP* **31** (5), 800 (1970).

[100] E. Z. Meilikhov, *Superconductivity* **3** (7), 1110 (1990).

[101] J. C. Martinez, S. H. Brongersma, A. Koshelev, B. Ivlev, P. H. Kes, R.P. Griessen, D. G. de Groot, Z. Tarnavski and A. A. Menovsky, *Phys. Rev. Lett.* **69**, 2276 (1992).

[102] W. E. Lawrence and S. Doniach, *Proc. 12th Int. Conf. Low Temp. Phys.* E. Kanda (ed.), 361 (Kyoto, 1970; Keigaku, Tokyo, 1971).

[103] G. Blatter, V. B. Geshkenbein and A. I. Larkin, *Phys. Rev. Lett.* **68**, 875 (1992).

[104] Department of Energy (United States), Superconductivity for Electric Systems Program Plan, DOE/GO-10096-167 (1996).

[105] P. Komarek, *Contemp. Phys.* **17**, 355 (1976).

[106] J. Everett, M. D. Dhalle, M. D. Johston, A. D. Caplin, J. C. Moore, S. Fox, D. Hyland, C. R. M. Grovenor, *Supercond. Sci. Technol.***9**, 1077 (1996).

[107] J. Horvat, W.G. Wang, R.Bhasale, Y.C. Gui, H.K. Liu, S.X. Dou, *Physica C* **275**, 327 (1997).

[108] D. T. Verebelyi, D. K. Christen, R. Feenstra, C. Cantoni, A. Goyal, D. F. Lee, M. Paranthaman, P. N. Arendt, R. F. DePaula, and J. R. Groves, Appl. *Phys. Lett.* **76**, 1755 (1995)

[109] J. W. Ekin, K. Salama, V. Selvamanickam, *Nature* **350**, 26 (1991).

[110] D. T. Shaw, *Mater. Res. Soc. Bull.***17**, 39 (1992).

[111] S. Kobayashi, T. Kaneko, T. Kato, J. Fujikami, K. Sato, *Physica C* **258**, 336 (1996).

[112] T. P. Orlando, K. A. Delin, *Applied Superconductivity*, Addison Wesley Publishing Company, 369-385 (1990).

[113] G. B. Lubkin, Phys. Today 49, 48-51 (1996).

[114] M. R. Beasley, *IEEE Trans. Appl. Supercond.* **15**(2), 141 (1995).

[115] A. Goyal, D.P. Norton, J.D. Budai, M. Paranthaman, E.D. Specht, D.M. Kroeger, D.K Christen, Q. He, B. Saffian, F.A. List, D.F. Lee, P.M. Martin, C.E. Klabunde, E. Hartfield and V.K. Sikka, *Appl. Phys. Lett.* **69**, 1795 (1996)

[116] Y. Iijima, N. Tanabe, O. Kohno, Y. Ikeno, Appl. Phys. Lett. **60**, 769 (1992).

[117] R. P. Reade, P. Berdahl, R. E. Russo, S. M. Garrison, *Appl. Phys. Lett.* **61**, 2231 (1992).

[118] X. D. Wu *et al*, Appl. *Phys. Lett.* **67**, 2397 (1995).

[119] D.P. Norton, A. Goyal, J.D. Budai, D.K. Christen, D.M. Kroeger, E.D. Specht, Q. He, B. Saffian, M. Paranthaman, C.E. Klabunde, D.F. Lee, B.C. Sales, and F. A. List, *Science* **274**, 755 (1996).

[120] A. L. L. Jarvis and T. B. Doyle, *Inst. Phys. Conf. Ser.* **158**, 1149 (1997).

[121] G. Hammerl, A. Schmehl, R.R. Schulz, B. Goetz, H. Bielefeldt, C.W. Schneider, H. Hilgenkamp, J. Mannhart, *Nature* **407**, 162 (2000).

[122] For example AT&T, Illinois Superconductors, Conductus, American Superconductor Corporation and Superconductive Technology Inc.

[123] See a review by P. C. W. Chu, *Scientific American* **273**(3), 162 (1995).

[124] K. K. Likharev, *Supercond. Sci. Technol.* **3**, 325 (1990).

[125] See a review by D.K. Brock, E.K. Track, J.M. Rowell, *IEEE Spectrum* **Dec**, 40 (2000).

[126] O. A. Mukhanov, S. V. Rylov, *IEEE Trans. Appl. Supercond.* **7**, 2669 (1997).

[127] A. H. Silver, *IEEE Trans. Appl. Supercond.* **7**, 69 (1997).

[128] T. van Duzer and C. W. Turner, *Principles of superconductive devices and circuits*, 2nd ed., Prentice Hall, (1999).

[129] S. L. Bud'ko *et al*, *Phys. Rev. Lett.* **86**, 1877 (2001).

[130] D. C. Larbalestier *et al*, *Nature* **410**, 186 (2001).

[131] K. A. Muller, M. Pomerantz, C. M. Knoedler and D. Abraham, *Phys. Rev. Lett.* **45**, 832 (1980).

[132] E. Stocker and J. Buttet, *Solid State Comm.* **53**, 915 (1985).

[133] D. Goldschmidt, *Phys. Rev. B* **39** 9139 (1989).

[134] A. Gerber, T. Grenet, M. Cyrot and J. Beille, *Phys. Rev. B* **43**, 12 935 (1991).

[135] P. Pureur, R. M. Costa, P. Rodrigues Jr, F. Schaf and J. V. Kunzler, *Phys. Rev. B* **47** 11 420 (1993).

[136] A. Oral, S. J. Bending, R. G. Humphreys and M. Henine, *Supercond. Sci. Technol.* **10** 12 and references therein (1997).

[137] H. F. Hess, C.A. Murray and J. V. Waszczak, *Phys. Rev. Lett.* **69** 2138 (1992).

[138] K. E. Andreev, A. V. Bobyl, S. A. Gudushnikov, S. F. Karmanenko, S. L. Kransosvobodtsev, L. V. Matveets, O. V. Snigirev, R. A. Suris and I. I. Vengrus, *Supercond. Sci. Technol.* **10** 366 (1997).

[139] A. Goyal, E. D. Specht, D. M. Kroeger, T. A. Mason, D. J. Dingley, G. N. Riley and M.W. Rupich, *Appl. Phys. Lett.* **66** 2903 (1995).

[140] A. E. Pashitsjki, A. Polyanskii, A. Gurevich, J. A. Parrell and D. C. Labalestier, *Physica C* **246** 133 (1995).

[141] M. Prester and E. Babic, Critical Currents in Superconductors, Proc. 7th Workshop, H. W. Weber (ed), 521 (1994).

[142] H. Kupfer, I. Apfelstadt, R. Flukiger, C. Keller, R. Meier-Hirmer, B. Runtschi, A. Turowski, U. Wiech and T. Wolf, *Cryogenics* **29**, 268 (1989).

[143] S. E. Male, J. Chilton, A. D. Caplin, C. N. Guy ans S. B. Newcomb, *Supercond. Sci. Technol.*, **1**, 1 (1989).

[144] J. W. Ekin, H. R. Hart Jr. and A. R. Gaddippati, *J. Appl. Phys.* **68**, 2285 (1990).

[145] J. W. Ekin, *Physica C*, **160**, 489 (1989).

[146] V. M. Vinokur and A. E. Koshelev, *Sov. Phys. JETP* **70**, 547 (1990).

[147] R. Fehrenbacher, V. B. Geshkenbein and G. Blatter, *Phys. Rev. B.* **45**, 5450 (1992).

[148] S. E. Russek, D. K. Lathrop, B. H. Moeckly, R. A. Buhrmann and D. H. Shin, *Appl. Phys. Lett.* **57**, 1155 (1990).

[149] E. Sarnelli, P. Chaudhari, M. Däumling and J. A. Lacey, *IEEE Trans. Appl. Supercond.*, **AS-3**, 2329 (1993).

[150] O. M. Froehlich, H. Schultze, A. Beck, B. Mayer, L. Alff, R. Gross and R. P. Huebener, *Appl. Phys. Lett.* **66**, 2289 (1995).

[151] J. Halbritter, *Phys. Rev. B* **46**, 14861 (1992).

[152] H. Hilgenkamp, C. W. Schneider, B. Goetz, R. R. Schulz, A. Schmehl, H. Bielefeldt and J. Mannhart, *Supercond. Sci. Technol.* **12**, 1043 (1999).

[153] E. Z. Meilikhov and T. B. Doyle, in: Proc. *7th Int. Critical Currents Workshop*, Alpbach, January (1994)

[154] E. Meilikhov and Yu. Gershanov, *Physica C* **157**, 431 (1989).

[155] F. Stucki, J. Rhyner and G. Blatter, *Physica C* **181**, 385 (1991).

[156] T. B. Doyle and R. A. Doyle, *Phys. Rev. B* **47**, 8111 (1993)

[157] G. Deutscher and K. A. Muller, *Phys. Rev. Lett.* **59**, 1745 (1987).

[158] L. N. Bulaevskii, V. L. Ginzburg and A. A. Sobyanin, *Sov. Phys. JETP* **67**, 1499 (1988).

[159] G. Deutscher and P. Chaudhari, *Phys. Rev. B* **44**, 4664 (1991).

[160] T. B. Doyle, R. A. Doyle and L. Scribani, *J. Supercond.* **7**, 747 (1994).

[161] V. Ambegaokar and B. I. Halperin, *Phys. Rev. Lett.* **22**, 1364 (1969).

[162] E. Sarnelli, P. Chaudhari and J. Lacey, *Appl. Phys. Lett.* **62**, 777 (1993)

[163] J. H. P. Waston, *J. Appl. Phys.* **39**, 3406 (1968).

[164] H. Dersch and G. Blatter, Phys. Rev. B 38, 11 391 (1988).

[165] A. Barone, G. Paterno, M. Russo and R. Vaglio, *Sov. Phys. JETP* **47**(4), 778 (1978).

[166] E. Sarnelli, P. Chaudhari and J. Lacey, *Appl. Phys. Lett.* **62** (7), 777 (1993).

[167] T. B Doyle, R. A. Doyle, D. Minkov, V. N. Stepankin and U. P. Yakovets, *Physica C* **233**, 253 (1994).

[168] V. G. Kogan, *Phys. Rev. B* **24** (3), 1572 (1981).

[169] V. G. Kogan, M. M. Fang and Sreeparna Mitra, *Phys. Rev. B* **38** (16), 11958 (1988).

[170] A. M. Neminsky and P. N. Nikolaev, *Physica C* **212**, 389 (1993).

[171] M. Tinkham, *Introduction To Superconductivity*, 2nd ed., McGraw-Hill, page 321 (1996).

[172] J. Van der Mass, V.A. Gasparov and D.Pavuna, *Nature* **328**, 603 (1987).

[173] R. Flükiger, T. Müller, W. Goldacker, T. Wolf, E. Seibt, I. Apfelstedt, H. Küpfervand W. Schauer, *Physica C*, **153-155**, 1574 (1988).

[174] D. Kumar, M. Sharon, P.R. Apte, L. C. Gupta and R. Vijayaraghavan, *Appl. Phys. Lett.*, **62**, 3522 (1993).

[175] J. Kurian, A. M. John, P. R. S. Wariar, P. K. Sajith, J. Koshy, S. P. Pai and R. Pinto, *Supercond. Sci. Technol.*, **13** 178 (2000).

[176] J. P. Singh, H. J. H. J. Leu, R. B. Poeppel, E. Van Voorhees, G. T. Goudey, K. Wensley and D. Shi, *J. Appl. Phys.*, **66**, 3154.

[177] P. Diko, G. Krabbes and C. Wende, *Supercond. Sci. Technol.* **14**, 486 (2001).

[178] H. Salamati, Ali A. Babaei-Brojeny and M. Safa, *Supercond. Sci. Technol.* **14**, 816 (2001).

[179] T. B. Doyle, Ph.D. thesis, University of the Witwaterrand (1975).

[180] M. Tinkham, *Introduction To Superconductivity*, 2nd ed., McGraw-Hill, page 379 (1996).

[181] G. Deutscher, Physica Scripta **T29**, 9-14 (1989).

[182] F. Hentsch, H. Seidel, M. Mehring, J. G. Bednorz and K. A. Müller, Physica C **153-155**, 1712 (1988).

[183] J. R. Cooper, C. T. Chu, L. W. Zhou, B. Dunn and G. Grüner, Phys. Rev. B, 37, 638 (1988).

[184] S. Mitra, J. H. Cho, W. C. Lee, D. C Johnston and V. G. Kogan, Phys. Rev. B, **40**, 26774 (1989).

[185] T. E. Faber and A. B. Pippard, *Proc. Roy. Soc.*, **A231**, 336-353 (1955).

[186] P. N. Dheer, *Proc. Roy. Soc.*, **A260**, 333-349 (1961).

[187] S. Goto and K. Shiiki, *Jpn. J. Appl. Phys.*, **34**, 4760-4764 (1995).

[188] E. Mogilko and Y. Schlesinger, *Supercond. Sci. Technol.*, **10**, 134-141 (1997).

[189] D. Minkov and T. B. Doyle, *Proc. 7th Int. Critical Currents Workshop*, Alpbach, (1994).

[190] A. Brown, *Magnetostatic Principles in Ferromagnetism*, Noth Holland Pub. Co., Amsterdam, (1962).

[191] E. Mendoza, T. Puig, E. Varesi, A.E. Carrillo, J. Plain and X. Obradors, *Physica C* **334**, 7 (2000).

[192] R. Gross, P.Chaudhari, D. Dimos, A. Gupta and G. Koren, *Phys. Rev. Lett.* **64**, 228 (1990).

[193] Z. Meilikhov, *Phys. Usp*, **36**, 129-151, (1993).

[194] W. Eichenauer and G. Müller, *Z. Metallk.*, **53**, 321, (1962).

[195] E.W.R. Steacie and F.M.G. Johnson, *Proc. R. Soc. A*, **112**, 542, (1926).

[196] H.C. Vacher, *Metals Handbook*, Cleveland, OH: American Society of Metals, 1151, (1948).

[197] F. Deslandes, B. Raveau, P. Dubots and D. Legat, *Solid State Comm.*, **71**, 407, (1989).

[198] B. Dwir, M. Affronte, D. Pavuna, *Appl. Phys. Lett.*, **55**, 399 (1989).

[199] S. L. Shinde, J. Morrill, D. Goland, D. A. Chance and T. McGuire, *Phys. Rev. B*, **41**, 8838, (1990).

[200] T. S. Orlova, J. Y. Laval, A. Dubon, C. Nguyen-van-Huong, B. I. Smirnov and Yu P. Stepanov, *Supercond. Sci. Technol.* **11**, 467, (1998).

[201] D. Lee and K. Salama, *Japan. J. Appl. Phys.*, **29** L2017, (1990).

[202] M. J. Wang, D. C. Ling, J. L. Lin, M. K. Wu, C. C. Chi, *Physica C*, **185-189**, 2417 (1991).

[203] C. Nguyen-van-Huong, E. Crampin, J. Y. Laval and A. Dubon, *Supercond.Sci. Technol.*, **10**, 85 (1997).

[204] H. Salamati, A. A. Babaei-Brojeny and M. Safa, *Supercond.Sci. Technol.*, **14**, 816 (2001).

[205] K. B. Ma, Q. Y. Chen, E. Postrekhin, Y. Zhan and W. K. Chu, *Physica C*, **341–348**, 2517 (2000).

[206] M. Komori and N. Akinage, *IEEE Trans. Appl. Supercond.*, **11**, 1733 (2001).

[207] J. R. Fang, L. Z. Zin, L. G. Yan and L. Y. Xiao, *IEEE Trans.Appl. Supercond.*, **11**, 1657 (2001).

[208] I. Vajda, T. Porjesz, A. Györe, A. Szalay, W.Gawalek, *Physica C*, **341-348**, 2609 (2000).

[209] R. A. Doyle, A. D. Bradley,W. Lo, D. A. Cardwell, A. M. Campbell, Ph. Vanderbemben, R. Cloots, *Appl. Phys. Lett.*, 73, **117** (1998).

[210] K. Iida, T. Kono, T. Kaneko, K. Katagiri, N. Sakai, M. Murakami and N. Koshizuka, *Supercond. Sci. Technol.*, **17**, S46 (2004).

[211] T. Kaneko, K. Iida, T. Kono, N. Sakai, M. Murkami, N. Koshizuka, A. Murakami, K. Katagiri, *Physica C*, **412-414**, 678 (2004).

[212] P. Schatzle, G. Krabbes, G. Stover, G. Fuchs and D. Schlafer, *Supercond. Sci. Technol.*, **12**, 69-76 (1999).

[213] L. Chen, H. Claus, A. P. Paulikas, H. Zheng and B. W. Veal, *Supercond. Sci. Technol.*, **15**, 672-674 (2002).

[214] D. Shi, *Appl. Phys. Lett.*, **66**, 2573-2575 (1995).

[215] H. Walter, C. H. Jooss, F. Sandiumenge, B. Bringmann, M. P. Delamare, A. Leenders and C. Freyhardt, *Euro. Phys. Letts*, **55**, 100-104 (2001).

[216] H. Zheng, M. Jiang, R. Nikolova, U. Welp, A.P. Paulikas, Y. Huang, G.W. Crabtree, B.W. Veal and H. Claus, *Physica C*, **322**, 1-8 (1999).

[217] K. Salama K and D. F. Lee, *Supercond. Sci. Technol.*, **7** 177 (1994).

[218] G. J. Schmitz, A. Tigges and J. C. Schmidt, *Supercond. Sci. Technol.*, **11**, 73 (1998).

[219] J. G. Noudem, E. S. Reddy, M. Tarka, M. Noe and G. J. Schmitz, *Supercond. Sci. Technol.*, **14**, 363 (2001).

[220] A L L Jarvis and M Pillay, *J. Phys.: Conf. Ser.*, **43,** 434 (2006).

[221] H. Zheng, M. Jiang, R. Nikolova, U. Welp, A. P. Paulikas, Y. Huang, G. W. Crabtree, B. W. Veal and H. Claus, *Physica C* **322** 1 (1999).

[222] U. Wiesner, G. Krabbes, M. Ueltzen, C. Magerkurth, J. Plewa and H. Altenburg, *Physica C*, **294**, 17 (1998).

[223] S. Iliescu, X. Granados, E. Bartolomé, S. Sena, A. E. Carrillo, T. Puig, X. Obradors and J. E. Evetts, *Supercond. Sci. Technol.* **17**, 182 (2004).

[224] S. Iliescu, A. E. Carrillo, E. Bartolomé, X. Granados, B. Bozzo, T. Puig, X. Obradors, I. García and H. Walter, *Supercond. Sci. Technol.*,**18**, 168 (2004).

[225] B. Bozzo, E. Bartolomé, X. Granados, T. Puig and X. Obradors, *J. Phys.: Conf. Ser.*, **43**, 401 (2006).

[226] A. Berenov, C. Farvacque, X. Qi, J. L. MacManus-Driscoll, D. MacPhail and S. Foltyn, *Physica C* **372-376**, Part 2, 1059 (2002).